NOVA SCHOOL OF SCIENCE & TECHNOLOGY

DEPARTMENT OF ELECTRICAL AND COMPUTER ENGINEERING

SIMULTANEOUS WIRELESS INFORMATION AND POWER TRANSFER IN 5G COMMUNICATION

AKASHKUMAR RAJARAM

Master of Science in Engineering ⟨Cyber Security⟩

DOCTORATE IN ELECTRICAL AND COMPUTER ENGINEERING

NOVA University Lisbon
May, 2023

DEPARTMENT OF ELECTRICAL
AND COMPUTER ENGINEERING

SIMULTANEOUS WIRELESS INFORMATION AND POWER TRANSFER IN 5G COMMUNICATION

AKASHKUMAR RAJARAM

Master of Science in Engineering ⟨Cyber Security⟩

Adviser: Doctor Rui Miguel Henriques Dias Morgado Dinis
Associate Professor with Habilitation, Universidade NOVA de Lisboa

Co-advisers: Doctor Dushantha Nalin K. Jayakody
Associate Professor, Universidade Lusófona de Humanidades e Tecnologias

Examination Committee

Chair: Doctor Paulo da Costa Luís da Fonseca Pinto
Full Professor, Universidade NOVA de Lisboa

Rapporteurs: Doctor Francisco António Bucho Cercas
Full Professor, Instituto Universitário de Lisboa

Doctor Marco Alexandre Cravo Gomes
Assistant Professor, Universidade de Coimbra

Adviser: Doctor Rui Miguel Henriques Dias Morgado Dinis
Associate Professor with Habilitation, Universidade NOVA de Lisboa

Members: Doctor Marko Beko
Associate Professor with Habilitation, Universidade de Lisboa

Doctor Rodolfo Alexandre Duarte Oliveira
Associate Professor with Habilitation, Universidade NOVA de Lisboa

DOCTORATE IN ELECTRICAL AND COMPUTER ENGINEERING

NOVA University Lisbon
May, 2023

Simultaneous Wireless Information and Power Transfer in 5G communication

Acknowledgements

I express my sincere gratitude to my adviser, Professor Rui Dinis, who guided me throughout my doctoral course and from time to time gave his valuable feedback. His friendly approach and initiative to support in research work and personal life helped me a lot in my career. I would like to thank my co-advisor Prof. Nalin Jayakody for his support and guiding my research work. I am grateful to Prof. Marko Beko for his academic support and valuable feedback to my research work. I would like to thank Prof. João Guerreiro for his valuable contribution and feedback, and I could learn a lot from him, especially about nonlinear distortion and optimization problems. I had comfortable and memorable office hours, thanks to David Borges, António Furtado, Luís Irio, Slaviša Tomic, Tharindu Perera, Furkhan Ali and Rabia Khan. David Borges and António Furtado were really very helpful on academic as well as on personal side. David and I had a lot of discussion and research work together, which helped me to explore MIMO and other topics in wireless communication.

I express my deepest gratitude to Faculdade de Ciências e Tecnologia da Universidade NOVA de Lisboa, Instituto de Telecomunicações, Universidade Lusófona (Copelabs) and National Research Tomsk Polytechnic University for hosting me and supporting my research work. My doctoral research work was supported by Fundação para a Ciências e Tecnologia through my doctoral grant DFA/BD/7926/2020, and Instituto de Telecomunicações under projects UID/EEA/50008/2013, UID/EEA/50008/2019 and MASSIVE5G (SAICT-45-2017-02). My research work was also funded by Copelabs, Universidade Lusòfona funding through UIDB/04111/2020 and National Research Tomsk Polytechnic University through Russian Federal Basic Research grant No 19-37-50083/19 and No. 8.13264.2018/8.9. The research work was also supported by the framework of Competitiveness Enhancement Program of the National Research Tomsk Polytechnic University and IRACON CA15014 research visits grant for early career researchers.

I dedicate my thesis to my parents and sisters, who were always there and for being part of me.

Abstract

Green communication technology is expected to be widely adopted in future generation networks to improve energy efficiency and reliability of wireless communication network. Among the green communication technologies, simultaneous wireless information and power transfer (SWIPT) is adopted for its flexible energy harvesting technology through the radio frequency (RF) signal that is used for information transmission. Even though existing SWIPT techniques are flexible and adoptable for the wireless communication networks, the power and time resources of the signal need to be shared between information transmission and RF energy harvesting, and this compromises the quality of the signal. Therefore, SWIPT techniques need to be designed to allow an efficient resource allocation for communication and energy harvesting.

The goal of this thesis is to design SWIPT techniques that allow efficient, reliable and secure joint communications and power transference. A problem associated to SWIPT techniques combined with multicarrier signals is that the increased power requirements inherent to energy harvesting purposes can exacerbate nonlinear distortion effects at the transmitter. Therefore, we evaluate nonlinear distortion and present feasible solutions to mitigate the impact of nonlinear distortion effects on the performance. Another goal of the thesis is to take advantage of the energy harvesting signals in SWIPT techniques for channel estimation and security purposes. The performance of these SWIPT techniques is evaluated analytically, and those results are validated by simulations. It is shown that the proposed SWIPT schemes can have excellent performance, outperforming conventional SWIPT schemes.

Keywords: Simultaneous wireless information and power transfer, channel estimation, nonlinear distortion, physical layer security.

Resumo

Espera-se que as chamadas tecnologias de *green communications* sejam amplamente adotadas em futuras redes de comunicação sem fios para melhorar a sua eficiência energética a fiabilidade. Entre estas, encontram-se as tecnologias SWIPT (Simultaneous Wireless Information and Power Transference), nas quais um sinal radio é usado para transferir simultaneamente potência e informações. Embora as técnicas SWIPT existentes sejam flexíveis e adequadas para as redes de comunicações sem fios, os recursos de energia e tempo do sinal precisam ser compartilhados entre a transmissão de informações e de energia, o que pode comprometer a qualidade do sinal. Deste modo, as técnicas SWIPT precisam ser projetadas para permitir uma alocação eficiente de recursos para comunicação e recolha de energia.

O objetivo desta tese é desenvolver técnicas SWIPT que permitam transferência de energia e comunicações eficientes, fiáveis e seguras. Um problema associado às técnicas SWIPT combinadas com sinais multi-portadora são as dificuldades de amplificação inerentes à combinação de sinais de transmissão de energia com sinais de transferência de dados, que podem exacerbar os efeitos de distorção não-linear nos sinais transmitidos. Deste modo, um dos objectivos desta tese é avaliar o impacto da distorção não-linear em sinais SWIPT, e apresentar soluções viáveis para mitigar os efeitos da distorção não-linear no desempenho da transmissão de dados. Outro objetivo da tese é aproveitar as vantagens dos sinais de transferência de energia em técnicas SWIPT para efeitos de estimação de canal e segurança na comunicação. Os desempenhos dessas técnicas SWIPT são avaliados analiticamente, sendo os respectivos resultados validados por simulações. É mostrado que os esquemas SWIPT propostos podem ter excelente desempenho, superando esquemas SWIPT convencionais.

Palavras chave: SWIPT (Simultaneous Wireless and Power Transference), estimação de canal, distorção não-linear, segurança na camada física.

Contents

List of Figures

List of Tables

Acronyms

AIR	Achievable information rate 11, 29
AN	Artificial noise 3, 25, 77
AWGN	Additive white Gaussian noise 10, 29, 62, 80, 90
BER	Bit error rate 39
CFO	Carrier frequency offset 7, 25, 60
CP	Constellation point 28
CPs	Constellation points 28
CSI	Channel state information 24, 77
DC	Direct current 24
DFT	Discrete Fourier transform 18, 64
EH	Energy harvesting 8, 28, 61, 77
FDE	Frequency domain equalization 17, 60, 61
FDMA	Frequency division multiple access 1, 16
FS-SWIPT	Frequency splitting based SWIPT 3, 4, 38
HCS	Hybrid constellation shaping 4, 28, 104
HPA	High power amplifier 38
IB-DFE	Iterative block decision feedback equalization 5, 20, 60, 78, 89, 105
ID	Information decoding 31, 62
IDFT	Inverse discrete Fourier transform 18, 66
IMP	Intermodulation product 39
IoT	Internet of things 1, 8

ISI	Inter symbol interference 18
IT	Information transmission 28
MFB	Matched filter bound 21
MIMO	Multiple input and multiple output 22, 77, 105
MMSE	Minimum mean squared error 20
M-SWIPT	Modulation based SWIPT 4, 28, 104
NLD	Nonlinear distortion 38
OFDM	Orthogonal frequency division multiplexing 1, 38
OFDMA	Orthogonal frequency-division multiple access 60
PAPR	Peak to average power ratio 18, 38
PAS	Probabilistic amplitude shaping 28
PLNC	Physical layer network coded 78
PLS	Physical layer security 3, 25, 77
PS-SWIPT	Power splitting based SWIPT 4, 12, 31
QAM	Quadrature amplitude modulation 79, 96
QoS	Quality of service 2, 9
QPSK	Quadrature phase shift keying 62
RF	Radio frequency 1, 8
RF-EH	Radio frequency based energy harvesting 8
SC-FDE	Single carrier with frequency domain equalization 16, 60
SC-FDMA	Single carrier frequency division multiple access 2, 16, 60, 78, 90
SER	Symbol error rate 9, 29
SIC	Successive interference cancellation 22
SINR	Signal-to-interference plus noise ratio 25, 77
SNR	Signal-to-noise ratio 1, 10, 12, 29
SWIPT	Simultaneous wireless information and power transfer 1, 10, 28, 38, 60, 77
TDMA	Time division multiple access 1, 16
TS-SWIPT	Time switching based SWIPT 12
WCNs	Wireless communication networks 1, 8
WPT	Wireless power transfer 1, 9, 77

ZF Zero forcing 67, 85, 96

Symbols

$\mathbf{AIR}_M$	Maximum achievable information rate of a MS-SWIPT model 33
R_{ξ_1}	Total number of receiving antennas at ξ_1 91
R_{ξ_2}	Total number of receiving antennas at ξ_2 91
T_J	Total number of transmitting antennas at J 91
$\tilde{H}_{k,l}^{av}$	Average estimate of channel frequency response 64
$B_k^{(i)}$	Feedback coefficient in IB-DFE block, where i denotes the number of iteration in IBDFE 21
Δf	Carrier frequency offset 63
$\Delta \tilde{f}$	Carrier frequency offset estimate 64
$H_{TR}^{(k)}$	Channel link between legitimate transmitter (T) and receiver (R). Note: All channel links between 2 nodes follow same notation pattern in Chapter 6 and Chapter 7. 79
$\mathbb{C}$	Field of complex numbers 18
$\rho^{(i-1)}$	Correlation factor of data symbol in IB-DFE block 21
$A^{[s]}$	Constellation points in QAM, where s denotes the index of the constellation point 29
$A_d^{[s]}$	Constellation points selected for data transmission, where s denotes the index of the constellation point 29
$A_e^{[s]}$	Constellation points selected for energy transmission, where s denotes the index of the constellation point 29
Ns	Cyclic prefix 19
d_{TR}	The minimum distance between $\mathbf{x}_d$ and its neighbouring symbol 32
d_{TR}	The distance between T and R 30
$\mathfrak{E}_{MS}$	Energy harvested from MS-SWIPT 30

$\mathfrak{E}_{PS}$ Energy harvested from PS-SWIPT 12, 63
$\mathfrak{E}_{TS}$ Energy harvested from TS-SWIPT 15
$\wp$ Energy harvester at the legitimate receiver 78
E_S The total amount of energy present in EH symbols 30
E_e The total amount of energy present in EH symbols 30
$\tilde{H}_{k,l}^{(j)}$ Estimate of channel frequency response 64
$\tilde{Q}_{k,l}^{(\Delta f)}$ Estimate of SC-FDMA pilot symbol with carrier frequency offset Δf, where l denotes the index of carrier block in the signal and k denotes the index of symbol in the lth block. 64
$\tilde{X}_{k,l}^{(j,\Delta f)}$ Estimate of SC-FDMA data symbol with carrier frequency offset Δf, where j is the number of IB-DFE iteration, l denotes the index of carrier block in the signal and k denotes the index of symbol in the lth block. 64
ξ General notation for eavesdropper 78
ξ_1 First eavesdropper 90
ξ_2 eavesdropper 90
$\mathbb{E}[.]$ Expected value of a variable or an array 10

$\tilde{X}_{k,l,F}^{(j,\Delta f)}$ Final estimate of SC-FDMA data symbol with carrier frequency offset Δf, where j is the number of IB-DFE iteration, l denotes the index of carrier block in the signal and k denotes the index of symbol in the lth block. 64
$F_k^{(i)}$ Feed forward coefficient in IB-DFE block, where i denotes the number of iteration in IBDFE 21

γ Generic symbol for SNR of the received signal 10, 11
γ_{PS} SNR of the PS-SWIPT signal 12
γ_{TS} SNR of the TS-SWIPT signal 15
$\mathfrak{E}$ Generic symbol for the harvested energy from the RF signal 10

B_j HCS model, where j denotes a model in Table 3.1 35
$H_{k,l}$ Rayleigh fading channel 64

$\mathbb{I}$ Mutual information 11
MS_j MS-SWIPT technique based on j HCS model 35

$\rho(a)$ Non-uniform probability occurrences of a, where a is magnitude of the symbol 31

P_o Outage probabilty 11

θ_n Phase rotation of the symbol 63

P_I	Average power of data signal from MIMO/SISO transmitter 91
P_J	Power of jamming (EH) signal from a single antenna 91
P_x	Power of data signal 62
P_q	Power of pilot signal 62
$r(.)$	Pulse shaping filter 18
$\mathbf{SER}_{Cr}$	SER of the symbols present in the corner of QAM constellation 33
$\mathbf{SER}_{Ed}$	SER of the symbols present in the edge of QAM constellation 33
$\mathbf{SER}_{In}$	SER of the symbols present in the inner part of QAM constellation 33
$\mathbf{SER}_{M}$	SER of individual symbol present in QAM constellation 34
$H(\mathbf{x})$	Shannon entropy of the signal, where $\mathbf{x}$ is the signal 33
R_{tg}	Target bit rate 11
h	Channel co-efficient in time domain 29
P	Transmit power of the signal 29
T_s	Symbol time duration 17
T_X	Signal time duration 10
$\rho_u(a)$	Uniform probability occurrences of a, where a is magnitude of the symbol 31
$\varkappa$	Path loss factor of the RF signal in free space 10
$x_{n,d}$	Symbols used for data transmission is denoted in time domain 29
$x_{n,e}$	Symbols used for energy transmission is denoted in time domain 29
$X_{k,l}^{(\Delta f)}$	SC-FDMA data symbol with carrier frequency offset Δf, where l denotes the index of carrier block in the signal and k denotes the index of symbol in the lth block. 64
$x(t_i)$	Time domain signal at t_i time instance 18
$Y_{k,l,i}^{(\Delta f)}$	Received SC-FDMA signal with carrier frequency offset Δf, where l denotes the index of carrier block in the signal and k denotes the index of symbol in the lth block. 64
ζ	The value of $\frac{E_e}{E_S}$ 30
ζ_P	Percentage of the total transmit power allocated for information decoding in PS-SWIPT 13, 32, 62
ζ_T	Percentage of the total transmit time allocated for information decoding in TS-SWIPT 15

1

Introduction

1.1 Scope and motivation

The evolution of Wireless communication networks (WCNs) over past decades has drastically introduced many novel technologies to improve communication and provide a variety of services in all the aspects of human life. For example a single entity like Amazon Web Services platform offers a variety of solutions using WCNs and among them Internet of things (IoT) services and solutions operates/manages billions of communication devices for on-demand cloud computing platforms and application programming interfaces and so on. Therefore, an enormous increase in network equipment and service requirement for the WCNs increases the spectrum resource and energy consumption and the resource requirement will further increase for the future generation WCNs. Green communication is a paradigm that involves adopting all possible energy efficient hardware and communication practices, and providing novel ways to harvest energy from the renewal resources through unconventional and conventional means [1].

In this thesis, the practical application of energy harvesting solutions combined with energy efficient signal transmission techniques are discussed in detail. Among them, one of the most interesting energy harvesting techniques is harvesting energy from the Radio frequency (RF) signal, which is called Wireless power transfer (WPT). There are some special communication techniques which support energy harvesting by using RF signals and simultaneously allow information transmission, which is called Simultaneous wireless information and power transfer (SWIPT). Both WPT and SWIPT are explained detailedly in the following sections and SWIPT is the topic of interest in this thesis, mainly due to its adaptability with communication protocols and as a main enabling technique for green communication [2]. In general, the communication standards such as 4G and 5G adopt Frequency division multiple access (FDMA) and Time division multiple access (TDMA) for signal transmission and whereas FDMA is dominantly used for both uplink and downlink communication. While there are many existing SWIPT techniques that can be combined with Orthogonal frequency division multiplexing (OFDM), all the existing SWIPT techniques affect the Signal-to-noise ratio (SNR) of the transmitted data signal.

FDMA techniques such as Single carrier frequency division multiple access (SC-FDMA) and OFDM signal transmission techniques can be adopted with SWIPT technique for both energy harvesting purposes and to improve Quality of service (QoS). Especially when combining SWIPT with OFDM is a novel and interesting idea since OFDM has high data rate and can be used for both uplink and downlink in 3G, 4G and 5G communications. Therefore, this work introduces novel SWIPT techniques that are more suitable for FDMA than existing SWIPT techniques. This work also addresses exacerbation of nonlinear distortion associated with the multicarrier signal when adopting FDMA with SWIPT techniques.

In addition to introducing novel SWIPT techniques, there is an opportunity to address drawbacks of both the existing and novel SWIPT techniques. Also, there is huge scope for adopting SWIPT with signal processing applications like channel estimation and carrier frequency offset estimation, and for improving secrecy rate of information signal. Therefore, in this work, we explore SWIPT for these signal processing applications.

1.2 Problem introduction

The energy harvesting techniques like SWIPT techniques can be adopted with FDMA for indoor communication and vehicular communication technologies to improve energy efficiency and provide a flexible power source for very small sensor devices where battery or other power source is not feasible. One of the major challenges for communication between the transmitter and receiver is to know the channel state information between them for accurate information transmission. So, apart from using SWIPT techniques for transmitting information and power, SWIPT needs to perform channel estimation and needs to be adapted for security purposes. These additional functions allow SWIPT techniques not to be only an energy source but also to improve QoS. However, existing SWIPT techniques such as power splitting based SWIPT use excess power resources for channel estimation purposes, and this could affect the performance of the system in terms of energy efficiency. Therefore, novel SWIPT techniques are introduced in this thesis to address these issues.

This work also addresses the issues related to combining SWIPT with OFDM, and one of the main problems is the exacerbation of nonlinear distortion of the OFDM signal at the transmitter. OFDM signal suffers nonlinear distortion at the transmitter side when the OFDM signal is amplified with a high power amplifier. One of the reasons for nonlinearity is the peak to average power ratio of the signal, which can be exacerbated due to SWIPT techniques. Apart from energy harvesting, SWIPT techniques can also be used for other signal applications that can improve QoS. The main motivation of this work is to improve energy efficiency while providing flexible power supply for the network nodes and also to improve QoS.

On the other hand, when adopting SWIPT techniques to improve energy efficiency, the transmitted signal tends to have high power as in case of power splitting based SWIPT and this, in turn, leads to reducing secrecy of information components of the signal in a wiretap channel. To overcome this major drawback, there are already research works focussed on improving Physical layer security (PLS) by using security measures like introducing Artificial noise (AN) to jam eavesdroppers [3]. However, this leads to usage of additional power and network resources and therefore, we focus on reducing the resource usage and improving energy efficiency.

1.3 Research question and hypothesis

In this thesis, the following research questions and hypotheses were considered:

Research Question
Is it possible to use SWIPT techniques for channel estimation and/or security purposes in addition to its information transmission and energy harvesting functions?
Hypothesis
All the existing SWIPT techniques can be used for channel estimation and/or security purposes, however additional resources should be allocated for these purposes. Therefore, novel approaches should be adopted to optimize resource allocation for these purposes and explore alternative SWIPT techniques to address these issues.

Research Question
It is possible to accurately characterize nonlinearly distorted OFDM signals when it is combined with SWIPT technique and whether it will be useful for improving information decoding?
Hypothesis
Although in general it is difficult to analyse nonlinear effects in communication systems, the Gaussian-like nature of multicarrier signals can be used to simplify the intermodulation analysis, providing a simple, yet accurate, framework for an analytical performance evaluation of nonlinear effects on SWIPT signals, both for conventional and optimum receivers.

Research Question
It is possible to adopt a SWIPT technique with OFDM signal that specifically takes advantage of frequency division method without affecting the SNR of the signal?
Hypothesis
In general, all the existing SWIPT techniques can be adopted with OFDM but SNR of the signal is reduced due to power allocation from the RF signal for energy harvesting purposes. Yet, it is possible to adopt Frequency splitting based SWIPT (FS-SWIPT) with OFDM, which takes advantage of frequency division method to segregate symbols used for energy harvesting purposes from other symbols and avoids allocating power resources from the symbols that are used for information transmission. However, as compared to other SWIPT techniques, FS-SWIPT increases nonlinear distortion of the signal which

subsequently degrades the SNR of the signal. But this problem can be reduced through a proper nonlinear distortion compensation technique.

1.4 Contribution

We introduces a novel SWIPT technique called Modulation based SWIPT (M-SWIPT), where the transmitter adopts high amplitude symbols for energy transfer and low amplitude symbols for information transmission. Since the characteristics of M-SWIPT technique depend on the signal modulation scheme, we define a generic M-SWIPT technique for M-QAM and further improvise the performance of M-SWIPT by shaping the constellation points of the modulated signal. In general, the error rate performance and achievable information rate of the M-SWIPT should be lower than the existing model such as Power splitting based SWIPT (PS-SWIPT), since high amplitude symbols are not used for information transmission purpose and to reduce these impacts, we adopt non uniform M-QAM constellation points. Therefore, we introduce a new constellation shaping technique called Hybrid constellation shaping (HCS) to shape the constellation points of the M-QAM signal. With the help of HCS, we could increase the maximum achievable information rate of the signal in M-SWIPT than that of PS-SWIPT, while maintaining the error rate performance comparably similar to that of PS-SWIPT. We study the advantages and disadvantages of M-SWIPT technique over PS-SWIPT with different HCS levels and study the impact of HCS on M-SWIPT technique. An exceptionally good achievable information rate performance at low SNR region is one of the key features of M-SWIPT technique.

We study another novel SWIPT technique called FS-SWIPT, where the transmitter adopts a multi-carrier signal transmission scheme i.e. OFDM with FS-SWIPT, in which high frequency signal carriers are used for energy transfer and low frequency signal carriers for information transmission. We present a simple, yet accurate analytical characterization of FS-SWIPT signals submitted to nonlinear devices. This characterization combines the use of Bussgang theorem, to decompose the nonlinearly distorted signal as the sum of uncorrelated useful and distortion terms, with the spectral characterization of those signals using intermodulation product (IMP) analysis. This characterization is then used to obtain the signal-to-noise plus interference levels for the different subcarriers. It is shown that performance degradation due to nonlinear effects on FS-SWIPT signals are much higher than with conventional OFDM signals, especially for the data subcarriers close to the EH subcarriers. We present an iterative receiver, inspired based on Bussgang receivers for conventional OFDM signals, that estimates and cancels NLD effects. It is shown that, in spite of the stronger NLD effects, we can still have good performance with that iterative receiver. The good performance of this receiver is due to the fact that the signals associated with high-power EH subcarriers are known and do not need to be estimated, leading to more accurate estimates of the NLD term, even in the presence of decision errors in the data estimates. Therefore, by employing this receiver the bit error rate (BER) of nonlinear FS-SWIPT signals can almost match the BER associated with linear transmissions. Finally, we study the optimum performance of nonlinearly distorted FS-SWIPT signals. Contrarily to the OFDM case, where stronger NLD levels can lead to higher performance gains for the optimum receiver, it is shown that performance gains for the nonlinear FS-SWIPT case relatively decrease with the increase in the power of the EH component. However, the NLD can still lead to performance improvements when compared with the linear transmission scenario.

We design a receiver for SWIPT with joint CFO and channel estimation. The pilot symbols, which are superimposed, with the information symbols are used for EH, CFO and channel estimation. Here, the overall transmit power of the pilot signal is higher than that of other competitive models such as techniques which employ multiplexing pilot symbols with the information symbols. We improve the channel estimation accuracy with the help of Iterative block decision feedback equalization (IB-DFE) and an algorithm is introduced with IB-DFE to increase the accuracy of the channel estimation with the estimated feedback in IB-DFE. We find the minimum power required for the pilot signal to estimate the channel condition and CFO with achievable accuracy for the given power of the information signal. Also, we find the optimum power allocation ratio between the information and the pilot signals by using simulation results.

We present two wiretap physical layer security models in two different scenarios and study threats from passive and active eavesdroppers, further we provide countermeasures against those eavesdroppers and improve the secrecy rate of legitimate networks. In both the models, energy harvesting signals are used as jamming signals against eavesdroppers. The first model explains the impact of high channel correlation between legitimate receiver and eavesdropper and provides solutions by using IBDFE to improve the secrecy rate of the legitimate network. The second model presents a solution to overcome challenges posed by two active cooperative eavesdroppers, where one located near the transmitter and other located near the receiver of the legitimate network. Both eavesdroppers estimate both jamming and information signals separately and share the estimates to improve the accuracy of estimation. Even though we present robust cooperative eavesdroppers, we could present solutions based on the analysis antenna diversity order and transmission power of jamming and information signals. The secrecy rate of legitimate networks is improved by adopting an IB-DFE receiver and by optimising the transmit power of information and jamming signals.

The list of publications during the PhD period are as follows:

Journal Papers:

1 Akashkumar Rajaram; Rui Dinis; Dushantha Nalin k. Jayakody; Neeraj Kumar, "**Receiver Design to Employ Simultaneous Wireless Information and Power Transmission for Joint CFO and Channel Estimation**," *IEEE Access*, Jan. 2019.

2 Akashkumar Rajaram; Rabia Khan; Selvakumar Tharranetharan; Dushantha Jayakody;

Rui Dinis; Stefan Panic, "**Novel SWIPT Schemes for 5G Wireless Networks**", *Sensors* 2019.

3 Akashkumar Rajaram; Dushantha Nalin K. Jayakody; Bin Chen; Rui Dinis; Sofine Affes, "**Modulation-based Simultaneous Wireless Information and Power Transfer**", *IEEE Communication Letters*, Oct. 2019.

4 Akashkumar Rajaram; Rui Dinis; Dushantha Nalin K. Jayakody; M. Beko, "**Secure Information Transmission with Self Jamming SWIPT**," *Electronics*, vol. 9, no. 4, p. 587, Mar. 2020.

5 Akashkumar Rajaram; Rui Dinis; Dushantha Nalin K. Jayakody; M. Beko, "**Energy efficient secure communication model against cooperative eavesdropper**,"*Applied Sciences*, Vol. 11, Issue. 4, p. 1563. Jan. 2021.

6 Akashkumar Rajaram ; Joao Madeira, Rui Dinis, Dushantha Nalin K. Jayakody, Marko Beko, "**Frequency-Splitting SWIPT with Strong Nonlinear distortion Effects : An Efficient Technique for IoT Systems**," *IEEE Internet of Things Journal*, 2022. (Submitted)

Conference papers:

1 Sangay Chedup; Bevek Subba; Sonam Dorji; Tharindu Perera; Akashkumar Rajaram; Dushantha Nalin K Jayakody, "**Visible Light Energy Harvesting in Modern Communication Systems**," *International Conference on Electrical, Electronics, Computer, Communication, Mechanical and Computing*, Jan. 2018.

2 Tharindu Perera; Akashkumar Rajaram; Sangay Chedup; Dushantha Jayakody, "**Hybrid RF/Visible Light Communication in Downlink Wireless System**", *International Conf. on Communication, Management and Information Technology*, Mar. 2018.

3 Pedro Viegas, David Borges, Akashkumar Rajaram, Dushantha Jayakody, Paulo Carvalho, Rui Dinis and João Oliveira, "**Applying energy efficient physical layer security into spatial multiplexed massive MIMO point-to-point communications**", *International Conf. on Emerging Technologies of Information and Communications* (ETIC), 2019. 7

4 David Borges, Guilherme Gaspar, Paulo Carvalho, Akashkumar Rajaram, Nalin D. K. Jayakody and Rui Dinis, "**Low Complexity Channel Estimation for Multi-user Massive MIMO Systems with Pilot Contamination**", *ETIC*, 2019.

5 Akashkumar Rajaram ; Joao Madeira, Rui Dinis, Dushantha Nalin K. Jayakody, Marko Beko ; "**Performance Evaluation of Nonlinear Effects in Frequency-Splitting SWIPT Signals**," *VTC* May. 2020.

6 Akashkumar Rajaram, David Borges, Paulo Montezuma, Rui Dinis, Dushnatha Nalin K. Jayakody, and Marko Beko. "**Joint Channel and Information Estimation on Symbol Decomposition-Based Secure Point-to-Point Communications**."*In Doctoral Conference on Computing, Electrical and Industrial Systems, Springer, Cham*, , pp. 137-146, 2020.

7 David Borges, Akashkumar Rajaram, Paulo. Montezuma, Rui Dinis and Marko Beko, "**Nonlinear Distortion Effects in Secure Energy Efficient MIMO Systems**,"*2020 12th International Symposium on Communication Systems, Networks and Digital Signal Processing (CSNDSP)*, pp. 1-4, 2020.

8 Akashkumar Rajaram ; Joao Guerreiro, Rui Dinis, Dushantha Nalin K. Jayakody ; "**Frequency-Splitting SWIPT with Joint Signal Detection and Nonlinear Distortion Compensation**," *ICECCME* July. 2021.

1.5 Outline

The outline of this thesis is as follows:

Chapter 2 includes the introduction to RF energy harvesting and SWIPT techniques and explains the necessity for novel SWIPT techniques. Apart from this, the introduction includes the basics of signal transmission schemes, channel estimation technique and physical layer security models that can be combined with the SWIPT systems.

Chapter 3 introduces M-SWIPT technique and studies the error rate and achievable rate of SWIPT. The performances of M-SWIPT based on four different HCS models are compared with PS-SWIPT based on the theoretical and simulated results.

Chapter 4 introduces another novel SWIPT technique called FS-SWIPT, which can effectively adopt an OFDM multi carrier signal. The chapter provides a novel solution to address nonlinear distortion effects associated with the high data rate OFDM signal.

Chapter 5 presents a robust channel estimation technique combined with SWIPT to provide accurate channel and Carrier frequency offset (CFO) estimates, making it particularly interesting for fast fading channel links. Furthermore, the chapter provides an analysis of optimum power allocation ratio between data and pilot symbols.

Chapter 6 presents two wiretap physical layer security models, the first model presents a wiretap channel with passive eavesdroppers and it is assumed that they are closely located to the receiver with high channel correlation. The second model presents more challenging circumstances, where two eavesdroppers cooperate with each other to estimate both jamming and information signals. The study explains the impact of channel estimation errors, and channel correlations between the eavesdroppers and the legitimate network. Further, feasible solutions to improve the secrecy rate of these models are provided in this chapter.

Chapter 7 provides the conclusion and future work of this thesis.

2

Literature review

2.1 Energy harvesting in wireless communication

Energy harvesting (EH) in wireless communication networks is one of the enabling technologies for future generation networks [2]. EH is a green communication scheme for harvesting energy from RF signals [4]. In the age of modern wireless communication networks, the advancement of communication protocols and wireless communication devices, supported by other technological innovations in the engineering fields have resulted in rapid development and utilization of wireless communication devices like sensor devices for many applications. The application of sensor devices with IoT technologies have deeply impacted every aspect of human life. The emergence of IoT sensors have underscored the need of WCNs for assisting our day to day life activities. The increase in the growing number of sensor devices has resulted in increased demand for energy and other radio resources. Therefore, efficient energy and radio resources management is required to support the evolving wireless communications network. Efficient energy resource management provides huge opportunities for the researchers to innovate new technologies and they are specifically focused on technologies to conserve and harvest energy from the available resources. These energy efficient technologies are standardized and incorporated in the green communication paradigm [2].

There are many energy harvesting techniques available for wireless communication networks. Among these techniques, there are notable renewable EH techniques that use solar energy, wind energy and piezoelectricity and so on. Another unconventional energy harvesting technique is Radio frequency based energy harvesting (RF-EH). RF-EH in wireless communication is a green communication technology which allows communication devices to harvest energy from the received RF signals There are several advantages in adopting RF-EH for sensors over conventional harvesting techniques. The drawbacks in adopting conventional techniques (like solar energy, wind energy and piezoelectricity) with sensors are mainly due to factors like size and locations of the sensor devices. In many practical communication scenarios without access to natural light or wind sources, conventional energy harvesting techniques are not applicable, which motivates the concept of wireless RF-EH. RF-EH and energy transfer has been regarded as a promising avenue for power constrained wireless networks and harvesting typically refers to the capability of wireless devices to convert the received RF signals into usable energy, while the RF energy transfer refers to delivering energy associated with the RF signal from a transmitter to a receiver by leveraging the far-field radiation properties of electromagnetic waves.

Traditionally, the wireless terminals are normally powered by the batteries with limited operation duration. Frequent battery recharging/replacement is inconvenient due to huge numbers of devices in use, hazardous for the devices located in toxic environments, or even impracticable in many applications, e.g., medical devices. In these scenarios, the RF energy harvesting technique becomes an attractive approach to charge the batteries of wireless devices. The feasibility of this technique has been experimentally demonstrated by prototypes, such as [5]. This results in significant gains in terms of spectral efficiency, time delay, and the energy consumption. Based on the source of RF signals for energy harvesting, there are two types of harvesting techniques, dedicated and ambient RF energy harvesting techniques. Dedicated RF energy harvesting technique refers to transmitting RF signal solely for the purpose of energy harvesting purpose and in most cases, the RF signal is transmitted with a comparatively higher power level than the signal normally used for information transmission purpose. Ambient RF energy harvesting technique refers to utilizing ambient RF signals irrespective of their power level for energy harvesting purposes. Due to the fact that ambient RF signals are freely available, it is more beneficial to adapt ambient RF energy harvesting techniques than adopting dedicated RF energy harvesting techniques [6] but ambient RF signals are uncontrollable and unpredictable.

In the dedicated RF energy harvesting technique, a transmitter adopts WPT protocol under which a dedicated high power RF signal is transmitted solely for the purpose of RF energy harvesting. One of the main disadvantages of WPT is the amount of time allocated for transmitting information is reduced due to energy harvesting purpose, this in turn degrades the Symbol error rate (SER) performance and outage probability of signal increases with the time allocated for energy harvesting purposes. However, WPT is used in cooperative communication and can be effectively used in the available time slots which are not used for information transmission [7], [8]. The sensor nodes which harvest energy from the dedicated high power signal can also take advantage of the broadcasted information signal for harvesting energy. The results of [7], [8] shows that the adopting WPT in cooperative communication networks is beneficial in increasing energy efficiency and also increases the QoS. The increase in number of nodes allows the cooperative communication networks to be more flexible in harvesting energy, this improves SER and outage probability performance of the received signal.

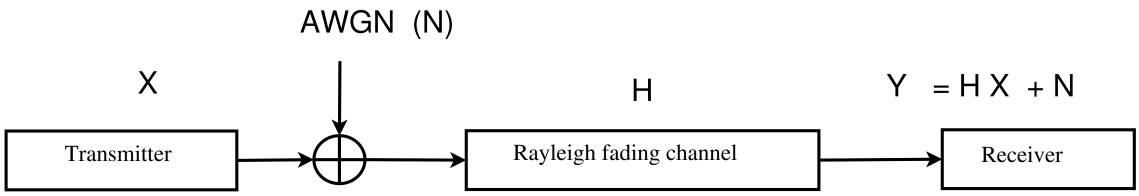

Figure 2.1: Rayleigh fading channel with AWGN and power constraint

The amount of harvesting energy from the received signal for a given time T_X is

$$\mathfrak{E} = \frac{\eta_{eh} P|H|^2 T_X}{d^{\varkappa}}. \tag{2.1}$$

where $\mathfrak{E}$ is the harvested energy, η_{eh} is the rectenna conversion efficiency and P is the power of the received signal. H is the channel coefficient, d is the distance between the transmitter and the receiver, and $\varkappa$ is the path loss factor.

However, WPT has one major drawback as this technique does not allow the receiver to harvest energy and receive information at the same time slot. Even though cooperative communication networks can allocate time slots in an opportunistic way, this does not allow the receiver to share the same time slot for both the functions. In order to overcome this drawback, researchers have envisaged another major technique called SWIPT in which dedicated RF signals can be adopted for both energy harvesting and information transmission purposes.

Throughout all the chapters, matrices or vectors are denoted by bold letters and scalar variables are denoted by italic letters. The variables associated to frequency domain and time domain are denoted by capital letters and small letters, respectively. $(.)^*$, $(.)^T$, $(.)^H$, $||.||$, $\mathbb{E}[.]$ and γ denotes the conjugate, transpose, Hermitian, trace, expectation operation, SNR of the received signal respectively.

2.1.1 Wireless channel capacity

The capacity of the channel is defined in [9] as the maximum of the mutual information between the input and the output over all distributions on the input that satisfy the power constraint. Channel capacity is derived for various communication scenarios by Claude E. Shannon [10]. It characterizes the maximum information rate for which reliable communications are possible. Let us consider a simple communication model as in Fig. 2.1 and the received signal Y at the receiver is given as

$$Y = \sqrt{P}HX + N, \tag{2.2}$$

where X, H, P and N are the modulated signal, the channel fading coefficient, the power constraint of the signal and the Additive white Gaussian noise (AWGN), respectively. The channel capacity of Rayleigh fading channel is given as

$$C(H;\gamma) = \mathbb{E}\{\log_2(1 + |H|^2\gamma)\}, \tag{2.3}$$

where γ is the signal to noise ratio. γ is expressed as

$$\gamma = \frac{\text{Power constraint of signal}}{\text{Power constraint of noise}} = \frac{\mathbb{E}[(\sqrt{P})^2]}{\mathbb{E}[N^2]} = \frac{\mathbb{E}[(\sqrt{P})^2]}{\mathbb{E}[N^2]} = \frac{P}{N_0},$$

where N_0 is noise spectral density power. P_o is denoted as the outage probability of a wireless communication channel, which is dependent on the channel capacity C and target rate R_{tg}. If the channel capacity is less than the target rate then an outage event occurs.

$$\begin{aligned} P_o = Pr(C(H;\gamma) < R_{tg}) &= Pr(\mathbb{E}\{\log_2(1+|H|^2\gamma)\} < R_{tg}) \\ &= Pr(R_i < R_{tg}), \end{aligned} \tag{2.4}$$

where R_i is the information rate of the signal based on the channel condition and P_o is the probability event. $Pr(R_i)$ can be expressed using the probability density function of Rayleigh fading channel and γ is distributed according to the exponential distribution [11, Sec. 2.2.1], and P_o is given as

$$P_o = 1 - \exp\left(-\frac{R_{tg}}{\gamma}\right). \tag{2.5}$$

The channel mutual information represents an upper limit or maximum limit of the Achievable information rate (AIR) for a signal based on its given modulation format in an information-theoretic perspective. In general, for any modulation scheme, the generated bits are assumed as in uniform distribution. Bits are denoted as b_i, where $i = 1, 2, ...m$ and $m = 2\log_2 M$ and M is the total number of constellation points in a quadrature amplitude modulation. Similarly, the modulated symbols i.e. X generated by using these bits are in uniform distribution. The following mutual information definitions are derived in [12], [13]. The generalized mutual information for a bit-wise decoder in a memoryless channel is denoted as $\mathbb{I}_b$, which is given as

$$\mathbb{I}_b = \sum_{i=1}^{m} \mathbb{I}(b_i; Y) = \sum_{i=1}^{m} \mathbb{E}\left[\log_2 \frac{p_{Y|b_i}(Y|b_i)}{p_Y(Y)}\right], \tag{2.6}$$

where b_i is a discrete random input and its corresponding continuous output is $Y = [Y_1, Y_2, ...Y_n]$. $p_{Y|b_i}$ the channel transition probability of the channel, $\mathbb{I}$ denotes mutual information, then $\mathbb{I}(b_i; Y)$ is the mutual information between the bits and the output symbols. Similarly, the generalized mutual information for a symbol-wise decoder in a memoryless channel is denoted as $\mathbb{I}_S$, which is given as

$$\mathbb{I}_S = \frac{1}{n}\mathbb{I}(X; Y) = \frac{1}{n}\sum_{i=1}^{m} \mathbb{E}\left[\log_2 \frac{p_{Y|X}(Y|X)}{p_Y(Y)}\right], \tag{2.7}$$

where $X = [X_1, X_2, ...X_n]$ is a discrete random input and its corresponding continuous output is $Y = [Y_1, Y_2, ...Y_n]$. Based on the symbol wise mutual information, the AIR for symbol wise decoder can be computed [14, Sec. VI]. In chapter 3, we use $\mathbb{I}_S$ for computing AIR of signal with on-uniform and non-equidistant constellation point distribution.

2.2 Simultaneous wireless information and power transfer

This technique allows the receiver to simultaneously harvest energy and decode information by using various strategies and receiver architectures. Traditionally, based on the receiver architectures, SWIPT are classified into four types, they are: separate antenna architecture based SWIPT, Time switching based SWIPT (TS-SWIPT), PS-SWIPT and Antenna switching based SWIPT [4]. Types of SWIPT based on antenna architecture are given in Fig. 2.2.

- **Separate antenna architecture**: In this architecture, receiver uses separate rectenna for energy harvesting and another antenna for information decoding (ID), this architecture has very simplistic approach and it will not affect the performance of information decoding process [15].

- **Antenna switching architecture**: This architecture is similar to separate antenna architecture, however, in this architecture a set of antennas is used for ID and a set of antennas is used for EH. The number of antennas used for EH and ID can be allocated based on the requirement of energy needs. Also this architecture can be adapted with PS-SWIPT to optimize power allocation [16].

The main drawback of having a dedicated antenna for energy harvesting and also antenna switching architecture is that it can not be adopted by single antenna sensor devices. Therefore due to hardware restriction, power splitting architecture and time switching architecture could be adopted for SWIPT schemes in sensor devices.

- **Power splitting architecture**: In this architecture, the receiver shares the same antenna for EH and ID, and the receiver uses a special circuit to divide the power of the received signal for EH and ID. This enables the receiver to adjust the available energy resources between the EH and ID process. The PS-SWIPT architecture is given in Fig. 2.3.

  In PS-SWIPT, the amount of harvesting energy from the received signal is denoted as Ł_{PS}, which is expressed as

  $$\text{Ł}_{PS} = \frac{\eta_{eh} P(1-\zeta_P)|H|^2 t}{d^{\varkappa}}, \tag{2.8}$$

  where $(1-\zeta_P)$ is the percentage of power allocated for energy harvesting.

  This power allocation can directly reduce SNR of the received signal during information decoding. The SNR of signal with PS-SWIPT is denoted as γ_{PS}, which is given as

  $$\gamma_{PS} = \frac{P\zeta_P |H|^2 d^{-\varkappa}}{N_0}, \tag{2.9}$$

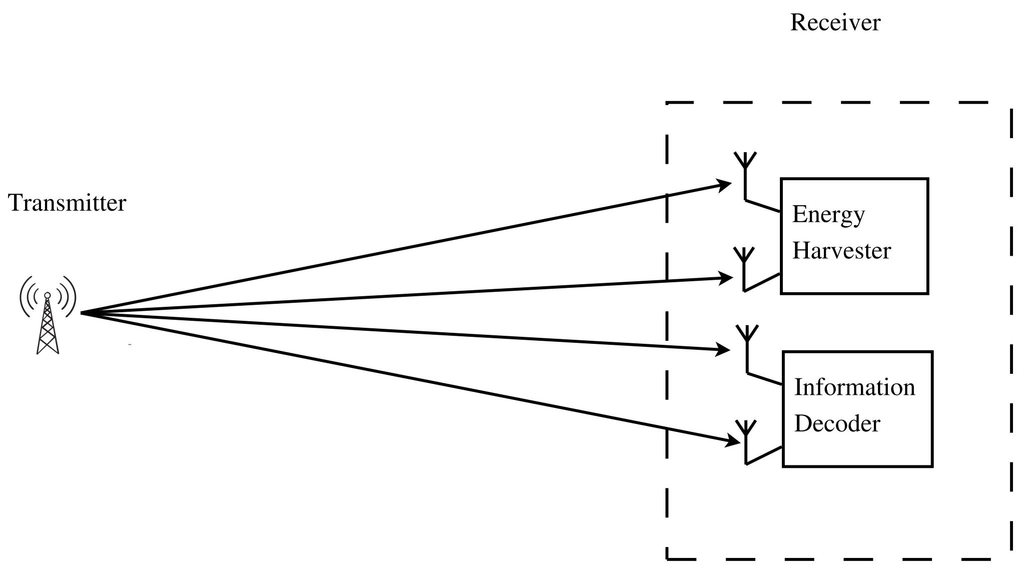

1. Seperate antenna architecture based SWIPT

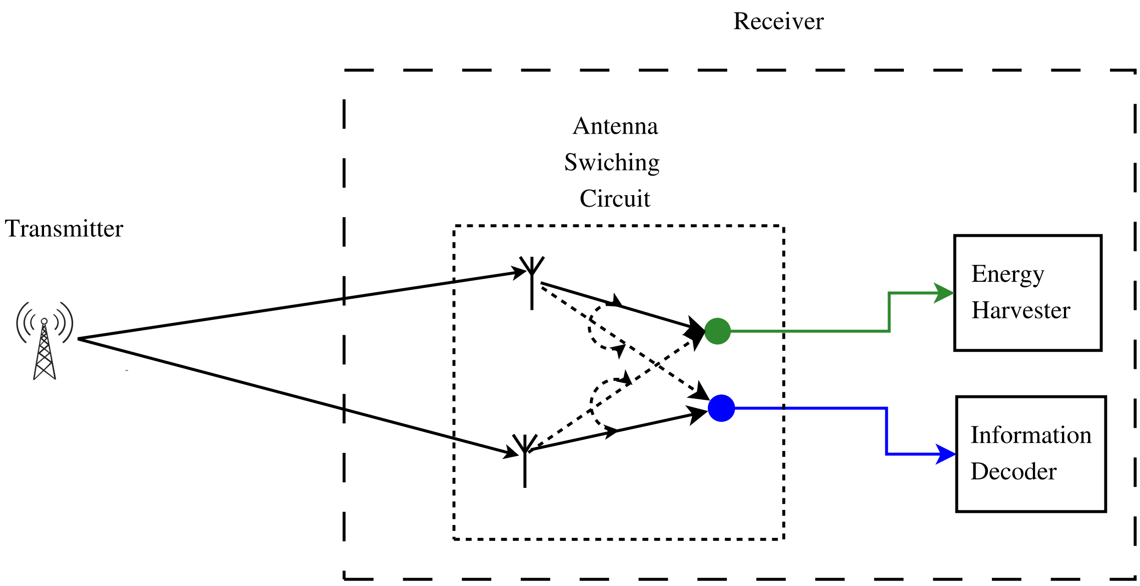

2. Antenna switching architecture based SWIPT

Figure 2.2: SWIPT based on antenna architecture.

where N_0 is the power of noise and ζ_P is the percentage of power remaining in the signal after energy harvesting. The SNR affects both SER and outage probability.

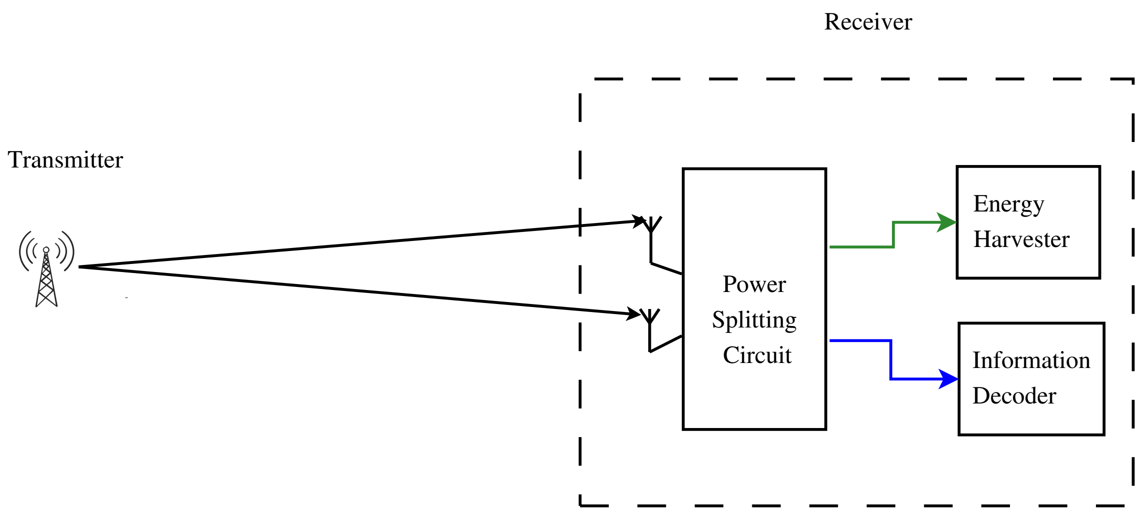

3. Power splitting architecture based SWIPT

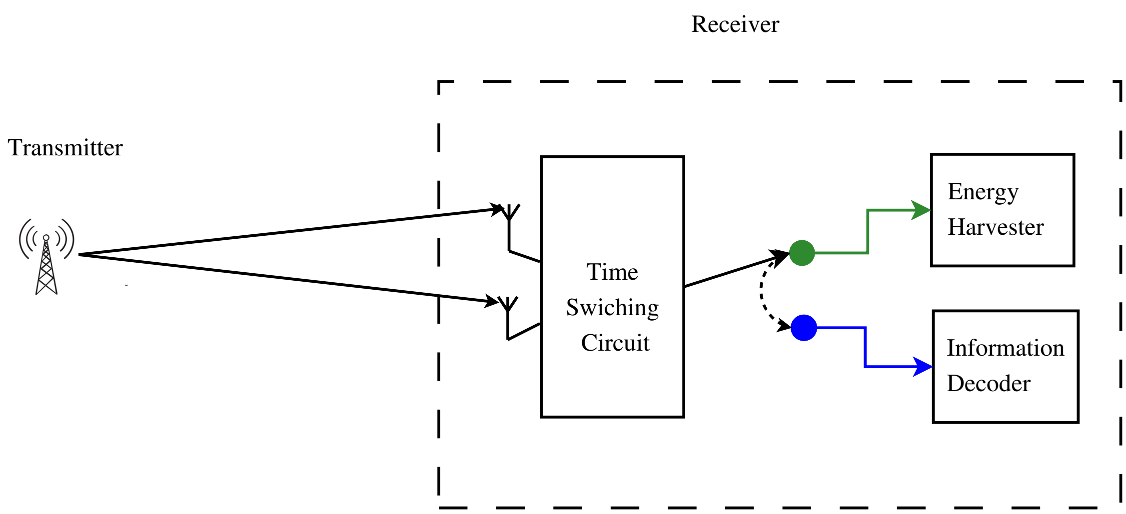

4. Time switching architecture based SWIPT

Figure 2.3: PS-SWIPT and TS-SWIPT architectures.

The outage probability of the PS-SWIPT is given as

$$\begin{aligned}\Pr(\text{PS}) &= Pr\left(\gamma_{PS} < 2^{\left(\frac{R_{tg}}{T_X}\right)} - 1\right) \\ &= 1 - \exp\left(-\frac{2^{\left(\frac{R_{tg}}{T_X}\right)} - 1}{\gamma_{PS}}\right),\end{aligned} \tag{2.10}$$

where R_{tg} is the target bit rate, which is bits per channel use. Therefore, SNR can directly increase the outage probability of the received signal.

- **Time switching architecture**: In this architecture, the receiver shares the same antenna for EH and ID, and uses a special circuit that periodically switches the antenna for EH and ID. The TS-SWIPT architecture is given in Fig. 2.3. In TS-SWIPT , the amount of harvesting energy from the received signal is denoted as $\mathfrak{E}_{TS}$, which is expressed as

$$\mathfrak{E}_{TS} = \frac{\eta_{eh} T_X (1-\zeta_T) P |H|^2}{d^{\varkappa}}, \tag{2.11}$$

where ζ_T is the percentage of time allocated for information decoding and $(1-\zeta_T)$ is the percentage of time allocated for energy harvesting. This directly reduces the total energy harvested from the signal as the time allocated for energy harvesting indirectly affects the total power of the signal. The amount of energy is measured in Joules and the power is measured in Joules per second, so the time allocated for energy harvesting directly reduces the power of the signal. The SNR of signal with TS-SWIPT is denoted as γ_{TS}, which is given as

$$\gamma_{TS} = \frac{T_X (1-\zeta_T) P |H|^2 d^{-\varkappa}}{N_0}, \tag{2.12}$$

where E is the total energy of the received signal. The amount of total received power is reduced due to time allocated for energy harvesting. Therefore, TS-SWIPT suffers SNR degradation at the receiver due to energy harvesting and the overall signal throughput is lost due to time resource allocation for the energy harvesting process. The outage probability of TS-SWIPT is given as

$$\begin{aligned}\Pr(\text{TS}) &= Pr\left(\gamma_{TS} < 2^{\left(\frac{\text{R}}{T_X \zeta_T}\right)}\right) \\ &= 1 - \exp\left(-\frac{2^{\left(\frac{\text{R}}{T_X \zeta_T}\right)} - 1}{\gamma_{TS}}\right).\end{aligned} \tag{2.13}$$

The reduction in time leads to reduced throughput and leads to SNR degradation which in turn increases outage probability of the given signal.

Thus, we understand that all the existing SWIPT techniques suffer performance degradation due to resource allocation for energy harvesting purposes. Furthermore, the performance analysis of PS-SWIPT in [17] explains the trade off between the performance of the received signal and energy harvested from the received signal. The performance metric like information rate, symbol error rate indicates that lower amplitude symbols of the M-ary modulated signal suffer excessively as compared to higher modulated signal due to power loss.

Therefore, a novel approach envisaged to adopt symbol wise energy harvesting technique in SWIPT and this technique is called Modulation based simultaneous wireless information and power transfer (M-SWIPT) [18]. Another approach to allocate by using a specific symbol for EH called FS-SWIPT is used in [19]. These two techniques explore unique ways to allocate a specific set of symbols for EH and the remaining set of symbols for ID.

Traditional SWIPT techniques which are based on power splitting, time switching and antenna splitting schemes allocate power, time and hardware resources respectively, between data and energy transmission. Whereas both M-SWIPT and FS-SWIPT allocate specific symbols for data transmission and remainders for energy transmission. The idea of using transmitted symbols as a resource will allow the system to improve its performance and as an additional benefit, the symbols allocated for energy harvesting can be exploited for other signal processing applications. M-SWIPT technique can be adopted with time division multiple access (TDMA) and also with frequency division multiple access (FDMA) signal transmission techniques, whereas FS-SWIPT can be only adopted with FDMA. Therefore, in this thesis novel SWIPT techniques such as M-SWIPT and FS-SWIPT are studied and analysed in following chapters for practical applications.

2.3 Frequency-division multiple access

FDMA is a channel access technique which allows multiple network nodes in the physical layer to transmit and receive at the same time. This technique separates channels by frequency and allows the nodes to transmit and/or receive signals in different frequencies. The FDMA technique has several advantages over TDMA, mainly the spectrum bandwidth can be allocated based on its different frequency band for multiple nodes to communicate at the same instant. Due to the versatility and adaptability of FDMA, FDMA is most commonly adopted in 4G and 5G communications as compared to TDMA. There are many FDMA techniques used in wireless communication and among them, the most common FDMA techniques are orthogonal FDMA technique and single carrier FDMA. While SC-FDMA as the name implies, it can be used for single carrier based communication and OFDMA can be used for both multiple carrier and single carrier communication. OFDMA is most suitable for multiple carrier communication as compared to SC-FDMA. SC-FDMA based on discrete Fourier transform spread OFDM (DFT–S–OFDM) is used for the uplink in 5G [20] and SC-FDMA specially useful for combining FDMA technique with SWIPT in a point to point communication model of 5G networks. So, both 4G and 5G networks use multi carrier and single carrier waveforms. The SC for uplink and MC modulation for downlink is proved to be the best choice [21]. The Single carrier with frequency domain equalization (SC-FDE) is the combination of single carrier modulation with the Frequency domain equalization (FDE), which is found to be suitable for the transmission of high data rate signal over severely time dispersive channels for single user than OFDM and OFDMA is most suitable for transmitting high data rate signal for multiple users at the same time slot [21].

Fig. 2.4, Fig. 2.5 and Fig. 2.7 illustrates the simple block diagram of the transmitter and receiver section of OFDMA, SC-FDE and SC-FDMA, respectively.

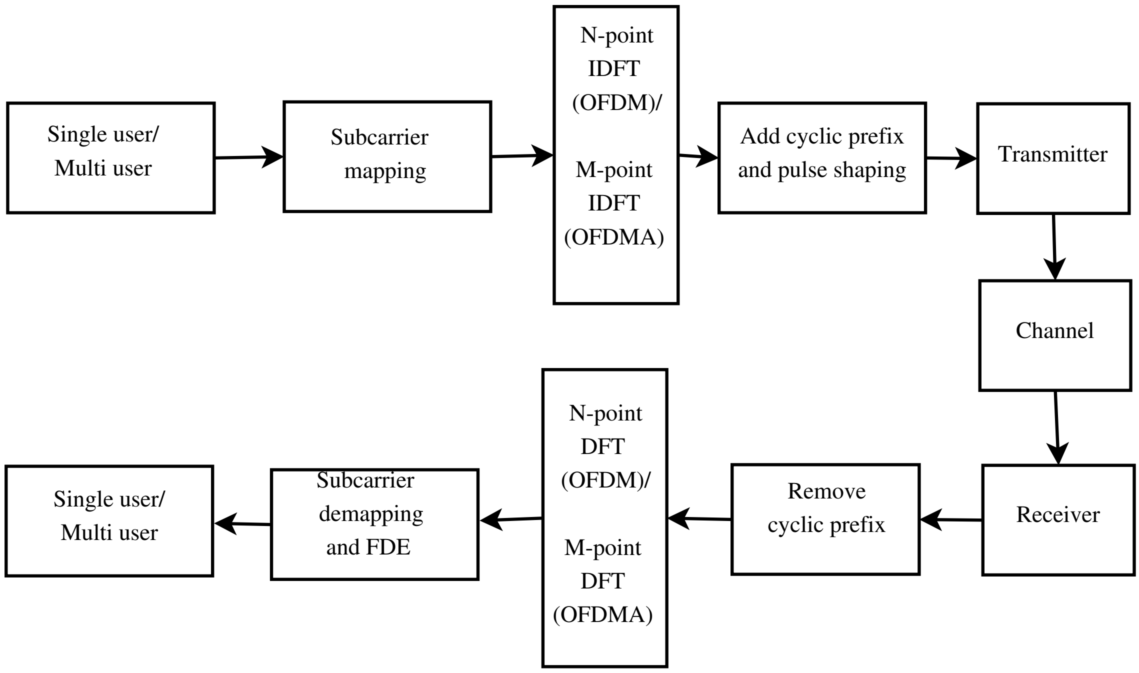

Figure 2.4: Block diagram of transmitter and receiver section of OFDM (single user)/ OFDMA (multi user).

2.3.1 Orthogonal Frequency division multiple access

The 'Orthogonal' FDMA is a special case of FDMA, where all the subcarriers in OFDMA signal are the multiple of a fundamental integral component that forms an orthogonal relation between them. The main advantage of OFDMA is the possibility of parallel transmission of all the subcarriers and therefore OFDMA results in a high data rate. Commonly in FDMA, multiple subcarriers are used in different frequencies f_c, where $c \in \{1, 2, \ldots, N-1\}$ and the subcarriers are filtered based on f_c. Whereas in OFDMA, specific frequency interval is allotted in between each subcarrier inorder to improve the spectral efficiency of the OFDMA signals and to maintain orthogonality between the subcarriers. The interval between each subcarrier is $1/T_s$, where T_s is the symbol time duration. The complex envelope of an OFDM signal or an OFDMA signal of a given time instant t_i is denoted as $x(t_i)$, which is expressed as

$$x(t_i) = \sum_{k=0}^{N-1} X_k \exp\left(j2\pi k \frac{t}{T_s}\right) w(t_i), \;\; 0 \leq t_i < T_s, \tag{2.14}$$

where X_k is the data symbol of k^{th} subcarrier with $k = 1, 2, \ldots, N-1$ and $w(t_i) = r\left(\frac{t}{T_s}\right)$, where $r(.)$ is the pulse shaping filter function. The waveform of k^{th} subcarrier is $\phi_k(t_i) = \exp\left(j2\pi k \frac{t}{T_s}\right)$. The orthogonality property of OFDMA signal can be proved by the dot product of $\phi_k(t_i)$ and $\phi_{k'}(t_i)$,

$$\begin{aligned} \langle \phi_k(t_i), \phi_{k'}(t_i) \rangle =& \frac{1}{T} \int_0^T \left(\exp\left(j2\pi k \frac{t}{T_s}\right)\right)\left(\exp\left(-j2\pi k' \frac{t}{T_s}\right)\right) dt \\ =& \frac{1}{T} \int_0^T \exp\left(j2\pi (k-k') \frac{t}{T_s}\right) dt \\ =& \begin{cases} 1, & k = k' \\ 0, & k \neq k'. \end{cases} \end{aligned} \tag{2.15}$$

The OFDMA signal i.e. $X_k = [X_1 X_2 ... X_{N-1}]^T \in \mathbb{C}$ is converted to the time domain from the frequency domain by using Inverse discrete Fourier transform (IDFT) , which is given as

$$x_n = \frac{1}{N} \sum_{k=0}^{N-1} X_k \exp\left(j2\pi k \frac{n}{N}\right), \tag{2.16}$$

where $n = 1, 2, \ldots, N-1$ and N is the total number of subcarriers. After converting the signal from frequency to time domain, cyclic prefix is included for every subcarrier as a guard interval and pulse shaping techniques are applied to reduce Inter symbol interference (ISI) before the signal transmission. At the receiver, the cyclic prefix and pulse shaping is removed before converting the time domain version of OFDMA signal into frequency domain using Discrete Fourier transform (DFT) as in Fig. 2.4. Even though OFDM is able to transmit data at high data rate and reduce the ISI by using orthogonality property, it still suffers from ISI especially due to multipath propagation. However, ISI can be avoided with proper cyclic prefix and pulse shaping. One of the main problem of OFDM signal is that it can have large envelope fluctuations in its waveform and it is incremental in case of OFDMA due to the summation of N modulated subcarriers as in (2.14). Therefore, IDFT output of a multicarrier signal with a large envelope results in very high peak power and subsequently leads to problems in operations such as amplification and quantization at the transmitter. The most common way to quantify these peak power outputs of multicarrier signals is to calculate peak to average power. The ratio of peak power to the average power of a signal is commonly called the Peak to average power ratio (PAPR). The mathematical expression for PAPR is given as

$$\text{PAPR} = \frac{\max(|x_n|^2)}{\mathbb{E}[|x_n|^2]} = \frac{\max(|x_n|^2)}{2\sigma_x^2}, \tag{2.17}$$

where $\max(|x_n|^2)$ gives the instantaneous peak power of the signal and $2\sigma_x^2$ is the expected average power of the signal. It should be noted that this PAPR will increase with the increase in the number of subcarriers of the signal transmit power and also higher order modulation can exacerbate PAPR.

2.3.2 Single Carrier Frequency division multiple access

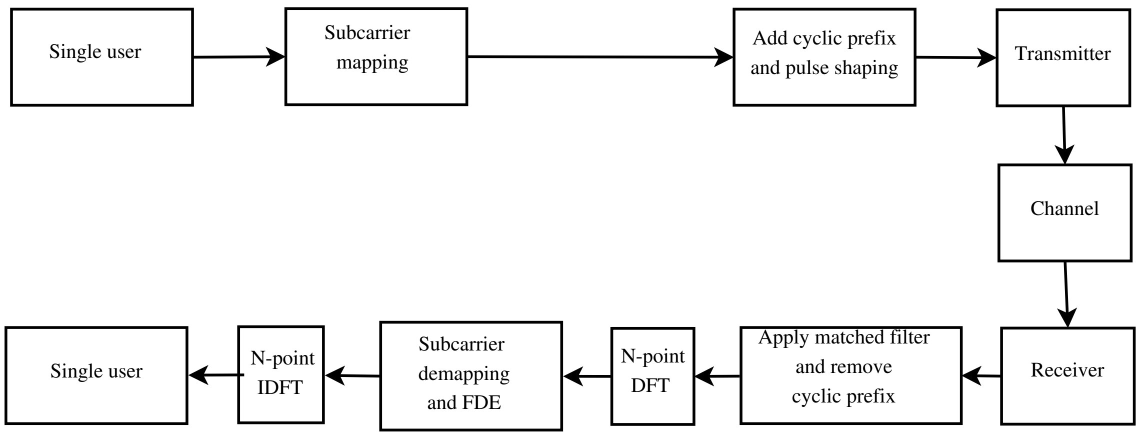

Figure 2.5: Block diagram of transmitter and receiver section of SC-FDE.

Single carrier transmission scheme combined with FDE i.e. SC-FDE can be complementary transmission scheme multicarrier modulations such as OFDM, mainly due to presence nonlinear equalizer structures in the frequency domain transmission chain [22]. Another advantage is the lower level of PAPR in SC-FDE as compared to OFDM, despite having similar performance and complexity levels of OFDM [23]. When comparing SC-FDE (see Fig. 2.5) and OFDM (see Fig. 2.4), SC-FDE structure is similar to that of OFDM but the main difference is the presence of IDFT block at the receiver side in the SC-FDE instead of transmitter side. Due to this main difference, OFDM has several parallel transmissions carrying a single data stream and in case of SC-FDE, the data streams are transmitted serially in a single carrier. Even though SC-FDE (DFT–S–OFDM) is similar to OFDM, the PAPR in SC-FDE is reduced as the symbol energy in a single subcarrier spreads over all the subcarriers before the IDFT function. A single carrier modulation is a modulation in which the energy of every symbol spreads throughout the all the transmission band. The signal transmission for n^{th} block in time domain of SC-FDE modulation is written as

$$x(t_i) = \sum_{n=-Ns}^{N-1} x_n r(t_i - nT_s), \tag{2.18}$$

where x_n is the complex data symbol with $n = 1, 2, \ldots, N-1$. $r(.)$ and Ns are the pulse shaping filter function and the cyclic prefix, respectively. The usage of block wise transmission technique with a cyclic Prefix before each block reduces ISI from the previous block. To avoid inter block interference between the blocks, cyclic prefix length should be greater than channel impulse response. The block-wise transmission in SC-FDE at the receiver can be implemented by using DFT, this reduces the complexity of the receiver while having low PAPR due to low envelope fluctuations. Therefore, when combining the time domain processing technique with the usage of a cyclic prefix, SC-DFE has the same performance and low complexity level of OFDM [22]. However, the receiver section of SC-FDE is more complex than OFDM and thus, requires proper equalization techniques.

2.3.2.1 Iterative block decision feedback equalization decoder

There are many FDE schemes available for single carrier modulation to reduce the impact of channel impulse response on the transmitted signal. Although single carrier modulation can employ FDE schemes such as Minimum mean squared error (MMSE), usually the residual interference could lead to performance degradation. In general, nonlinear time domain equalizers are known to outperform linear equalizers and therefore one of the promising nonlinear FDE technique which is iterative block based FDE i.e. IB-DFE is introduced [24]. Due to its low complexity, IB-DFE is proposed for FDE in diversity scenarios [25], for MIMO systems in [26], and for multiple user case in [27]. The IB-DFE is further improved by adopting frequency domain feed forward and frequency domain feedback loop for SC-FDE in [28].

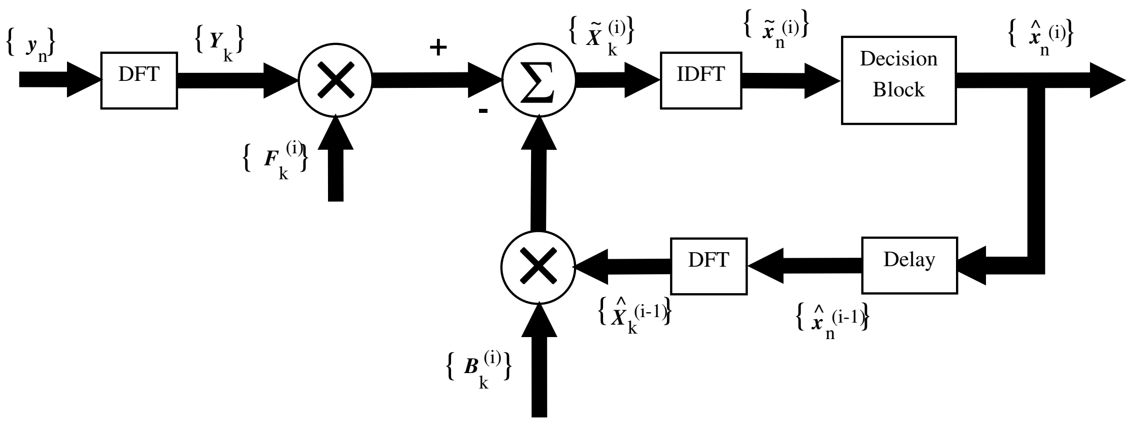

Figure 2.6: Basic IB-DFE block diagram for single user SC-FDE.

The IB-DFE receiver block diagram for single user SC-FDE is given in Fig. 2.6, where y_n and Y_k, respectively are the received signal in time and frequency domain and $\hat{x}_n^{(i)}$ is the estimated information (modulated symbols as in the transmitter side) in time domain for the given IB-DFE iteration (i), where $i = 0, 1, ..., N$ and i is the number of iterations followed in an IB-DFE receiver. We assume that the communication channel is Rayleigh frequency selective fading channel and it is denoted by the coefficient H_k. The IB-DFE based estimate for $\tilde{X}_k^{(j)}$ is given as

$$\tilde{X}_k^{(i)} = X_k F_k^{(i)} - \hat{X}_k^{(i-1)} B_k^{(i)}, \tag{2.19}$$

where $\hat{X}_k^{(i-1)}$ is the previous iteration value of $\tilde{X}_k^{(i)}$, $F_k^{(i)}$ and $B_k^{(i)}$ are the iteration of feed forward coefficient and feedback coefficient, respectively. $F_k^{(i)}$ is given as

$$F_k^{(i)} = \frac{H_k^*}{\left(\frac{\sigma_N^2}{\sigma_X^2}\right) + |H_k|^2\left(1 - (\rho^{(i-1)})^2\right)}, \tag{2.20}$$

where $\rho^{(i-1)} = \frac{\mathbb{E}[\hat{x}_n^{(i)} x_n^{(i*)}]}{\mathbb{E}[|x_n^{(i)}|^2]}$ is the correlation factor of x_n. σ_N^2 and σ_X^2 are the variance of noise and X_k, respectively. The feedback coefficient is written as

$$B_k^{(i)} = \rho^{(i-1)}(F_k^{(i)} H_k - 1). \tag{2.21}$$

In general, the accuracy of $\hat{x}_n^{(i)}$ increases with each iteration up to its saturation point which is closer to Matched filter bound (MFB) and this makes IB-DFE technique as one of the most preferred FDE technique for SC-FDE.

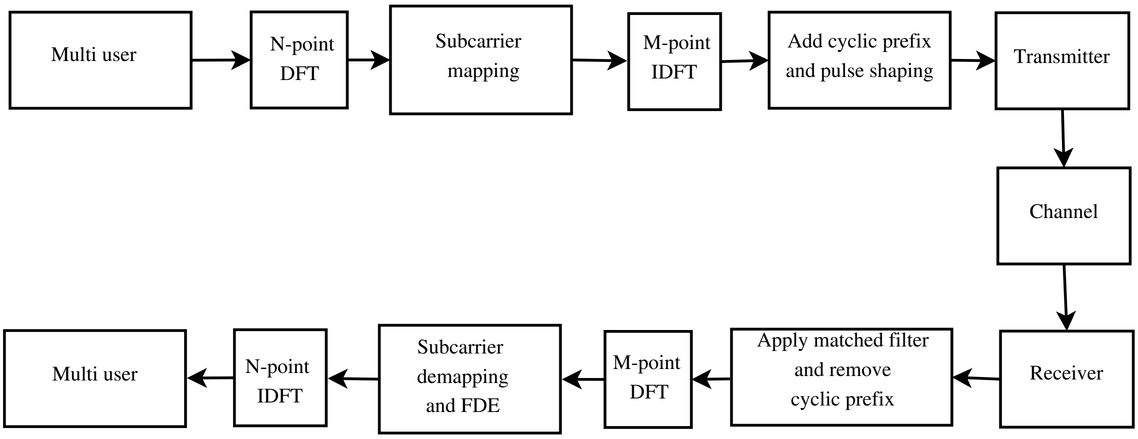

Figure 2.7: Block diagram of transmitter and receiver section of SC-FDMA.

Another important technique in single carrier modulation is SC-FDMA or DFT–S–OFDM and the main difference between SC-FDE and SC-FDMA is the presence of DFT and IDFT block at the transmitter side of SC-FDMA. Similar to OFDMA, SC-FDMA transmits the signal as blocks of symbols sequentially in multiple linear subcarriers within a single subcarrier at the same instant. However, SC-FDMA has an additional DFT block at the transmitter side before the subcarrier mapping of the symbols as in Fig. 2.7. The time domain data symbols, $x_n, n = 1, 2, \ldots, N-1$ in N subcarriers are converted to frequency domain symbols, $X_k, k = 1, 2, \ldots, N-1$ by using N-point DFT as in Fig. 2.8. Then, X_k which is N subcarriers are mapped with M subcarriers level $X_l, l = 1, 2, \ldots, M-1$ by using distributed subcarrier mapping. There are two main subcarrier mapping methods, they are distributed or interleaved subcarrier mapping method and localised subcarrier mapping method [29]. SC-FDMA has a gain of 4 to 7 dB in PAPR when using distributed subcarrier mapping as compared to localised subcarrier mapping, however adopting localised subcarrier mapping approach gives better throughput than adopting distributed subcarrier mapping [29].

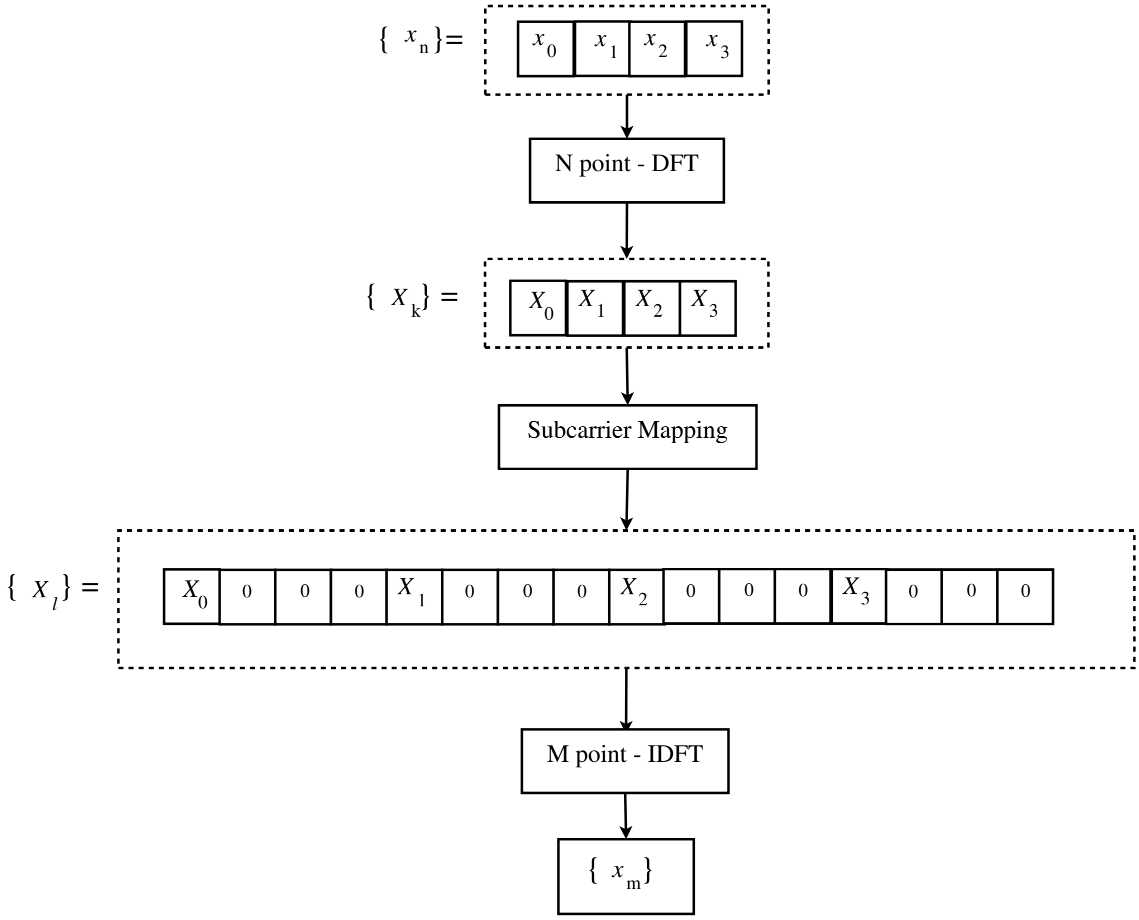

Figure 2.8: Generation of SC-FDMA symbols in transmitter block.

The main difference between OFDMA and SC-FDMA in terms of signal transmission block is an additional DFT block at the SC-FDMA transmitter. Also, the receiver side, SC-FDMA has an additional IDFT block after the subcarrier demapping function. In general, both OFDMA and SC-FDMA employ equalization techniques to reduce distortion of time dispersive signal that is transmitted over fading channels. Even if both the techniques can employ low complexity frequency domain equalization schemes like MMSE, SC-FDMA can additionally employ IB-DFE along with Successive interference cancellation (SIC) to increase the gain close to the level of MBF [30].

2.4 Multiple Input Multiple Output System

Multiple input and multiple output (MIMO) system is one of major technologies in the wireless communication network, which lead to drastic increase in capacity of wireless channel links. The main motivation of the MIMO concept is to increase throughput of the communication network. In wireless communication networks, throughput is a measurement of successfully transferring bits per second to the receiver. Throughput (bits/s) is a product of bandwidth (Hz) and spectral efficiency (bits/s/Hz), so throughput can be increased by bandwidth or/and spectral efficiency. A fixed bandwidth is not easy to change and bandwidth in a way can decrease SNR, in a wider bandwidth, the receiver gets additional noise associated with the frequency range of wider bandwidth. So the focus on increasing throughput by using spectral efficiency is explored with MIMO technology [31]. MIMO antenna increase the spectral efficiency by utilizing the antenna diversity at both transmitter and receiver, where signal streams are multiplexed into several separate signal streams depending on number of antennas used at transmitter and receiver [32], [33]. MIMO improves the reliability of the communicating channel by offering redundant channel links, which can also be used for diversity gain and capacity gain. So, MIMO can be adopted for different scenarios, even for the channel with a strong fading environment [32]. The introduction of MIMO has led researchers to explore space-division multiple access, which is used to reuse intracell bandwidth by adopting spatial multiplexing techniques [34, 35]. Therefore, when the hardware requirements are increased due to the MIMO system, the power and hardware requirements are optimised by evolving MIMO techniques that exploits space diversity and other radio resources [36, 37].

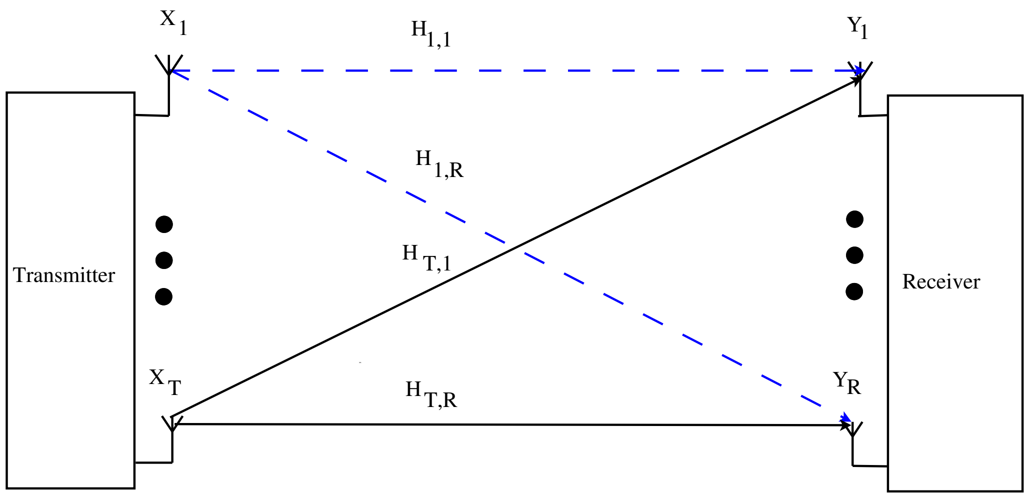

Figure 2.9: System model of MIMO.

In this section, we present a simple MIMO system model in Fig. 2.9, where the total number of transmitting antennas and receiving antennas is T and R, respectively. The $X_t; t = 1, 2, ..., T$ is transmitted from the transmitter to the receiver over $H_{r,t}; t = 1, 2, ..., T; r = 1, 2, ..., R$ channels, here the signal will have diversity order depending on the number of transmitting and receiver antennas. Then the received signal at receiving antenna r is given as

$$Y_r = \sum_{t=1}^{T} PX_t H_{r,t} + N_r, \tag{2.22}$$

where N_r and P are the AWGN and average power constraint for all the received signal, respectively and the average noise power of N_r is denoted as N_0. Therefore, the average

SNR for all the received signal is given as $\gamma = \frac{P}{N_0}$. The received signal in the matrix format is given as

$$\begin{bmatrix} Y_1 \\ \vdots \\ Y_R \end{bmatrix} = \begin{bmatrix} X_1 \\ \vdots \\ X_T \end{bmatrix} \begin{bmatrix} H_{1,1} & \dots & H_{1,T} \\ \vdots & \ddots & \vdots \\ H_{R,1} & \dots & H_{R,T} \end{bmatrix} + \begin{bmatrix} N_1 \\ \vdots \\ N_R \end{bmatrix} \tag{2.23}$$

Here, a MIMO channel capacity is derived by using singular value decomposition (SVD) as in [38]. Based on SVD, the channel matrix is given as $h = usv^H$, where u and v are left and right singular vectors of h, respectively. u and v can be used as combining matrix and precoding matrix, respectively. From this, we can write $x = v\tilde{x}$ and $\tilde{x} = u^H y$, where x is a precoded signal of X or IDFT of X. So based on SVD, the MIMO can be equivalent to parallel single input and single output systems with different SNRs values and equal SNR if all links have the same transmit power and noise power. Since, we consider γ is equal for all channel links, the capacity for a random MIMO channel with the assumption that $T = R$ is given as

$$C = T \log_2(1 + \gamma). \tag{2.24}$$

2.5 SWIPT for Channel estimation

The channel estimation and signal detection techniques are fundamental part of signal processing as well as the most critical to wireless communication. The Channel state information (CSI) obtained by the communication networks by using channel estimation techniques is imperative for signal detection at the receiver side. The CSI is crucial for achieving reliable communication with high data rates in multi antenna systems. So there are several channel estimation techniques in practice for estimating the CSI of the communicating channel, however it is impossible to have full knowledge of CSI and the main contributors for the imperfect CSI are channel estimation error, delay and frequency offset. Therefore, it is imperative to reduce channel estimation and frequency offset ratio errors as much as possible. The effectiveness of channel estimation technique depends mainly on the fading condition of the channel and the channel estimation errors are comparatively higher in fast fading channels than that of slow fading channels. The imperfect CSI condition leads to an increase in signal detection errors and this situation exacerbates when SWIPT or WPT techniques are adopted under imperfect CSI conditions [39]. For example, by studying the impact of imperfect CSI on TS-SWIPT, we can attribute that the increase in energy harvesting time in TS-SWIPT leads to the increase in signal detection errors and outage probability [39], since the channel estimation errors indirectly decreases SNR of the received signal.

The efficiency of energy harvesting in WPT and SWIPT can be improved with CSI by adopting channel adaptive waveform for converting RF signal energy to Direct current (DC) [40]. The general simplistic approach involves non-adaptive waveforms without considering CSI, however the efficiency of RF energy to DC is lower and unreliable, which then depends on the fading scenario of the communicating channel. Therefore without considering multipath fading, the expected power out cannot be achieved and hence, the waveform of the transmitting EH signal needs to be optimized in accordance with the CSI. There are several research works that are focused on designing channel-adaptive wireless power waveform to maximize RF to DC efficiency and in this approach transmitter acquires CSI and sends EH signal waveform accordingly [41, 42].

In practice, the channel estimates are obtained by using pilot symbols, which are either in time or frequency domain [43]. Most commonly, frequency domain is used for OFDM modulations while both time and frequency domain is used for SC modulations. In block transmission techniques, the channel impulse response may be very long and the record over-heads for channel estimation is possibly very high. As a solution, the pilot symbols are superimposed with the information symbols,instead of multiplexing the pilot symbols with the information symbols. This increases the density of pilots with respect to information symbols without comprising spectral efficiency. This helps in improving the amount of EH. The disadvantages of using a superimposed pilot signal, is the interference of pilot signal with the information signal with increase in transmit power of pilot signal. Then, the interference of the pilot signal with the information signal can be reduced by averaging the channel estimate of the respective frequency. The proposed technique helps in estimating CFO as shown in [44] by using the highly energized identical pilot signal sequence on each block. Thereby with the help of SWIPT, pilot signals will be more robust for signal interference and noise. Therefore, in the upcoming chapters our research work is focused on adopting SWIPT techniques for supporting channel estimation and signal detection techniques.

2.6 SWIPT for Physical layer security

Apart from harvesting energy by using SWIPT techniques, SWIPT could be adopted for PLS purposes [46]. One of the most important technique in improving PLS of a wiretap channel, is using AN in the communication channel to degrade the Signal-to-interference plus noise ratio (SINR) of eavesdroppers; and thereby, improving the security of legitimate users [3]. The high energy signal that is used for harvesting energy in SWIPT can also be adopted for creating AN to improve PLS as in [47]. The secrecy rate of legitimate users in a wiretap channel can be improved with the SINR degradation of eavesdroppers as in [48, 49]. Furthermore, the secrecy rate for the MIMO system model is established in [50]. A simple wiretap channel is presented in Fig. 2.10, where two jamming signals are used to jam the eavesdropper. When transmitter broadcasts the signal, the eavesdroppers can receive the signal as like the receiver and the main idea using jammer are in introducing AN to the wireless network. To avoid the impact of AN to the legitimate receiver, AN is introduced in the null space of the legitimate receiver's channel matrix. The channel link from the jammers J_1 and J_2 to the receiver R are denoted as H_{J1R} and H_{J2R}, respectively. The following equations presents simple precoded jamming symbols $X_{J_1}^{(k)}$ and $X_{J_2}^{(k)}$ from J_1 and J_2, respectively as

$$\begin{aligned} X_{J_1}^{(k)} &= A_{J_1}^{(k)} H_{J2R}^{(k)}, \\ X_{J_2}^{(k)} &= A_{J_2}^{(k)} H_{J1R}^{(k)}, \end{aligned} \tag{2.25}$$

where $k = 1, 2, ...N$, $A_{J_1}^{(k)}$ and $A_{J_2}^{(k)}$ are the k^{th} entry of the precoding vectors $\mathbf{A}_{J_1}$ and $\mathbf{A}_{J_2}$, respectively. The precoding vectors are chosen such that, under any SINR condition $H_{J1R}^{(k)} X_{J_1}^{(k)} + H_{J2R}^{(k)} X_{J_2}^{(k)} = 0$, however there could be slight precoding error due channel estimation error or a change in channel impulse response and this error can be consider as noise N_p at the receiver side. Whereas eavesdropper will receive the jamming signal as an AN. Therefore SNR of R and Eavesdropper ξ are respectively given as

$$\gamma_R = \frac{P}{N_0 + N_p}; \qquad \gamma_\xi = \frac{P}{N_0 + N_{AN}}, \tag{2.26}$$

where N_0 and N_{AN} are the noise power of AWGN and AN, respectively, and P is the transmit power of a data signal. Then, secrecy capacity rate can be written as

$$C_R = \log\left(\frac{1 + |H_{TR}|^2 \gamma_R}{1 + |H_{T\xi}|^2 \gamma_\xi}\right), \tag{2.27}$$

where H_{TR} is the channel link between the transmitter and receiver, and $H_{T\xi}$ is the channel link between the transmitter and eavesdropper. From this, we could understand that the secrecy rate depends on the channel gains as well as N_0, N_{AN} and N_p. Thereby,

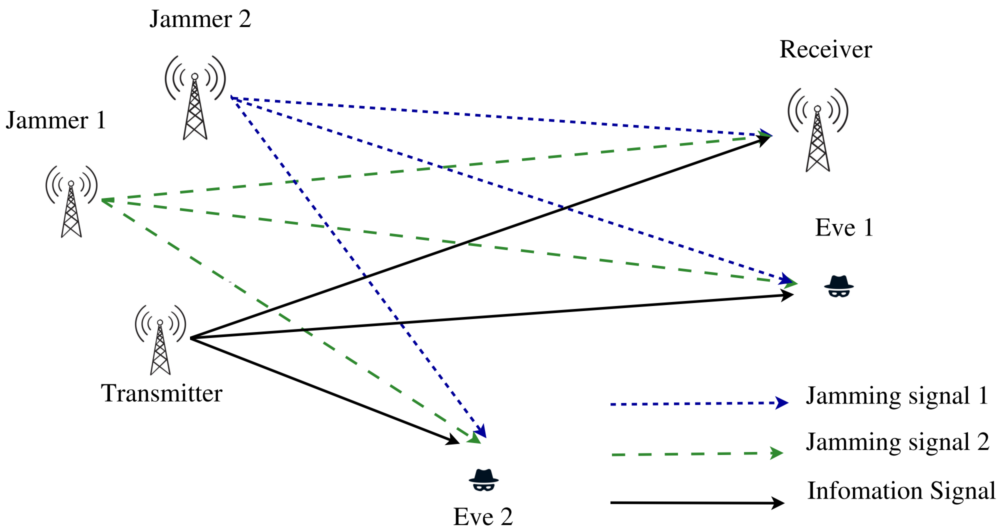

Figure 2.10: A wiretap channel.

AN degrades SINR of eavesdroppers without compromising the quality of the legitimate users' signal [51]. However, the successful negation of AN is dependent on the CSI of the receiver at the legitimate transmitter and can be effectively used against much robust eavesdroppers as in [52]. This is considered as a challenge in imperfect CSI condition [53, 54]. Another challenge in using AN against eavesdroppers lies in the fact that a jamming attack depends on the channel correlation between the eavesdroppers and legitimate receiver; if the channel correlation is very high, then AN can be partially cancelled out by eavesdropper [55, 56].

Therefore, the high channel correlation between the eavesdroppers and legitimate receiver is considered as a major limitation of jammers in a wiretap channel. It is mitigated by increasing the jamming signal power that amplifies the error due to the difference in CSI between both channels. The increment in jamming signal power can degrade the eavesdropper's SNR, but this can also increase the negative impact of the jammer's precoding error at legitimate receiver. The effect of the jammer's precoding error at a legitimate receiver can be reduced by using the expected jammer's precoding error as additional noise power feedback in the IB-DFE decoder [57]. Even though the increase in jamming signal power can increase SNR degradation at the eavesdropper, this is not energy efficient and can degrade the performance of the legitimate receiver, if there is any channel estimation error or precoding error in the legitimate network. In [57], the passive eavesdropper does not estimate jamming signal and in this research, the idea of cooperative eavesdropper is explored to estimate jamming signal. Therefore, it is necessary to optimize the jamming signal power and explore counter measures for a cooperative eavesdropper scenario. In chapter 6, our research is focused on optimizing the transmitting power of EH components in SWIPT to improve energy efficiency and improve secrecy rate of information components.

3

Modulation-based simultaneous wireless information and power transfer

In this chapter, we introduce a new SWIPT scheme called M-SWIPT[1] and it does not explicitly use power or time resources instead it allocates Constellation points (CPs) of the modulated signal for energy harvesting EH. In [58], researchers investigated the performance of SWIPT adopting an M-ary modulation scheme, which represents a major leap forward as it does not require a dedicated beam as in the case of wireless power transfer. However, this comes at the expense of some loss in the system throughput since part of the transmitted signal is used for power transfer. Furthermore, EH is beneficial only when the received signal power is greater than a certain sensitivity level. Henceforth, it is necessary to conceive an alternate SWIPT concept.

M-SWIPT technique uses specific CPs for EH and then the remaining ones for Information transmission (IT) . This suggests that the CPs intended for IT do not suffer direct power loss due to EH, which is different from how CPs are used in traditional power splitting and time switching architectures [2], [4]. However in M-SWIPT, the excess amount of energy will be spent in transmitting symbols for EH. Alternatively, symbols carrying information and energy can be transmitted in two separate signal streams using two different time slots, but this consumes excess time resource, decreasing the spectral efficiency [2]. Due to the nature of CPs usage in M-SWIPT, it gives us an opportunity to shape the CPs to improve the performance of M-SWIPT. The idea of shaping the CPs is introduced in [59] and their performance is studied in [60] and [61]. We can improve the spectral efficiency of M-SWIPT by utilizing HCS [62] and in M-SWIPT, HCS of M-ary modulation is adopted. HCS is a hybrid geometric and probabilistic shaping method that modifies the nature of the signal to a non-uniform and non-equidistant constellation point distribution. HCS is preferred over geometric shaping and Probabilistic amplitude shaping (PAS) as it maintains the total amount of energy of each Constellation point (CP)

[1] In the figures and tables M-SWIPT is shortly denoted as (MS).

like regular M-QAM. This helps in allocating fixed amounts of energies for IT and EH, regardless of the degree of constellation shaping.

In contrast with existing SWIPT techniques, we show that M-SWIPT has better SER and maximum AIR for low SNR operating regions. However, at high SNR, the AIR of M-SWIPT does not reach its maximum rate due to the fact that some CPs are used for EH. AIR of M-SWIPT can be further improved for certain SNR regions by using HCS. Thus, HCS is effective for our proposed M-SWIPT scheme to improve AIR as compared to using a regular M-QAM scheme for EH and IT.

3.1 System model

We assume a point-to-point communication system comprising a transmitter Tx and a receiver R. The input signal $\mathbf{x}$ is transmitted by using the transmit power P over Rayleigh fading channel and the channel co-efficient is given as h, where $h \sim CN(0,\sigma^2)$ and the channel power gain is $|h|^2$, which has an exponential distribution. The channel noise $\mathbf{n}$ is AWGN with zero mean and variance σ_{TR}^2, $\mathbf{n} \sim N(0,\sigma_{TR}^2) = N(0,N_0/2)$. $\mathbf{x}$ has N symbols and the nth individual symbols of $\mathbf{x}$ are denoted by x_n, $n = 1,...,N$ [2]. The CPs of $\mathbf{x}$ are based on a square M-QAM modulation, where $M = 2^b$, and b is the number of bits per symbol. CPs are denoted as $A^{[s]}$, where s is the index of CP, with $s = 1,..,M$.

3.1.1 Modulation-based SWIPT Technique

In the M-SWIPT, all the highest energy CPs (with same magnitude) are selected for EH and are denoted by the set $A_e^{[s]}$. The rest of the CPs are used for IT, and define the set $A_d^{[s]}$. Here, $\{A_e^{[s]}, A_d^{[s]}\} \in A^{[s]}$ and M-SWIPT are illustrated in Fig. 3.1. If $x_n \in A_e^{[s]}$, then it is denoted as $x_{n,e}$, else it is denoted as $x_{n,d}$. Here, $x_{n,d}$ and $x_{n,e}$ are orderly positioned in a pattern known to T and R, and based on this pattern and amplitude of the symbols, the receiver separates the symbols for IT and EH.

The basis of selecting CPs for EH in M-QAM is dependent on two factors. Firstly, the amount of energy to be harvested. Since each constellation point has a fixed amount of energy level, the fraction of CPs for EH can be used to select the desired energy ratio between EH and IT. Secondly, while choosing the CPs for EH, $A_e^{[s]}$, if high amplitude CPs are chosen for EH and other CPs for IT, then it will be comparatively easy for the receiver to distinguish specific symbols for IT and this simplifies the receiver synchronization between EH and IT. Moreover, the EH signal should be designed to avoid undesirable spectral lines, which is achieved with a pseudo-random selection within $A_e^{[s]}$ and a set $A_e^{[s]}$ with zero mean (that is the case of the set of higher energy CPs in a QAM constellation).

$$\mathbf{y} = \sqrt{\frac{P}{E_M}} h\mathbf{x} + \mathbf{n}, \tag{3.1}$$

[2] In this chapter, irrespective index n of the symbol, only the set of symbols used for IT is considered for calculating SER and AIR performance.

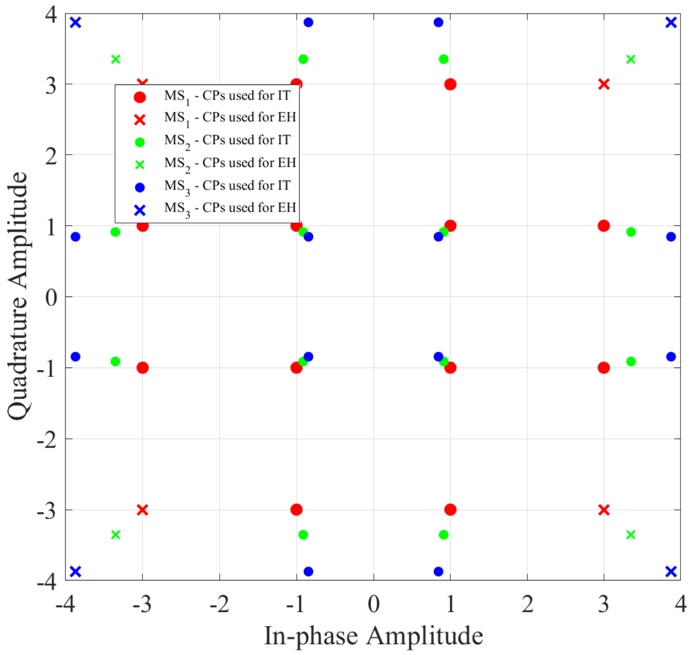

Figure 3.1: The CPs of MS_1, MS_2 and MS_3 are illustrated without considering their respective per symbol transmit power. The models are described in Sec. 3.2 and its alphabets are mentioned in Tab. 3.1. The HCS of MS_3 model is illustrated in Fig. 3.2.

where E_M is the average amount of energy of the symbol and P is the transmit power. The amount of energy harvested from the received signal at R is is denoted as Ł_{MS}, which is expressed as

$$\text{Ł}_{MS} = \frac{\eta_{EH} P |h|^2 \zeta}{{d_{TR}}^{\varkappa}}, \tag{3.2}$$

where η_{EH} is the RF energy harvesting efficiency, the distance between T and R is denoted as d_{TR} and $\varkappa$ is the path loss factor. $\zeta = E_e/E_S$, E_e and E_S are the total amount of energy present in $\mathbf{x}_e$ and $\mathbf{x}$, respectively and T_s is the time taken for transmitting $\mathbf{x}$. E_e and E_S are given as $E_e = \mathbb{E}[|\mathbf{x}_e|^2]$ and $E_S = \mathbb{E}[|\mathbf{x}|^2]$, respectively[3]. The transmit SNR of $\mathbf{x}$ is denoted as γ and $\gamma = \frac{E_S}{N_0}$.

3.1.2 Hybrid constellation shaping in M-QAM

HCS shapes the CPs by changing the amplitude and probability of occurrence of the symbols of each CP and thereby changes the percentage of symbols present in each CP and the amplitude of respective symbols. The HCS model is illustrated in Fig. 3.2[4] and in Fig. 3.1. An important feature of HCS is that irrespective of the degree of shaping, the total amount of energy in each CP is constant. $A^{[s]}$ is represented in a complex form by the combination of the individual alphabets, where the alphabets are denoted as a,

[3]The expected value operator is denoted as $\mathbb{E}[w]$, where w is a variable.
[4]For our convenience, only the B_3 model is illustrated.

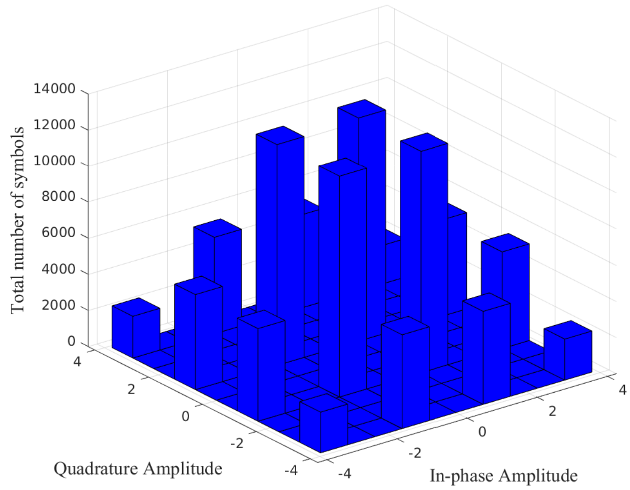

Figure 3.2: The symbols distributed across the CPs of 16-QAM signal based on HCS model B_3 are described in Sec. 3.2 and its alphabets are mentioned in Tab. 3.1.

where a in real and imaginary axis are denoted as a and ja, respectively. The value of a is $(2m-1)$, where if $M \geq 16$ then $m = 1, ..., \frac{\sqrt{M}}{2}$, or else if $M = 4$, then $m = 1$. The value of $A^{[s]}$ due to HCS is expressed as

$$A^{[s]} = \pm \frac{\rho_u(a)}{\rho(a)} a \pm \frac{\rho_u(ja)}{\rho(ja)} ja, \tag{3.3}$$

where the non-uniform probability and uniform probability occurrences of a in CPs are denoted as $\rho(a)$ and $\rho_u(a)$, respectively. Similarly, the non-uniform probability and uniform probability occurrence of ja in CPs are denoted as $\rho(ja)$ and $\rho_u(ja)$, respectively. To validate perfect HCS of M-QAM signal, the signal stream x_n belonging to $A^{[s]}$ should satisfy the following condition.

$$\mathbb{E}[\pm \frac{\rho_u(a)}{\rho(a)} a \pm \frac{\rho_u(ja)}{\rho(ja)} ja] = \mathbb{E}[\pm \rho_u(a) ja \pm \rho_u(ja) ja], \tag{3.4}$$

where (3.4) is a condition in which the expected value of individual CP with HCS as in (3.3) should always be equal to the expected value of its respective CP with uniform symbol distribution.

3.1.3 Comparison of M-SWIPT and PS-SWIPT

The M-SWIPT is compared with the traditional PS-SWIPT[5]. Both M-SWIPT and PS-SWIPT schemes divide the transmit power for EH and Information decoding (ID) but the method of dividing the power is different for both the schemes. In PS-SWIPT, energy is harvested from **y** by using a power splitting circuit and this circuit divides the power of the signal for EH and information decoding [1], [2]. Thus, in PS-SWIPT all the symbols are

[5]In the figures and tables PS-SWIPT is shortly denoted as (PS).

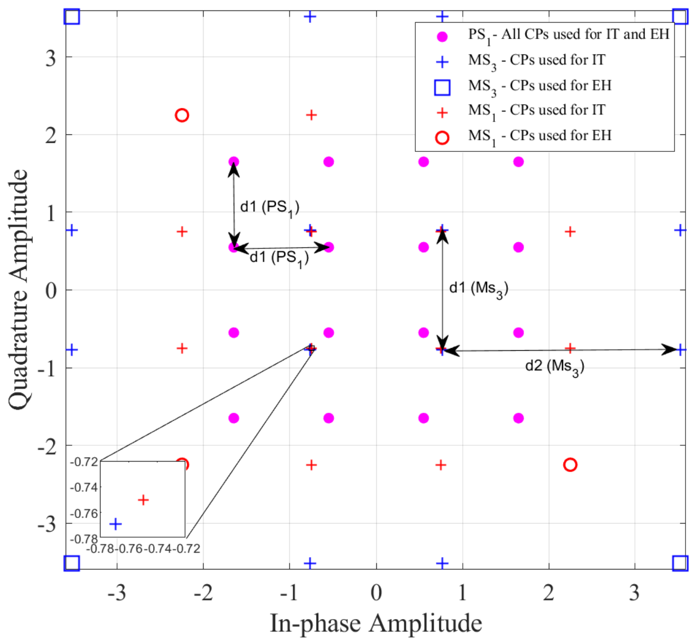

Figure 3.3: The minimum distance between CPs of MS_1, MS_3 and PS_1 are illustrated as given in Tab. 3.2. Note that the position of CPs in the M-SWIPT scheme varies when compared to their respective position illustrated in Fig. 3.1 because of the consideration of their respective P_m.

used for EH, whereas in M-SWIPT, EH only comes from the specific CPs of $\mathbf{y}$. In M-SWIPT, the total number of symbols used for IT and EH are denoted as N_i and N_e, respectively. N_i should be equal in both M-SWIPT and PS-SWIPT, and then $K = N_i/(100-\rho(\mathbf{x}_e))\%$, where $\rho_u(\mathbf{x}_e)$ is the probability of x_e present in $\mathbf{x}$ and $N_e = N - N_i$. Irrespective of additional symbols present in M-SWIPT, N_i should be equal in both M-SWIPT and PS-SWIPT and also P should be equal in both PS-SWIPT and M-SWIPT to compare both the EH schemes. The transmit power used in M-SWIPT for each symbol is given as

$$P_m = P(N_i/(N_e + N_i)), \tag{3.5}$$

where P is the transmit power of each symbol present in PS-SWIPT. The SER performance of M-SWIPT and PS-SWIPT models are dependant on SNR condition and minimum distance between $\mathbf{x}_d$ and its neighbouring symbol, which is denoted as d_{TR}. $d_{x_{n,d}}$ of both the schemes are dependent on the position of CPs and the power allocated for the symbols to perform IT. In uniform CPs distribution, the relationship between M-SWIPT and PS-SWIPT in terms of $d_{x_{n,d}}$ and transmit power per symbol is given as

$$P_m d_{x_{n,d}} = \zeta_P P d_{x_{n,d}}, \tag{3.6}$$

where ζ_P is the fraction of P allocated for IT and the value of $d_{x_{n,d}}$ varies depending on HCS models. The minimum distance of a 16-QAM signal using M-SWIPT and PS-SWIPT models with equal number for symbols for IT and also with equal value of P are illustrated in Fig. 3.3. The figure shows that $d_{x_{n,d}}$ in M-SWIPT is greater than that of PS-SWIPT. Also by using HCS, it is possible to increase $d_{x_{n,d}}$ of symbols in M-SWIPT. Fig. 3.3 illustrates $d_{x_{n,d}}$ of MS_1 and MS_3 and the value is calculated in Tab. 3.1. As compared to MS_1, in MS_3, the HCS reduces the amplitude of symbols in low amplitude CPs and increases the amplitude of symbols in high amplitude CPs and this decreases N_e of MS_3 over MS_1, thus P_m increases with the decrease N_e.

The basis of selecting the degree of HCS is dependant on the operating SNR region of the system and Shannon entropy of the signal, which is denoted as $H(\mathbf{x})$. For different operating SNR region, the system can be adapted by adjusting P_m value with the change in the degree of HCS. $H(\mathbf{x})$ is maximum under uniform HCS. For a regular M-QAM signal with uniform probability occurrence of CPs, $H(\mathbf{x}) = \sum_{s=1}^{M} \rho_u(A_d^{[s]}) \log\left(1/\rho_u(A_d^{[s]})\right)$, where $\rho_u(A_d^{[s]})$ is the uniform probability of symbols belonging to $A_d^{[s]}$ is present in $\mathbf{x}$. Similarly, for M-QAM signal with HCS, we should considered only the CPs used for IT. Also, the percentage of excess symbols used in $A_d^{[s]}$ should be considered in calculating Shannon entropy of M-SWIPT and it is given as

$$H(\mathbf{x}_d) = \sum_{s=1}^{M} \left(\rho(A_d^{[s]}) \frac{N_e + N_i}{N_i}\right) \log\left(\frac{\{\rho(A_d^{[s]})\}^{-1}}{\frac{N_e+N_i}{N_i}}\right), \tag{3.7}$$

where $(N_e + N_i)/N_i$ is the percentage of increase in the symbols belonging to $A_d^{[s]}$ and $\rho(A_d^{[s]})$ is the non-uniform probability of symbols belonging to $A_d^{[s]}$ is present in $\mathbf{x}$. Even though N_i is equal for both the regular signal and M-SWIPT signal, $H(\mathbf{x})$ decreases with the decrease in randomness. AIR of M-SWIPT signal is denoted as AIR_M. The maximum AIR_M of the signal is determined by the value of $H(\mathbf{x}_d)$ and it is also necessary to select HCS models based on its $H(\mathbf{x}_d)$ value and operating SNR region where the maximum AIR_M can be achieved.

In general, PS-SWIPT should have better AIR performance than that of M-SWIPT due to the usage of all the CPs of regular M-QAM signal and uniform CPs distribution. In PS-SWIPT, due to the fact that the energy is harvested from all the symbols in the signal, the SNR of the symbols in low amplitude CPs suffers energy loss as opposed to the case of low amplitude symbols in M-SWIPT and it is illustrated in Fig. 3.3. Thus, at low SNR, the HCS models in combination with M-SWIPT having low $H(\mathbf{x})$ can possibly perform better than the models with high $H(\mathbf{x})$ value.

3.1.4 Theoretical symbol error and achievable rate of M-QAM with M-SWIPT

In this section, average SER is derived for the proposed system using the M-QAM signal with HCS. The symbols of M-QAM are located in three regions of CPs. There are 4 symbols in the corner, $4(\sqrt{M} - 2)$ symbols on the edge of CPs and $(\sqrt{M} - 2)^2$ symbols in the interior. The approximated SER of individual symbols located in corner, edges and interior is 2 SER_{Cr}, 3 SER_{Ed} and 4 SER_{In}, respectively. The SER of an individual symbol is denoted as SER_{x_d}. Depending on the location of symbols in the constellation map, $\text{SER}_{x_d} \subset \{\text{SER}_{Cr}, \text{SER}_{Ed}, \text{SER}_{In}\}$. Thus, SER_{x_d} is given as

$$\begin{aligned} \text{SER}_{x_d} &= \int_0^\infty Q(2d_{x_{n,d}} a_h \gamma) 2a_h \exp\left(-(a_h{}^2)\right) \mathrm{d}a_h \\ &= \frac{1}{2}\left(1 - \sqrt{\frac{d_{x_{n,d}}\gamma}{1 + d_{x_{n,d}}\gamma}}\right), \end{aligned} \tag{3.8}$$

where a_h is the amplitude of the channel h and $\mathrm{d}a_h$ is the differential of a_h. The neighbouring CPs are used for either IT or EH. In the case of 4-QAM, all the symbols are considered as corner symbols. Thus, depending on the energy requirement, the symbols in 4-QAM are used for either EH or IT.

The average SER of M-SWIPT signal is derived based on the general SER of M-QAM signal derivation in [63] but it varies from the SER of M-QAM signal due to non-uniform constellation shaping, $d_{x_{n,d}}$ of $x_{n,d}$, and $A_d^{[s]}$. The $d_{x_{n,d}}$ of $x_{n,d}$ is considered based on the closest neighbouring CPs. In the case of communication error, the probability of $x_{n,d}$ occurring in CPs other than the closest neighbouring CP region is not considered. If $\mathbf{x}_d$ moves towards the direction of other neighbouring CPs region apart from the closest neighbouring CP region, then the possibility of error decreases due to the increase in $d_{x_{n,d}}$. Hence, this is an upper bound SER for the M-QAM with non-uniform HCS. The SER for individual symbol present in $x_{n,d}$ is denoted as SER_M, which is given as

$$\text{SER}_M[x_{n,d}] \approx \begin{cases} 3\text{SER}_{Ed}, & x_{n,d} = \{\pm\frac{\rho_u(a)}{\rho(a)} a \pm j1\frac{\rho_u(ja)}{\rho(a)}\} \\ 3\text{SER}_{Ed}, & x_{n,d} = \{\pm 1\frac{\rho_u(a)}{\rho(a)} \pm ja\frac{\rho_u(ja)}{\rho(ja)}\} \\ 4\text{SER}_{In}, & x_{n,d} = \{\pm\frac{\rho_u(a)}{\rho(a)}(2m_i - 1) \\ & \qquad \pm j\frac{\rho_u(ja)}{\rho(ja)}(2m_i - 1)\}, \end{cases} \tag{3.9}$$

where if $M = 16$, then $m_i = 1$ or else if $M > 16$, then $m_i = \{1, ..., \frac{\sqrt{M}}{2} - 1\}$ and the SER of symbols in corner CPs are not considered in $\text{SER}_M[x_{n,d}]$. The average SER of all the symbols present in $\mathbf{x}_d$ gives the SER of M-SWIPT signal and it is given as $\text{SER}_M \approx \frac{1}{N}\sum_{n=1}^{N} \text{SER}_M[x_{n,d}]$.

The maximum AIR is one of the performance metrics which is considered for understanding the feasibility of M-SWIPT, since it uses the highest amplitude symbols for EH. The symbol-wise mutual information between input and output symbols of a signal in a finite auxiliary channel with Monte Carlo integration is given in [14, Sec. VI]. This formula is used to find an approximate lower bound AIR for the signal with PAS by using circularly symmetric Gaussian noise statistics as in [13]. The benefit of using Monte Carlo simulation based equation is that the impact of HCS of the given input signal is considered in estimating its AIR. Therefore, as similar to the AIR of PAS, an approximate lower bound AIR for the signal with HCS can be estimated by using [13, Eq.5]. The AIR of M-SWIPT is given as

$$\mathrm{AIR}_M \approx \frac{1}{N}\sum_{n=1}^{N}\log_2\frac{Q_{\mathbf{y}|\mathbf{x}_d}(\mathbf{y}^{[k]}|x_{n,d})}{Q_{\mathbf{y}}(\mathbf{y}^{[k]})}, \tag{3.10}$$

where $\mathbf{y}^{[k]}$ is the output symbol corresponding to the input symbol $x_{n,d}$, and $n = 1,...,N$. Here, $Q_{\mathbf{y}|\mathbf{x}_d}$ and $Q_{\mathbf{y}}$ denotes the auxiliary channel and the auxiliary channel output density, respectively. It is assumed that the transition probability distribution of $Q_{\mathbf{y}|\mathbf{x}_d}$ is same as h. $Q_{\mathbf{y}|\mathbf{x}_d}(\mathbf{y}^{[k]}|x_{n,d})$ and $Q_{\mathbf{y}}(\mathbf{y}^{[k]})$ are derived in [13].

3.2 Numerical results

In this section, four HCS models are presented with M-SWIPT scheme and they are compared with PS-SWIPT to find the best M-SWIPT scheme. Four HCS models are used over a 16-QAM signal, as shown in Tab. 3.1 with 0.05% variation in $\rho(a)$ between each model and they are named as B_j where $j = 1,2,3,4$ and we consider $\rho(a)$ and $\rho(ja)$ are equal and the amplitude of a and ja are equal. These four HCS models are applied[6] on MS_j. We gradually vary $\rho(a)$ in B_j to understand the impact of $\rho(a)$ in the performance of MS_j. In the 16-QAM signal, $x_{n,H} = (\pm 3\big(\frac{\rho_u(a)}{\rho(a)}\big), \pm 3j\big(\frac{\rho_u(ja)}{\rho(ja)}\big))$, where $x_{n,H}$ denotes the highest amplitude symbols. $d_{x_{n,d}}$ for $x_{n,H}$ is denoted as $d_{x_{n,d},H}$ and for the remaining CPs, $d_{x_{n,d}}$ is denoted as $d_{x_{n,d},L}$. B_1 is equal to $\rho_u(a)$. B_2, B_3 and B_4 models has non-uniform probability

Table 3.1: Probability and amplitude of the alphabets, $d_{x_{n,d}}$ of the alphabets in B_j and $H(\mathbf{x})$ of B_j.

B_j	$\rho(a)$	a	$d_{x_{n,d},H}$	$d_{x_{n,d},L}$	$H(\mathbf{x})$
B_1	$\{0.25, 0.25\}$	$\{\pm 3, \quad \pm 1\}$	2	2	4
B_2	$\{0.20, 0.30\}$	$\{\pm 3.3541, \pm 0.9129\}$	2.44	1.83	3.9419
B_3	$\{0.15, 0.35\}$	$\{\pm 3.8730, \pm 0.8452\}$	3.03	1.69	3.7626
B_4	$\{0.10, 0.40\}$	$\{\pm 4.7434, \pm 0.7906\}$	3.95	1.58	3.4439

distribution of a and their respective bit energy value is calculated by using (3.3) as shown in Tab. 3.1. MS_j uses $x_{n,H}$ for EH and the rest of the CPs for IT. MS_1, MS_2, MS_3 and MS_4 uses 25%, 16%, 9% and 4% symbols for EH, respectively. At condition ideal, $\mathfrak{E}_{MS}$ of MS_j is constant with $\zeta = 45\%$. For fair comparison of EH schemes, PS-SWIPT uses B_1 with $(1-\zeta_P) = 45\%$ and it is denoted as $PS_{\zeta_P 1}$. For the energy harvesting simulation set-up, d_{TR} varies from 1 m to 5 m. It is assumed that $\varkappa = 2$, $\eta_{EH} = 0.9$, $P = 50$ dB, $T_s = 1$ second and the signal attenuation is constant at 30 dB. EH at MS_j and $PS_{\zeta_P 1}$ are equal as both the schemes allocate on 45% power for EH. $\mathfrak{E}_{MS} = 0.036, 0.009, 0.004, 0.002$ and 0.0015 at $d_{TR} = 1,2,3,4$ and 5, respectively. $\mathfrak{E}_{MS}$ decreases with the increase in distance due to path loss factor.

Tab. 3.2 illustrates $d_{x_{n,d},L}$ of the alphabets in EH Models, $H(\mathbf{x}_d)$ of MS_j and N_i, N_e, and N of EH models. $d_{x_{n,d},L}$ is calculated for MS_j and $PS_{\zeta_P 1}$ by using (3.5), (3.6) and

[6] In this section, for convenience, we use notation MS_j to denote the subcategory of MS scheme.

Table 3.2: EH models and B_j of the respective EH models, $d_{x_{n,d},L}$ of the alphabets in EH models, $H(\mathbf{x}_d)$ of MS_j, N_i, and N of EH models.

models	B_j	$d_{x_{n,d},L}$	$H(\mathbf{x}_d)$	N_i	N
MS_1	B_1	$2 \times 0.75 = 1.5$	3.5850	10^6	$10^6(100/75)$
MS_2	B_2	$1.83 \times 0.86 = 1.54$	3.5567	10^6	$10^6(100/84)$
MS_3	B_3	$1.69 \times 0.92 = 1.55$	3.4573	10^6	$10^6(100/91)$
MS_4	B_4	$1.58 \times 0.96 = 1.52$	3.2516	10^6	$10^6(100/96)$
$PS_{\zeta_p 1}$	B_1	$2 \times 0.55 = 1.1$	4	10^6	10^6

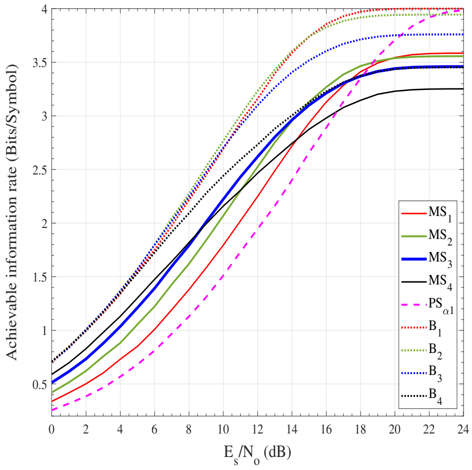

Figure 3.4: A comparison between the AIR of MS_j and $PS_{\zeta_p 1}$

.

$d_{x_{n,d},L}$ of B_j from Tab. 3.1. $d_{x_{n,d},H}$ is not considered as $x_{n,H}$ is not used for IT and for $PS_{\zeta_p 1}$, $d_{x_{n,d},H} = d_{x_{n,d},L}$. For MS_3, $d_{x_{n,d},L} = 1.69 \times 0.917 = 1.55$, where $d_{x_{n,d},L}$ of B_3 is 1.69 and P_m of $x_{n,d}$ is 91.7%. In case of $PS_{\zeta_p 1}$, $d_{x_{n,d},H} = d_{x_{n,d},L}$ for B_1 model and $d^1_{x^[_d k]} = 2 \times 0.75 = 1.50$, where $d_{x_{n,d},L}$ of B_1 is 2 and P of $x_{n,d}$ is 75%. Similarly, $d_{x_{n,d},L}$ of symbols in MS_j are calculated.

To analyse SER and AIR performance of MS_j and $PS_{\zeta_p 1}$, we set $P = 1$ and the distance is not considered in this set-up. Fig. 3.4 illustrates the AIR of MS_j and B_j, and $PS_{\zeta_p 1}$. In general, the AIR performance is in the order of $B_1 > B_2 > B_3 > B_4$ with the increase in non-uniform HCS. For SNR region from 0 dB to 16.5 dB, all MS_j performs better than $PS_{\zeta_p 1}$ and particularly the performance improves with the increase in degree of HCS because in MS_j other than the $x_{n,H}$ symbols, $x_{n,d}$ does not suffer energy loss. Also the amount of energy loss of $x_{n,d}$ is comparatively lesser in MS_j with the increase in degree of HCS. At any SNR greater than 7 dB, $PS_{\zeta_p 1}$ performs better than MS_j because MS_j does not use $x_{n,H}$ symbols for IT. After 20 dB SNR, MS_j saturates at its respective $H(\mathbf{x}_d)$ as illustrated in Tab. 3.2. While considering a broader operating SNR region in Fig. 3.4, i.e., from 0 dB to 15 dB SNR, MS_3 performs better than MS_j and $PS_{\zeta_p 1}$ until 15 dB and 18 dB SNR, respectively. MS_3 has a SNR gain in the range of 1.5 dB to 3.5 dB over $PS_{\zeta_p 1}$

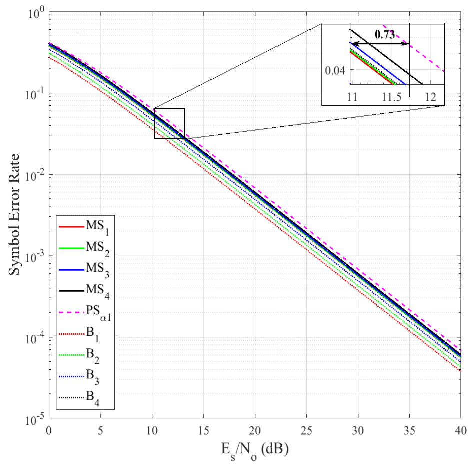

Figure 3.5: A comparison between SER of MS_j and $PS_{\zeta_p 1}$.

from 0 dB to 16 dB SNR.

Fig. 3.5 illustrates upper bound SER of MS_j and B_j, and the SER of $PS_{\zeta_p 1}$. In general, the SER performance is in the order of $B_1 > B_2 > B_3$ because higher order modulated symbols and $d_{x_{n,d}}$ is in the order of $B_1 > B_2 > B_3$ as in Tab. 3.1. The performance of MS_j as compared to that of B_j shows that SER does not changes within MS_j as like in B_j, this is due to similar $d_{x_{n,d}}$ as result of power compensation which is illustrated in Tab. 3.2 and Fig. 3.3. Performance within EH schemes shows that, the performance of MS_j is better due to less amount of energy loss for $x_{n,d}$. Both Tab. 3.2 and Fig. 3.3 illustrate that $d_{x_{n,d},L}$ of MS_j is better than $PS_{\zeta_p 1}$ and, $d_{x_{n,d},L}$ of MS_3 is better than MS_1 as explained in Sec. 3.1.3. Therefore by considering $d_{x_{n,d},L}$ of MS_3 and $PS_{\zeta_p 1}$, even with the same power allocation for EH, at 11 dB SNR, the difference in $d_{x_{n,d}}$ helps MS_3 to outperform $PS_{\zeta_p 1}$ by around 1 dB SNR gain.

3.3 Conclusions

In this chapter, we introduced a new SWIPT technique described as M-SWIPT technique. This scheme can be implemented in any modulation and improves the energy efficiency of low amplitude symbols as compared to traditional PS-SWIPT. We studied the impact of CPs in EH using hybrid constellation shaping to improve the spectral efficiency. It was shown that M-SWIPT has better SER performance as compared to PS-SWIPT. It can also outperform PS-SWIPT in terms of achievable rates.

4

Frequency-Splitting SWIPT Signals with Strong Nonlinear Distortion Effects

In this chapter, we see another novel symbol allocation based SWIPT technique. FS-SWIPT technique allocates part of the available bandwidth for EH purposes and the rest of the frequency band for data transmission. The use of OFDM schemes with FS-SWIPT techniques is a natural option, since it can combine the advantages of both [64] and in [65], symbols belonging to specific frequency subcarriers are used for EH, while the remaining symbols are used for data transmission. One of the first references of FS-SWIPT in the literature is [66]. The frequency splitting or frequency bifurcation at the receiver is studied in [67], [68]. The performance of FS-SWIPT technique is comprehensively studied using a practical experimental prototype in [69] and for example in [70], it is discussed for possible biomedical application in neural prostheses devices.

It is well known that multicarrier systems such as OFDM are particularly suitable for high rate transmission over severely frequency selective channels, since they decompose the available band in multiple sub-channels (usually called "subcarriers") with narrow bandwidth, simplifying the receiver design and allowing flexible allocation of resources. However, multicarrier signals in general and OFDM signals in particular can have significant envelope fluctuations and a high PAPR, which makes them very prone to nonlinear effects, such as the ones associated to an efficient power amplification [71] and digital clipping [72], which can cause severe Nonlinear distortion (NLD) and considerable performance degradation. By combining OFDM with FS-SWIPT, we can expect an even worse situation, since we are usually combining the high power EH subcarriers with the comparatively lower power data subcarriers.

Since working in the linear region of typical nonlinear devices is not feasible in most scenarios (e.g., for High power amplifier (HPA), this would mean having large backoff and, consequently, reduced amplification efficiency [73]), there are several approaches to cope with nonlinear effects in OFDM signals. By using pre-distortion techniques [74, 75], we can linearize amplifiers, but only up to the saturation level (in practice, an ideal pre-distortion turns a given amplification characteristic into an envelope clipping). As an alternative, we can employ iterative receivers that estimate and cancel the nonlinear distortion [76]. Although these receivers can have excellent performance at high SNR, there can be error propagation effects at medium and, especially at low SNR. Finally, we can take advantage of the information on the nonlinear distortion term to improve the performance [77].

The number of existing works that concern nonlinear distortion effects on SWIPT signals are relatively small, especially for the particular scenario of FS-SWIPT. One of the few papers addressing this issue is [78], where FS-SWIPT is used in such a way that the high power signal is transmitted only in a specific frequency band but the leakage NLD from EH subcarriers to data subcarriers is not considered.

In this chapter, we study analytically and by simulation the impact of NLD effects on the performance of FS-SWIPT signals, as well as ways of overcoming those effects. The main contributions of this chapter are the following:

- We present a simple, yet accurate analytical characterization of FS-SWIPT signals submitted to nonlinear devices. This characterization combines the use of Bussgang theorem, to decompose the nonlinearly distorted signal as the sum of uncorrelated useful and distortion terms, with the spectral characterization of those signals using Intermodulation product (IMP) analysis. This characterization is then used to obtain the signal-to-noise plus interference levels for the different subcarriers. It is shown that performance degradation due to nonlinear effects on FS-SWIPT signals are much higher than with conventional OFDM signals, especially for the data subcarriers close to the EH subcarriers.

- We present an iterative receiver, inspired on Bussgang receivers for conventional OFDM signals, that estimates and cancels NLD effects. It is shown that, in spite of the stronger NLD effects, we can still have good performance with that iterative receiver. The good performance of this receiver is due to the fact that the signals associated with high-power EH subcarriers are known and do not need to be estimated, leading to more accurate estimates of the NLD term, even in the presence of decision errors in the data estimates. Therefore, by employing this receiver the Bit error rate (BER) of nonlinear FS-SWIPT signals can almost match the BER associated to linear transmissions.

- Finally, we study the optimum performance of nonlinearly distorted FS-SWIPT signals. Contrarily to the OFDM case, where stronger NLD levels can lead to higher performance gains for the optimum receiver [77], it is shown that performance gains for the nonlinear FS-SWIPT case relatively decrease with the increase in the power of the EH component. However, the NLD can still lead to performance improvements when compared with the linear transmission scenario.

This chapter is organized as follows: The characterization of the FS-SWIPT system considered in this chapter is described in Section **??**. Section 4.2 presents the analytical characterization of FS-SWIPT signals submitted to nonlinear devices and Section 4.3.2 presents a novel iterative receiver that estimates and compensates NLD effects in FS-SWIPT signals. The optimum performance of nonlinear FS-SWIPT signals is studied in Section 4.3.3 and then, the performance of the proposed receivers is analysed in Section **??**. Finally, Section **??** concludes the chapter.

4.1 System Model

In this work, we consider a point-to-point communication system based on an FS-SWIPT OFDM scheme. The main blocks of the system are shown in Fig. 5.1. The subcarrier

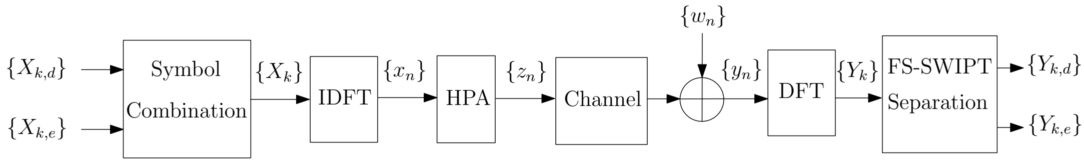

Figure 4.1: OFDM-based FS-SWIPT system model with a nonlinear transmission chain.

allocation scheme of the FS-SWIPT system is represented in Fig. 4.2. As can be noted, the OFDM signal has a central band dedicated to the transmission of energy symbols for EH and two sidebands adopted for the transmission of data symbols. With the EH subcarriers in the central part of the spectrum, it is easier to meet specific out-of-band radiation requirements since, as it will be shown, most NLD effects are in the vicinity of the EH subcarriers, which usually have much higher power than the subcarriers used for data transmission. Therefore, most of the nonlinear distortion is well within the data subcarriers instead of spreading on the adjacent channels. Even though this could lead to performance degradation, these effects can be minimized with our iterative receiver (see Section 4.3.2), and can actually lead to performance gains if an optimum detection is considered (see Section 4.3.3).

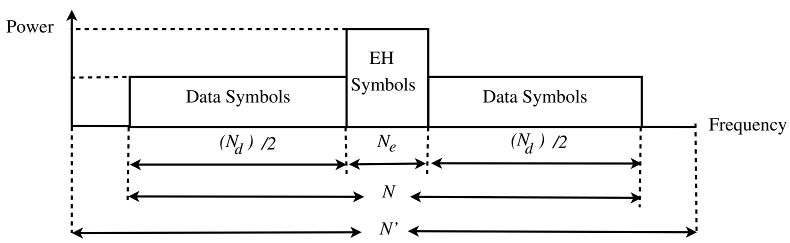

Figure 4.2: Subcarrier allocation for the considered FS-SWIPT OFDM system.

The frequency-domain OFDM symbols are denoted as $\{X_k; k = 0, 1, \cdots, N' - 1\}$, where N' is the total number of subcarriers, from which $N' - N$ are left idle for oversampling purposes (i.e., $M = N'/N$ is the oversampling factor). From the N used subcarriers, we consider that N_e are dedicated to EH and $N_d = N - N_e$ are used for data transmission. The ratio between the number of subcarriers used for EH to the total number of used subcarriers is denoted as $\zeta = N_e/N$. Note that on one hand, ζ should take relatively low values to avoid compromising the system spectral efficiency for data transmission (which is upper-bounded by $1-\zeta = N_d/N$). On the other hand, small values of N_e make the EH component very prone to fading effects[1].

The data symbols are denoted as $X_{k,d}$ and occupy the indexes $k \in \chi_d$, with the set $\chi_d = \{\frac{N'}{2}-\frac{N_d}{2}, \frac{N'}{2}-\frac{N_d}{2}+1, \cdots, \frac{N'}{2}-\frac{N_e}{2}-1\} \cup \{\frac{N'}{2}+\frac{N_e}{2}, \frac{N'}{2}+\frac{N_e}{2}+1, \cdots, \frac{N'}{2}+\frac{N_e}{2}+\frac{N_d}{2}-1\}$. The EH symbols are denoted as $X_{k,e}$ and occupy the indexes $k \in \chi_e$, with the set $\chi_e = \{\frac{N'}{2}-\frac{N_e}{2}, \frac{N'}{2}-\frac{N_e}{2}+1, \cdots, \frac{N'}{2}+\frac{N_e}{2}-1\}$. Regardless of their type, all symbols are selected from quadrature phase shift keying (QPSK) constellations (the generalization to other constellations or to the case where different constellations are employed in different subcarriers is straightforward). However, while the data symbols are of the form $X_{k,d} = \pm 1 \pm j$, which means $\mathbb{E}[|X_{k,d}|^2] = 2$, the EH symbols are defined as $X_{k,e} = \pm A \pm jA$, i.e., $\mathbb{E}[|X_{k,e}|^2] = 2A^2$.

The time-domain OFDM samples are obtained by taking the IDFT of X_k, i.e., $\{x_n = \mathrm{IDFT}(X_k); n = 0, 1, \cdots, N'-1\}$. A given time-domain sample can be separated into two terms, one representing the contribution of the data subcarriers and another representing the contribution of the EH subcarriers, i.e.,

$$x_n = x_{n,d} + x_{n,e}. \tag{4.1}$$

The average power of data symbols and the average power of the EH symbols are denoted as P_d and P_e respectively, where P_d and P_e are calculated as:

$$\begin{aligned}
P_d &= \mathbb{E}\left[\left|x_{n,d}\right|^2\right] \\
&= 2\sigma_d^2 = \frac{1}{N'^2}\sum_{k\in\chi_d}\mathbb{E}\left[\left|X_{k,d}\right|^2\right] = \frac{2N_d}{N'^2}, \\
P_e &= \mathbb{E}\left[\left|x_{n,e}\right|^2\right] \\
&= 2\sigma_e^2 = \frac{1}{N'^2}\sum_{k\in\chi_e}\mathbb{E}\left[\left|X_{k,e}\right|^2\right] = \frac{2A^2N_e}{N'^2},
\end{aligned} \tag{4.2}$$

with σ_d^2 and σ_e^2 denoting the variance of $x_{n,d}$ and $x_{n,e}$, respectively. Note that $P_e \gg P_d$, i.e., the power associated with the EH signal is much higher than the power associated with the data transmission signal. The relation between these powers is given by

$$\beta = \frac{P_e}{P_d} = \frac{N_e A^2}{N_d}. \tag{4.3}$$

[1] By spreading the EH subcarriers over the transmission band we could reduce the EH susceptibility to fading, but this leads to implementation difficulties (e.g., it complicates the filtering used to remove the EH signal).

It should be noted that the amplitude of QPSK symbols dedicated to EH (i.e., the value of A) is defined according to the values of β and ζ, i.e.,

$$A^2 = \beta \frac{1-\zeta}{\zeta}. \tag{4.4}$$

The total average power of the FS-SWIPT OFDM signal is

$$\begin{aligned} P &= P_d + P_e \\ &= \mathbb{E}\left[|x_n|^2\right] = 2\sigma_x^2 = \frac{1}{N'^2} \sum_{k \in \chi_e} \mathbb{E}\left[|X_k|^2\right], \end{aligned} \tag{4.5}$$

where σ_x^2 is the variance of the real and imaginary parts of x_n.

4.2 Analytical Characterization of Nonlinear FS-SWIPT Signals

In this section, we present the analytical characterization of nonlinearly distorted FS-SWIPT OFDM signals considering both the time and frequency domain. For readers' convenience, we start by presenting some preliminary general definitions that are important for understanding those characterizations.

4.2.0.1 Preliminary Definitions

We represent the continuous time-domain version of the baseband FS-SWIPT signal (i.e., the analog version of the time-domain samples $\{x_n; n = 0, 1, \cdots, N'-1\}$) by the function $x(t)$. The autocorrelation of $x(t)$ is defined as $R_{xx}(\tau) = \mathbb{E}[x(t)x^*(t-\tau)]$, where τ represents a given time delay. By defining the nonlinearly distorted version of $x(t)$ as $z(t)$, we can write the cross-correlation between $x(t)$ and $z(t)$ as $R_{xz}(\tau) = \mathbb{E}[x(t)z^*(t-\tau)]$. When it comes to the discrete time, we define the autocorrelation of a sequence $\{x_n; n = 0, 1, \cdots, N'-1\}$ as $\{R_x(n-n') = \mathbb{E}[x_n x_{n'}^*]; n, n' = 0, 1, \cdots, N'-1\}$. Regarding the frequency domain, the power spectral density (PSD) of the complex envelopes $x(t)$ and $z(t)$ are represented as $G_x(f)$ and $G_z(f)$, respectively, with $G_x(f) = \mathcal{F}(R_{xx}(\tau))$ and $G_z(f) = \mathcal{F}(R_{zz}(\tau))$, where $\mathcal{F}(\cdot)$ is the Fourier transform operator. We also define the PSD of the discrete version of FS-SWIPT signals $\{X_k; k = 0, 1, \cdots, N'-1\}$ as $G_x(k) = \mathbb{E}[|X_k|^2]$. The discrete autocorrelations and PSDs are related by the discrete Fourier transform (DFT) and the inverse discrete Fourier transform (IDFT). More concretely, the autocorrelation of the input signal can be written as

$$R_{xx}(n-n') = \frac{1}{N'^2} \sum_{k=-N/2}^{N/2-1} G_x(k) e^{j2\pi \frac{k(n-n')}{N'}}, \tag{4.6}$$

with $\{R_{xx}(n-n'); n, n' = 0, 1, \cdots, N'-1\} = \frac{1}{N'}\text{IDFT}\ \{G_x(k); k = 0, 1, \cdots, N'-1\}$.

4.2.0.2 Gaussian Approximation

It is widely known that OFDM signals have large envelope fluctuations. In that sense, OFDM signals can be approximately modeled by a Gaussian random process, especially when the number of subcarriers is large [79]. Under these conditions, the absolute value of the complex envelope $x(t)$, given by $r(t) = |x(t)|$, has an approximate Rayleigh distribution with probability density function (PDF) defined as in [80]:

$$p(r) = \frac{r}{\sigma_x^2} \exp\left(-\frac{r^2}{2\sigma_x^2}\right), \quad r \geq 0, \tag{4.7}$$

where r is a random variable that models the absolute value of the complex envelope of FS-SWIPT OFDM signals. Fig. 4.3 shows the simulated and theoretical PDF (given by (4.7)) of the envelope of the FS-SWIPT OFDM signals considering $\beta = 10$ dB and different values of ζ. As can be noted in that figure, the PDF represented in (4.7) presents a

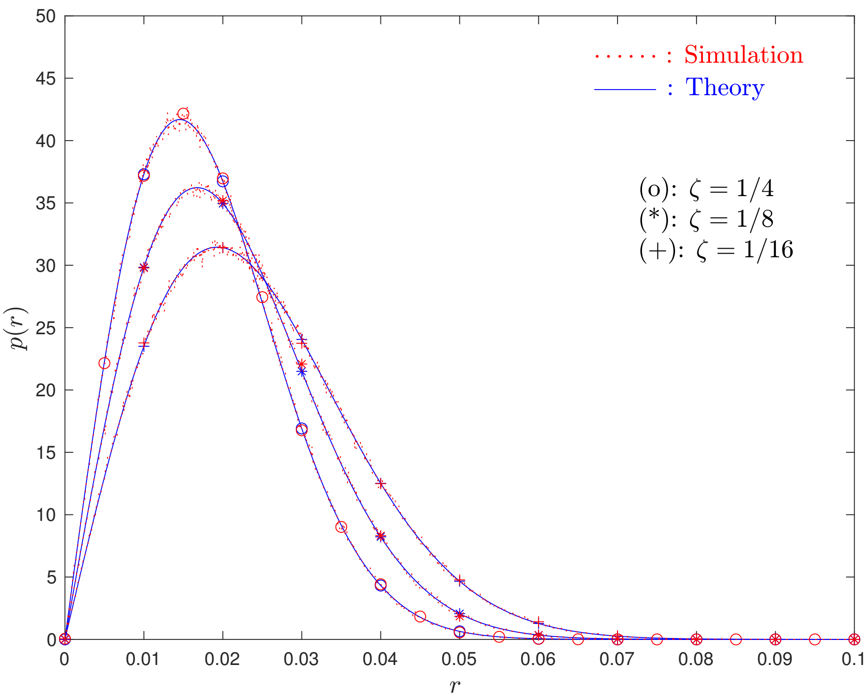

Figure 4.3: Simulated and theoretical PDF of the envelope of the FS-SWIPT OFDM considering $\beta = 10$ dB and different values of ζ.

high degree of accuracy to model the statistical distribution of the envelope of FS-SWIPT OFDM signals.

4.2.1 Nonlinear FS-SWIPT OFDM Signals

Conventional OFDM signals can easily drive the HPA into the saturation region, leading to severe NLD effects. This can be explained by the high PAPR of the signals, combined with the nonlinear nature of the HPA, which typically exhibits a nonlinear characteristic. In FS-SWIPT schemes, this problem can be even worse since the power among the subcarriers is not constant, which can lead to even higher envelope fluctuations. In this work, we consider an HPA in the transmission chain, and we modeled it as a general memoryless bandpass nonlinearity [81]. By using the bandpass model, we can write the complex envelope of the HPA output as

$$z(t) = f_a(r(t))\exp(j\left(\arg(r(t)) + f_p(r(t))\right), \tag{4.8}$$

where $f_a(\cdot)$ is the amplitude-to-amplitude conversion function (AM/AM) and $f_p(\cdot)$ is the amplitude-to-phase conversion function (AM/PM). In this work, we specifically consider Rapp's model for the HPA [82], although our analysis is valid to any bandpass memoryless nonlinearity model (this includes the Saleh model [83], as well as simple envelope clipping models that arise when ideal predistortion techniques are employed [84]). In Rapp's model, we have an approximately null AM/PM function, i.e., $f_p(r(t)) \approx 0$, and an AM/AM function is characterized by

$$f_a(r(t)) = \frac{|r(t)|}{\sqrt[2q]{1+\left(\frac{|r(t)|}{s_M}\right)^{2q}}}, \tag{4.9}$$

where s_M is the clipping level and q is the sharpness factor, which is associated with the smoothness of the transition between linear and nonlinear operating regions of the amplifier's characteristic. To analyze the severity of the NLD effects independently from the input power of the nonlinearity, we define the normalized clipping level as $\frac{s_M}{\sigma_x}$ and if $\frac{s_M}{\sigma_x}$ is higher, then the severity of the NLD effects will be lower.

4.2.2 Time-domain Characterization of Nonlinear FS-SWIPT OFDM Signals

By taking advantage of the Gaussian nature of FS-SWIPT OFDM signals, one can consider the Bussgang's theorem to have an alternative representation of their nonlinearly distorted version [85]. In that representation, $z(t)$ can be separated into two uncorrelated terms: a scaled replica of the input signal $x(t)$ and distortion term $d(t)$, i.e.,

$$z(t) = \alpha x(t) + d(t), \tag{4.10}$$

where α is the scaling factor of $x(t)$, which is the scaled cross correlation between the input and output signals of the nonlinearity (in our case, the HPA) and can be calculated[2] as

$$\alpha = \frac{R_{xz}(0)}{R_{xx}(0)} = \frac{\mathbb{E}[rf_a(r)]}{2\sigma_x^2} = \frac{1}{2\sigma_x^2}\int_0^\infty rf_a(r)p(r)dr. \tag{4.11}$$

By using Bussgang's theorem, we can represent the nonlinearly distorted signal at the nth time instant as $\{z_n; n = 0, 1, \cdots, N'-1\}$, with

$$z_n = \alpha x_n + d_n. \tag{4.12}$$

[2]Since the input signal $x(t)$ is approximately stationary, the time dependence of r (and, consequently, of α) is omitted in (4.11).

4.2.3 Frequency-domain Characterization of Nonlinear FS-SWIPT OFDM Signals

In this section, our main goal is to obtain the PSD of the nonlinearly distorted FS-SWIPT OFDM signals. By considering Bussgang's theorem, we can define the frequency-domain version of the nonlinearly distorted FS-SWIPT OFDM signals as the DFT of (4.12), i.e., $\{Z_k; k = 0, 1, \cdots, N' - 1\} = \text{DFT}\ \{z_n; n = 0, 1, \cdots, N' - 1\}$. Under these conditions, the symbol at kth subcarrier at the nonlinearity output can be written as

$$Z_k = \alpha X_k + D_k, \tag{4.13}$$

where $\{D_k; k = 0, 1, \cdots, N' - 1\} = \text{DFT}\ \{d_n; n = 0, 1, \cdots, N' - 1\}$.

Since the PSD and the autocorrelation are related by the DFT (see (4.6)), we can obtain the PSD of FS-SWIPT OFDM signals by computing first the autocorrelation of the nonlinearly distorted signal and then obtain its DFT, i.e., $G_z(k) = \mathbb{E}[|Z_k|^2] = \text{DFT}(R_{zz}(n - n'))$. In [86, 87] it is shown that the autocorrelation function of a nonlinearly distorted signal can be computed theoretically as a function of the autocorrelation of the input signal, namely

$$\begin{aligned} &R_{zz}(n-n') \\ &= \sum_{\mu=0}^{+\infty} 2\rho_{2\mu+1} \frac{(R_{xx}(n-n'))^{\mu+1}(R_{xx}^*(n-n'))^{\mu}}{(R_{xx}(0))^{\mu+1}}, \end{aligned} \tag{4.14}$$

where $\rho_{2\mu+1}$ denotes the power associated to the IMP of order $2\mu+1$, which can be computed as explained in [86, 88]. The PSD of the distortion component $G_d(k) = \mathbb{E}[|D_k|^2]$ is given by the DFT of the autocorrelation of the distortion term, which is obtained by discarding the contribution of the first IMP (i.e., the term associated with $\mu = 0$) in (4.14).

In the following, a set of results regarding the frequency-domain characterization of nonlinearly distorted FS-SWIPT signals are presented. In all these results, it is assumed that $N' = 2048$ and $N = 512$ (i.e., an oversampling $M = 4$ is adopted for accurate characterization of the NLD effects).

Fig. 4.4 shows the simulated and theoretical PSD of nonlinearly distorted FS-SWIPT OFDM signals considering $\beta = 15$ dB and different values of s_M/σ_x and ζ. From the figure, it can be noted that (4.14) shows a great degree of accuracy, with a very close match between theoretical and simulated PSD results. The same degree of accuracy can be observed in Fig. 4.5, which shows the PSD of the distortion component considering the same values of β, s_M/σ_x and ζ used in Fig. 4.4. From this figure, it can be noted that the lower the clipping level, the higher the level of nonlinear distortion. Moreover, as expected, the EH subcarriers have stronger distortion since these subcarriers have a much higher power. The main disadvantage of using EH subcarriers is the effect of distortion spreading from those subcarriers to the ones associated with data transmission.

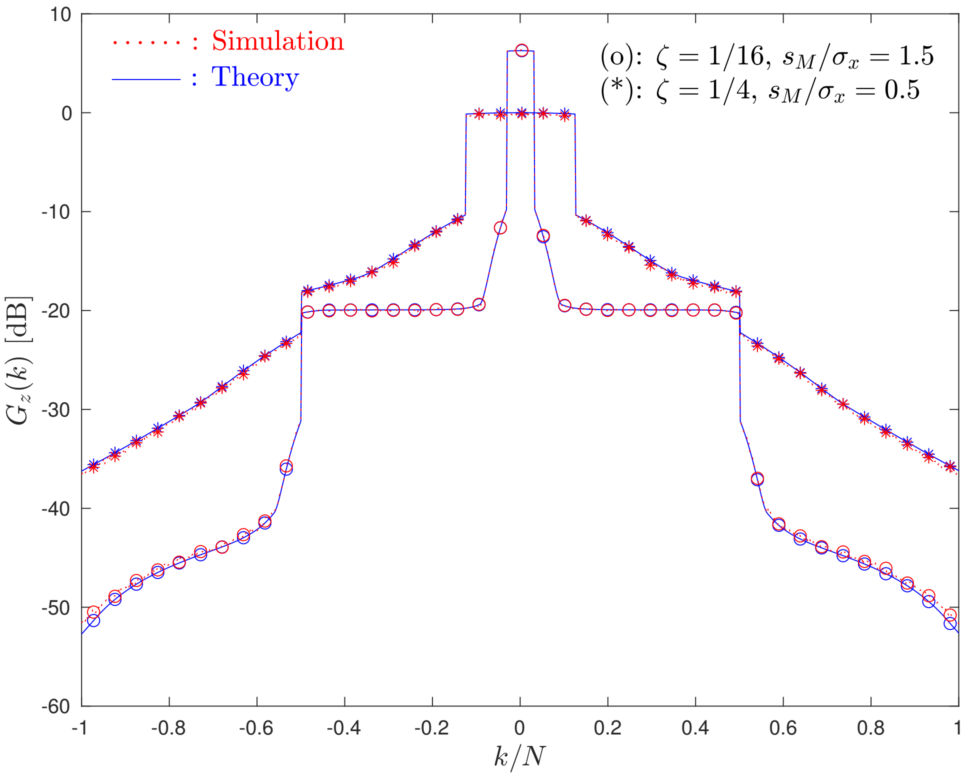

Figure 4.4: Simulated and theoretical PSD of nonlinearly distorted FS-SWIPT OFDM signals considering $\beta = 15$ dB.

4.2.4 Self-to-interference ratio

To evaluate the NLD levels on the system's performance, one can define the self-interference ratio (SIR), which is given by the ratio between the power of the useful signal to the power of the distortion component, i.e.,

$$\mathrm{SIR}_k = \frac{|\alpha|^2 \mathbb{E}[|X_k|^2]}{\mathbb{E}[|D_k|^2]} = |\alpha|^2 \frac{G_x(k)}{G_d(k)}. \tag{4.15}$$

(due to the non-flat nature of the nonlinear distortion PSD, the SIR levels depend on the subcarrier, i.e., they are a function of the subcarrier index k).

Fig. 4.6 shows the simulated and theoretical SIR levels for FS-SWIPT OFDM signals considering $\beta = 15$ dB and different values of s_M/σ_x and ζ. Once again, our analytical results are very accurate, being observed by a close matching between theoretical and simulated results. As expected, the lower the normalized clipping level, the higher the NLD levels. It can also be noted that the SIR is much higher at the middle of the band, i.e., in the N_e subcarriers dedicated to EH. However, since these are not used for data transmission purposes, the SIR is only meaningful for the remaining N_d subcarriers. For those, it can be noted that the SIR levels are much higher close to the EH subcarriers, with large variations throughout the data subcarriers.

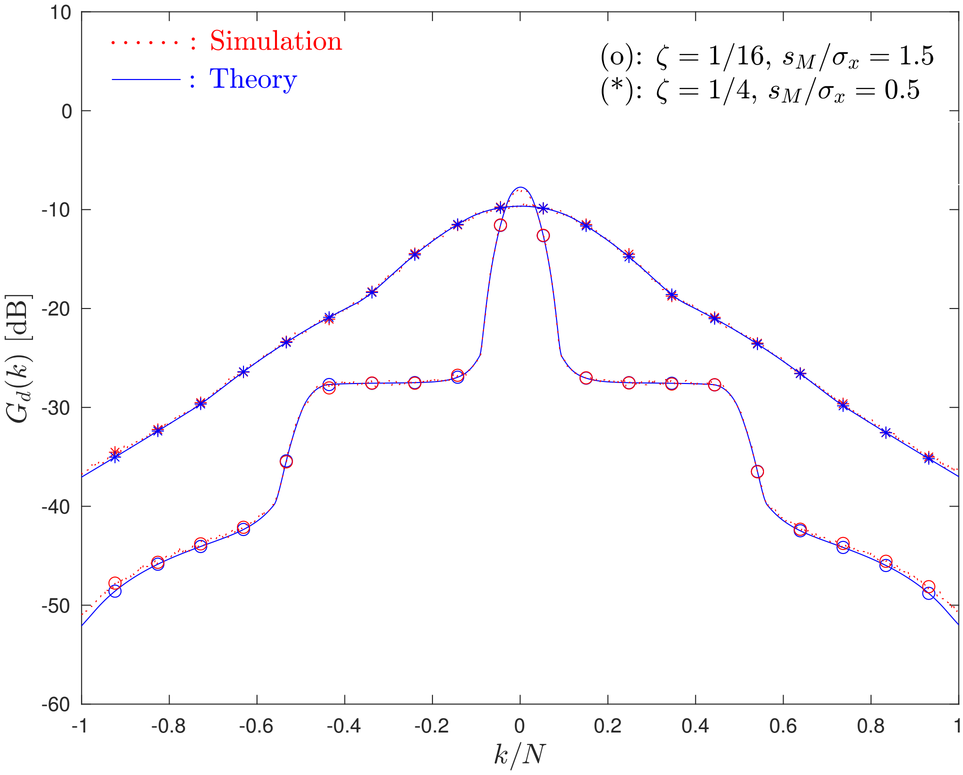

Figure 4.5: Simulated and theoretical PSD of the NLD term considering nonlinearly distorted FS-SWIPT OFDM signals with $\beta = 15$ dB.

Fig. 4.7 shows the average SIR (average along all the N in-band subcarriers), the maximum SIR, and the minimum SIR, considering different values of β, s_M/σ_x and ζ. As can be noted, all these quantities related to the SIR increase with the clipping level and decrease with β.

4.3 Receiver Design for Nonlinearly Distorted FS-SWIPT OFDM Signals

4.3.1 Received Signal

Let us consider a signal transmission over a frequency-selective channel (e.g., a multipath channel with Rayleigh fading on the different multipath components). The channel frequency response for the kth subcarrier is denoted by H_k (since we are interested in the achievable performance, we assumed perfect channel knowledge in this paper; in practice, the channel can be estimated from suitable pilots or training sequences, as with conventional OFDM schemes). The received signal associated with the kth subcarrier can be written as

$$Y_k = H_k Z_k + W_k = \alpha H_k X_k + H_k D_k + W_k, \tag{4.16}$$

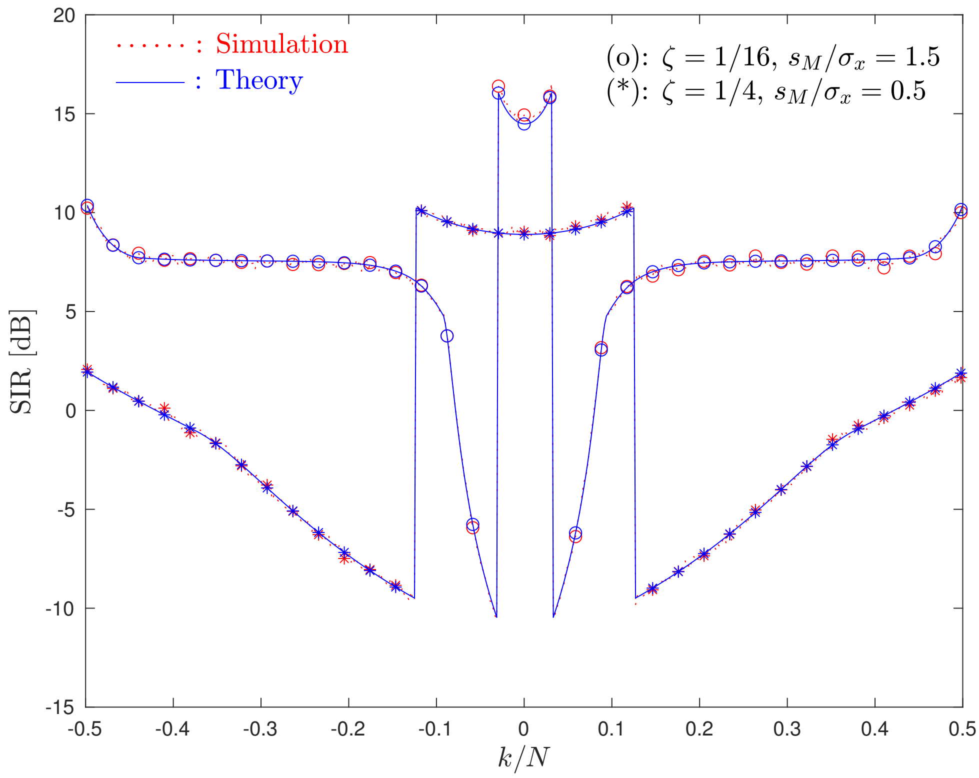

Figure 4.6: Simulated and theoretical SIR considering $\beta = 15$ dB.

where $\alpha H_k X_k$ is the scaled version of the useful signal and $H_k D_k$ and W_k are the NLD and the noise component associated to the kth subcarrier, respectively.

The NLD term at the subcarrier level, D_k, is approximately Gaussian [79]. Conventional OFDM receivers treat it as an additional noise-like term that is added to the channel noise. As such, their performance is a function of the signal-to-noise plus distortion ratio (SNDR), which is given by

$$\text{SNDR}_k = \frac{|\alpha|^2 \mathbb{E}[|H_k X_k|^2]}{\mathbb{E}[|W_k|^2] + \mathbb{E}[|H_k D_k|^2]}, k \in \chi_d. \tag{4.17}$$

It can be shown that SNDR_k can be obtained from $|H_k|^2$ and SIR_k as follows

$$\text{SNDR}_k = \frac{|H_k|^2}{\frac{|H_k|^2}{\text{SIR}_k} + \frac{1}{\text{SNR}_k}}, k \in \chi_d \tag{4.18}$$

where SIR_k can be theoretically obtained with (4.15) and the SNR for the data subcarriers is defined as

$$\text{SNR}_k = \frac{|\alpha|^2 \mathbb{E}[|X_{k,d}|^2]}{\mathbb{E}[|W_k|^2]}, k \in \chi_d. \tag{4.19}$$

Since the NLD term is approximately Gaussian distributed at the subcarrier level, the corresponding BER of conventional receivers can be directly obtained from SNDR_k [79].

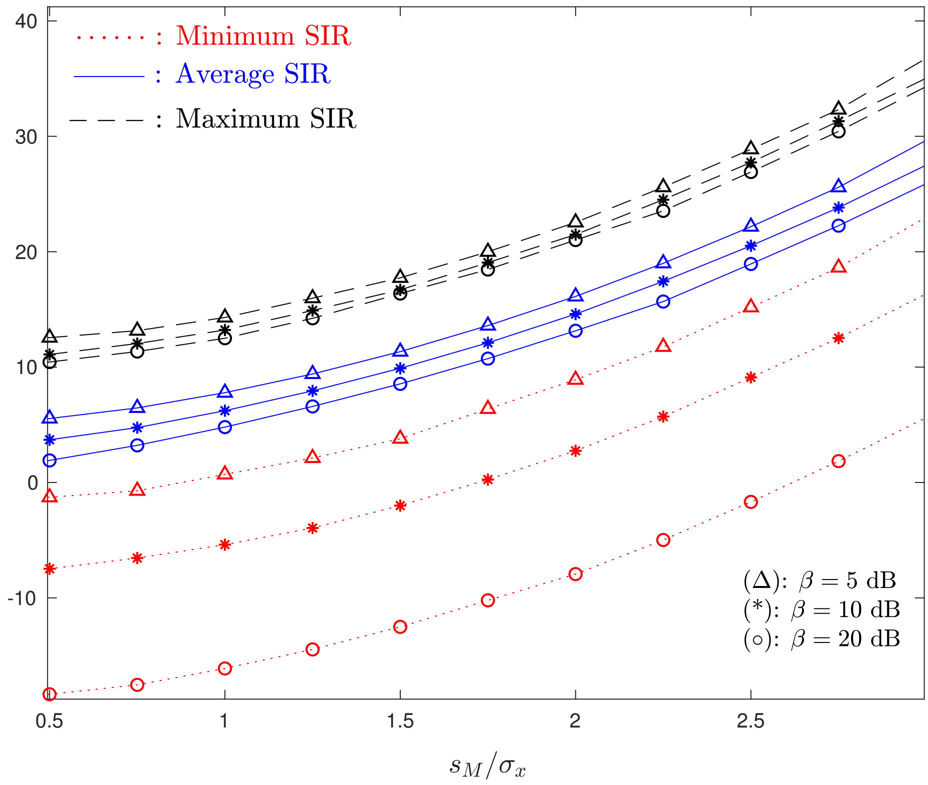

Figure 4.7: Evolution of the average, maximum and minimum SIR with the normalized clipping level and β.

For QPSK constellations the BER of the kth subcarrier is

$$BER_k = Q\left(\sqrt{\mathrm{SNDR}_k}\right). \tag{4.20}$$

The generalization for other constellations is straightforward [63, Sec. 5.2.2]. The SNDR_k values can also be used for obtaining the log-likelihood ratio of the different bits, required for soft decision decoding of turbo codes, low-density parity-check codes, and other coding schemes.

It should also be noted that for a given operating point of the nonlinear device, the power of the NLD term increases with the average power of the input signal x_n. Therefore, the introduction of high powered $X_{k,e}$ symbols in X_k can negatively impact the detection performance due to the decreased SIR_k levels, especially for the subcarriers close to the EH region.

4.3.2 Iterative Bussgang Receivers

As pointed out in the previous section, FS-SWIPT OFDM signals are much more prone to NLD effects than conventional OFDM signals, especially when β is large. In this section, we propose an iterative receiver for nonlinearly distorted FS-SWIPT OFDM signals that takes advantage of Bussgang's theorem. As with the so-called "Bussgang receivers"for conventional OFDM, the basic idea is to estimate and remove the nonlinear distortion term of the received signal (see (4.16)) in an iterative way so that its impact on the performance can be mitigated. Whereas the "conventional Bussgang receiver"does not use the estimates of data and distortion term as feedback in an iterative way to remove distortion term and therefore the iterative receiver is expected to have better performance. The proposed receiver structure is depicted in Fig. 4.8. The receiver operates in an iterative

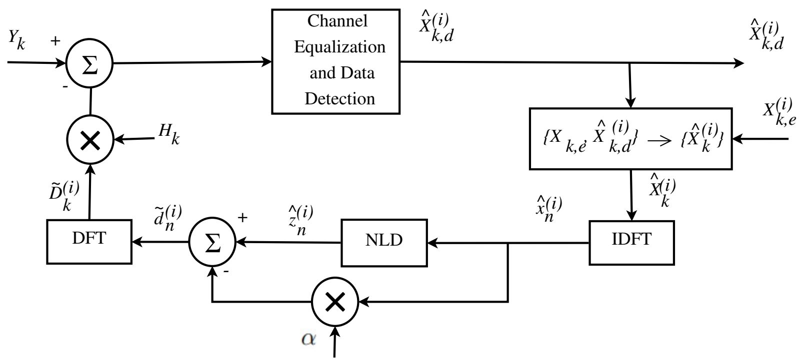

Figure 4.8: Joint signal detection and NLD compensation receiver.

fashion and has two main blocks: a data estimation block and NLD estimation block. To estimate the NLD, the receiver needs to employ the same nonlinearity used in the transmitter as well as an estimate of the transmitted signal (naturally, the receiver only needs to estimate the transmitted data symbols, since the EH symbols are known). With the data estimate, the receiver estimates the NLD and cancels it from the received signal. This process is repeated iteratively. Note that the estimate of $X_{k,d}$ for the ith iteration is given as

$$\tilde{X}^{(i)}_{k,d} = Y_{k,d} - \tilde{D}^{(i)}_{k,d} H_k, \tag{4.21}$$

where $\tilde{D}^{(i)}_{k,d}$ is an estimate of NLD term obtained from $\hat{X}^{(i-1)}_k$, which is 'hard decision' estimate of X_k where $X_{k,d}$ is replaced by their estimates $\hat{X}^{(i)}_{k,d}$ (naturally, in the first iteration, we have $\tilde{D}^{(0)}_{k,d} = 0$). The samples $\hat{x}^{(i)}_{n,d}$ and $\hat{x}^{(i)}_n$ are the 'hard decision' estimates of $x_{n,d}$ and x_n, respectively (i.e., the IDFTs of the corresponding frequency-domain blocks). Assuming that the nonlinear characteristic that takes place at the transmitter is known by the receiver, we can obtain the NLD estimates from

$$\tilde{d}^{(i)}_n = \hat{z}^{(i)}_n - \alpha \hat{x}^{(i)}_n, \tag{4.22}$$

where $\hat{z}^{(i)}_n = f(\hat{x}^{(i)}_n)$ and $f(\cdot)$ represents the nonlinear operation. From the time-domain NLD estimates $\tilde{d}^{(i)}_n$, we can obtain the corresponding frequency-domain NLD estimates $\{\tilde{D}^{(i)}_k; k = 0, 1, \cdots, N'-1\} = \text{DFT}\ \{\tilde{d}^{(i)}_n; n = 0, 1, \cdots, N'-1\}$. Therefore, estimates $\tilde{X}^{(i)}_{k,d}$ and $\tilde{D}^{(i)}_{k,d}$ can be improved by using (4.21) and (4.22) in an iterative way.

The error propagation effects are the most common problem associated with the receivers that estimate NLD and then cancel it from the received signal. However, in our scenario the error propagation effects can be limited, since part of the estimates in $\hat{X}_k^{(i)}$ are error-free, i.e., the EH symbols ($X_{k,e}$). In fact, although EH symbols have more NLD effects as compared to data symbols, they are already known to the receiver, which means that the reliability of this receiver increases with the increase of ζ. The reliability of the data estimates at the ith iteration can be defined as

$$\Psi = \frac{\mathbb{E}[|\hat{X}_k^{(i)} X_k^*|]}{\mathbb{E}[|X_k|^2]}. \tag{4.23}$$

The BER performance of this iterative receiver is presented and compared with the performance of PS-SWIPT scheme in section 5.3.

4.3.3 Optimum Receivers

The conventional approach to cope with NLD is to treat it as an undesirable noise term that is added to channel noise (this is the case of the receivers proposed in the previous section). In contrast with this view, it has been shown that the NLD, which is a function of the data signals to be transmitted, has useful information on those signals that can be used to improve the performance, provided that an optimum detection is considered [89]-[90].

The optimum maximum likelihood receiver compares the received signal with all the possible transmitted sequences, which means that its complexity might be too high, even for OFDM signals with a small constellation and a small number of subcarriers [91]. However, recently proposed sub-optimum receivers can approach the optimum performance with acceptable complexity [92]-[93].

For Gaussian signals submitted to bandpass nonlinearities, it was shown that the potential asymptotic gain of ML receivers relative to linear transmissions is dependent on the squared Euclidean distance (SED) between two nonlinearly distorted signals [90, 94]. The term "asymptotic gain"is related to two approximations since: (i) the gain is calculated for signals with a large number of subcarriers (N); and (ii) the gain is calculated for the high SNR regime. The approximation (i) is explained by the fact that the SED is a random variable, whose variance reduces when N increases. Here, it should be noted that the "random"nature of the SED is related to the fact that it depends on the "original"signal and on the error position. The approximation (ii) means that the most likely error events are the ones associated with transmitted sequences differing in one bit. Under these circumstances, the pairwise error probability (PEP) associated with one-bit error events dominates the BER. Studies using the PEP for obtaining the approximate BER performance of nonlinear OFDM have shown that with ML receivers the performance of nonlinear transmitters can outperform conventional receivers with linear OFDM [90]. As it was shown in the previous sections, the nonlinear distortion levels for FS-SWIPT OFDM signals are much higher than the ones associated with corresponding non-SWIPT OFDM schemes, which motivates the study of ML receivers for nonlinear FS-SWIPT OFDM schemes.

Let us define the time-domain FS-SWIPT OFDM signal[3] as $x = x_e + x_d$ and its 1-bit variation as $x' = x + \varepsilon$. The geometric representation of these signals is depicted in Fig. 4.9. By denoting the nonlinearity function as $f(\cdot)$, the SED can be computed as

$$D^2 = \|f(x) - f(x')\|^2 = \|f(x) - f(x+\varepsilon)\|^2. \tag{4.24}$$

Moreover, by taking advantage of a Taylor approximation of $f(x)$ (which is valid for

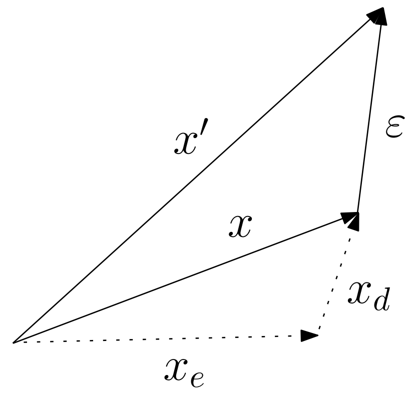

Figure 4.9: Geometric representation of the OFDM signal and its 1-bit variation.

reasonably smooth nonlinear characteristics), we can write

$$f(x+\varepsilon) \approx f(x) + f'(x_n)\varepsilon, \tag{4.25}$$

where $f'(\cdot)$ is the first-order derivative of the nonlinear function $f(\cdot)$. Under these conditions,

$$D^2 \approx \|f'(x_n)\varepsilon\|^2. \tag{4.26}$$

The resulting potential asymptotic gain over linear transmissions is

$$G = \frac{D^2}{4E_b}, \tag{4.27}$$

where E_b denotes the average bit energy. In [94], it was shown that the average value of SED for nonlinearly distorted Gaussian signals can be computed theoretically as

$$\mathbb{E}[D^2] = 4\int_0^{+\infty} \left(f_a'^2(r) + \frac{f_a^2(r)}{r^2} + f_p'^2(r) f_a^2(r) \right) p(r)\,dr, \tag{4.28}$$

with r denoting a random variable that models the absolute value of the Gaussian signal, $p(r)$ being the distribution of r (given by (4.7)) and $f_a'(r)$ representing the first-order derivative of $f_a(r)$.

Fig. 4.10 shows the average SED and the average potential asymptotic gain of FS-SWIPT OFDM signals submitted to a soft envelope limiter (SEL) (which is equivalent to

[3]For the sake of notation simplicity we drop the time index n.

an HPA with the AM/AM function represented in (4.9) particularized for the case where $q \to \infty$) with normalized clipping level s_M/σ_x, considering $N = 512$ subcarriers, $M = 4$ and different values of β and ζ. From this figure, it can be observed that (4.28) presents a high degree of accuracy for modeling the SED (and the optimum asymptotic gain) of FS-SWIPT OFDM signals submitted to bandpass nonlinearities. As expected, the SED decreases when the normalized clipping level decreases. However, since the power of the signal at the nonlinearity's output decreases with s_M/σ_x with a faster rate, the asymptotic gain increases when we decrease s_M/σ_x. The behavior is similar to the one observed for conventional OFDM: larger nonlinear distortion effects lead to higher gains. In fact, we can have gains close to 1.8 (around 2.5 dB) for $s_M/\sigma_x = 0.5$, although the gains decrease with β. In this sense, nonlinear FS-SWIPT OFDM is different from nonlinear OFDM, since larger values of β mean larger NLD levels at the data subcarriers. This is due to the fact that when we increase β, the part of the NLD that is a function of the data symbols decreases.

By considering (4.27), we can write the approximate optimum performance as [94]

$$P_b = \int_0^\infty Q\left(\sqrt{G\frac{2E_b}{N_0}}\right) p(G)\, dG, \tag{4.29}$$

where $p(G)$ is the distribution of the asymptotic gain. In additive white Gaussian noise (AWGN) channels, $p(G)$ tends to a unique value (i.e., the variance of $p(G)$ is very low), provided that N is large. As can be observed in Fig. 4.10, if the transmission is linear we have $G = 1$ and no performance gains exist. In that scenario, ML receivers present exactly the same performance as conventional receivers for OFDM and $P_b = Q\left(\sqrt{\frac{2E_b}{N_0}}\right)$. For frequency-selective channels, the SED between two nonlinear distorted signals can also be used to estimate the optimum asymptotic performance [94]. By denoting the original FS-SWIPT signal as $\{Z_k^{(1)} = \alpha X_k^{(1)} + D_k^{(1)}; k = 0, 1, \cdots, N' - 1\}$ and its 1-bit variation as $\{Z_k^{(2)} = \alpha X_k^{(2)} + D_k^{(2)}; k = 0, 1, \cdots, N' - 1\}$, and taking into account (4.13), the asymptotic gain can be computed as

$$\begin{aligned} G &\triangleq G_{\{X_k^{(1)}\}\to\{X_k^{(2)}\}} \\ &= \frac{\sum_{k=1}^{N'} |H_k|^2 \left(\alpha\left(X_k^{(2)} - X_k^{(1)}\right) + \left(D_k^{(2)} - D_k^{(1)}\right)\right)}{4E_b}, \end{aligned} \tag{4.30}$$

where $X_k^{(1)}$ and $X_k^{(2)}$ are the original (i.e., non-distorted) OFDM symbols associated with $Z_k^{(1)}$ and $Z_k^{(2)}$, respectively. It should be noted that in a linear transmission scenario, $G = |H_k|^2$ and (4.29) reduces to the conventional performance of OFDM systems in fading channels. However, in the presence of nonlinear distortion effects, (4.30) can be seen as an equivalent fading factor that has an inherent diversity effect, since it is not only conditioned to the fading factor associated with a given subcarrier $|H_k|^2$.

Fig. 4.11 shows the distribution of $p(G)$ considering frequency-selective channels with $L = 32$ uncorrelated multipath components. The FS-SWIPT signals have $\zeta = 1/4$

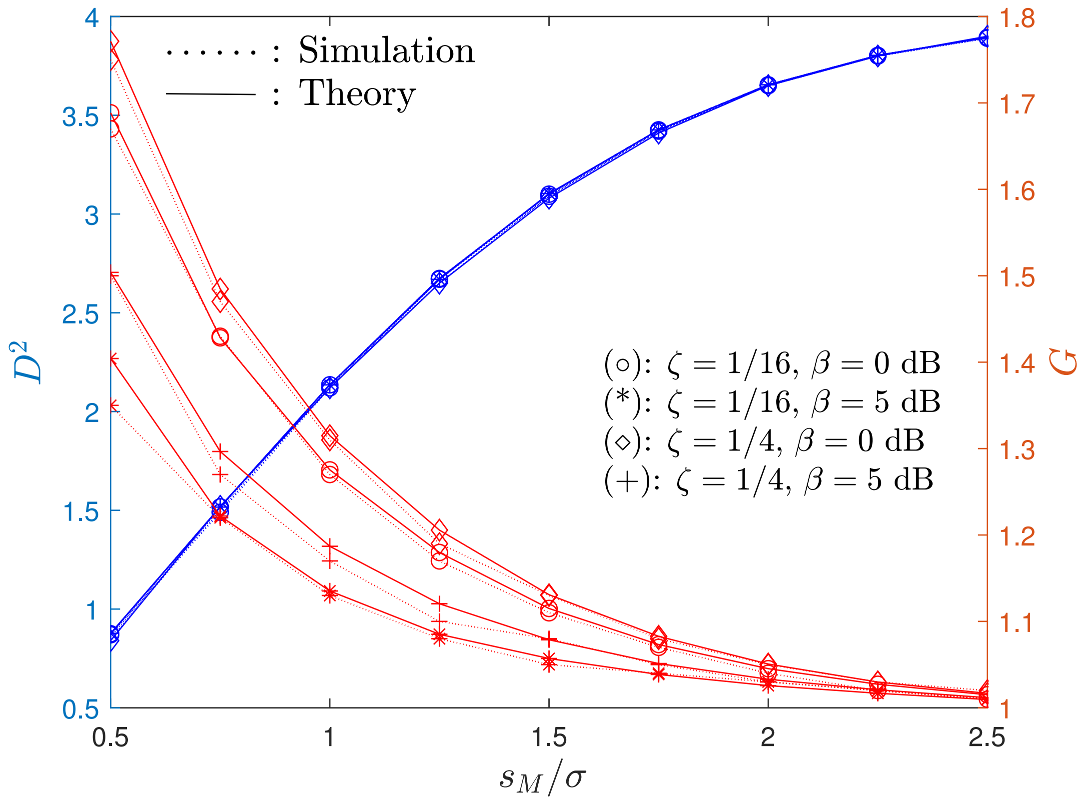

Figure 4.10: Simulated and theoretical average SED and potential asymptotic gain of FS-SWIPT OFDM signals submitted to an envelope clipping considering different values of β.

and $\beta = 0$ dB. The distribution of the fading factor $|H_k|^2$ is also shown for comparison purposes. As can be noted from the figure, in the presence of nonlinear distortion effects, the distribution of the equivalent fading factor assumes higher values than $p(|H_k|^2)$, which leads to performance gains. On the other hand, when the transmission is linear, $p(G) = p(|H_k|^2)$ and no gains are observed.

4.4 Performance Results

This section is dedicated for the performance analysis of the proposed receivers in Section 4.3. In all performance results, the FS-SWIPT signals have $N' = 2048$ and $N = 512$, i.e., an implicit oversampling of $M = 4$ is adopted. We consider a multipath Rayleigh fading channel with $L = 32$ independent rays. In the following figures, the conventional non-SWIPT OFDM with NLD is simply denoted as "non-SWIPT"and the conventional linear OFDM is simply denoted as "linear OFDM".

Let us start by analyzing the performance of the iterative receiver considering $i = 4$ iterations (the additional gains observed after $i = 4$ are negligible). Fig. 4.12 considers the simulated BER considering $\beta = 0$ dB, different normalized clipping levels, and different

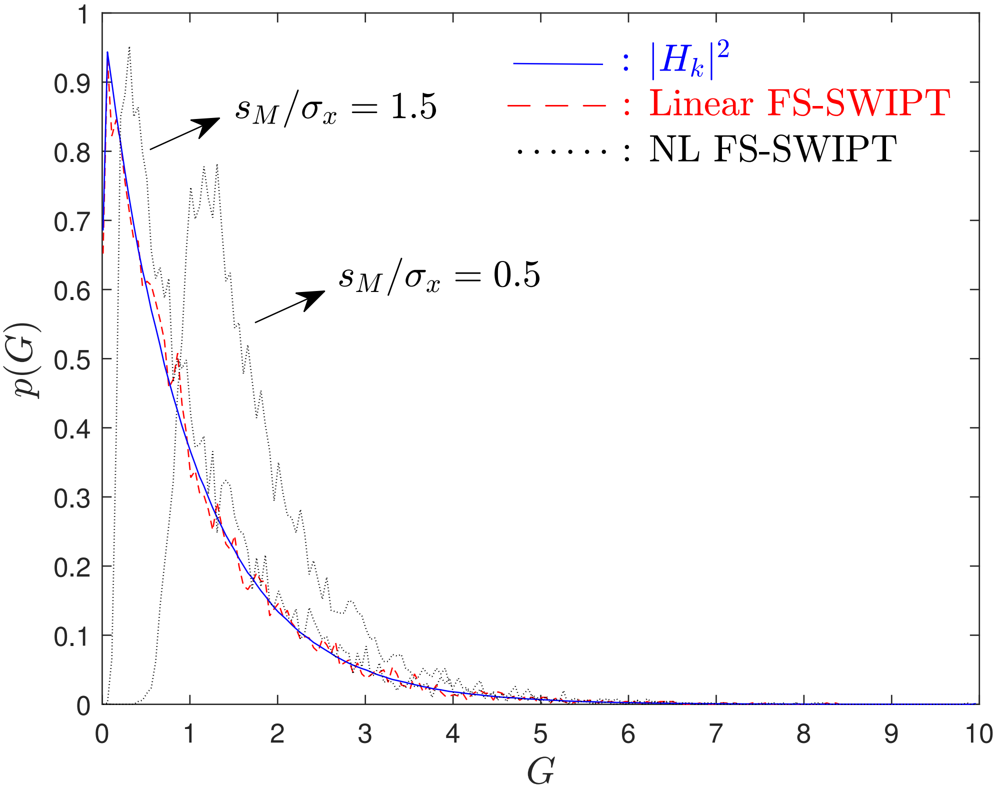

Figure 4.11: Distribution of the optimum asymptotic gain in frequency-selective channels.

values of ζ. Clearly, we are able to approach linear performance almost in all cases. The only exception is when $s_M/\sigma_x = 1.0$ and $\zeta = 1/32$, which corresponds to extremely high nonlinear distortion levels, especially for the subcarriers close to the EH region.

Regardless of the value of ζ, when $s_M/\sigma_x = 2.0$, the receiver usually approaches the linear performance. Therefore, for the following figures, the normalized clipping level is fixed at $s_M/\sigma_x = 1.5$, which corresponds to a moderate NLD level.

To understand the performance of the proposed receiver for different FS-SWIPT configurations, let us consider the evolution of Ψ defined by (4.23), which is shown in Fig. 4.13. As expected, in the first iteration the estimates of the transmitted block are less accurate since NLD is not removed. However, even for $E_b/N_0 = 1$ dB, we have $\Psi > 0.55$, i.e., the data estimates already have some accuracy. As E_b/N_0 increases, the reliability of the estimates improves, but it saturates due to errors driven by the NLD term. As we increase the number of iterations, the data estimates become more reliable, with Ψ increasing, as well as the corresponding saturation level. After a few iterations, we start having very reliable estimates, with Ψ reaching values close to 1. For instance, when $\beta = 15$ dB and $\zeta = 1/8, 1/32$, this happens for an E_b/N_0 of approximately 13 dB. This indicates that the proposed iterative receiver can substantially reduce the NLD levels.

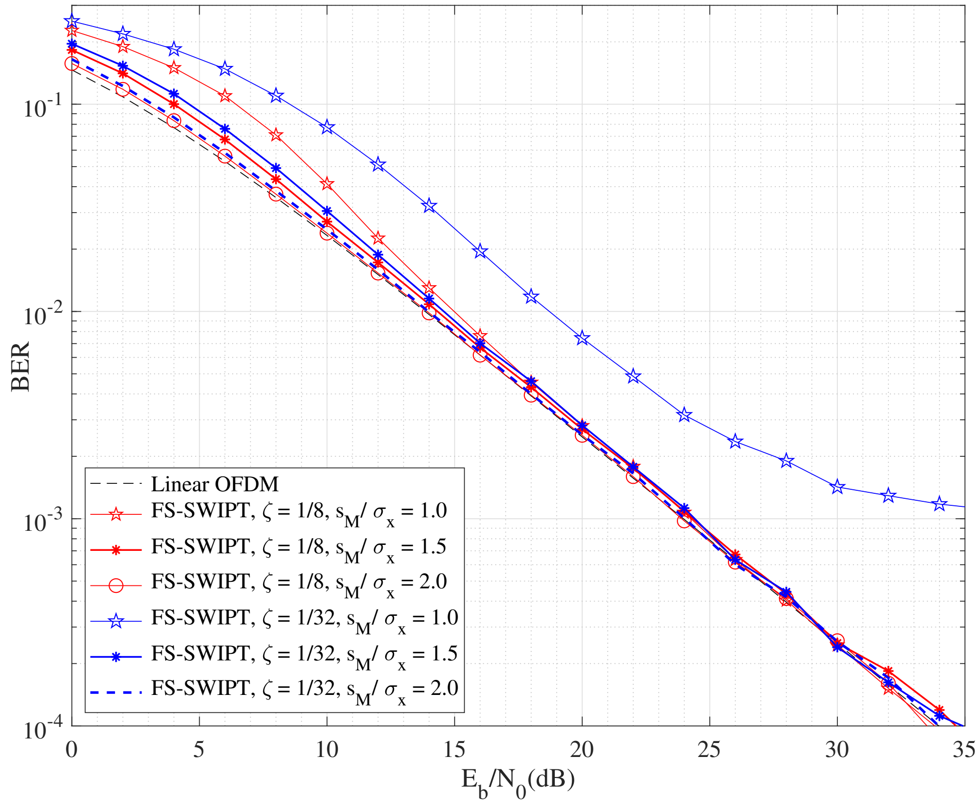

Figure 4.12: BER performance of the proposed iterative Bussgang receiver considering different FS-SWIPT signals, different normalized clipping levels and $\beta = 0$ dB.

Fig. 4.14 presents the BER performance for different FS-SWIPT schemes, as well as an OFDM-based PS-SWIPT scheme with the same nonlinear characteristic and employing a conventional Bussgang receiver (which, essentially, corresponds to a conventional OFDM signal with nonlinear transmitter and a Bussgang receiver). For a fair comparison, we assumed that PS-SWIPT and FS-SWIPT have the same normalized saturation level s_M/σ_x, which means that the total NLD levels will be identical. Further, the power used for information symbols in FS-SWIPT is equal to the power allocated for the information part of the PS-SWIPT and therefore, both schemes harvest the equal amount of energy. From these figures, we can make two main observations:

Firstly, for FS-SWIPT, BER improves substantially with each iteration, approaching the non-SWIPT OFDM linear performance. Also, the better BER performance of $\zeta = 1/8$ over $\zeta = 1/32$ indicates that the higher N_e (when $\zeta = 1/8$) leads to better NLD compensation in the iterative loop (i.e. (4.21) and (4.22)), which is in conformance with the Ψ performance shown in Fig. 4.13.

Secondly, when we compare FS-SWIPT with PS-SWIPT at the first iteration (i.e., conventional Bussgang receiver) PS-SWIPT outperforms FS-SWIPT, which is mainly due to the higher NLD levels of the subcarriers close to the EH region in the FS-SWIPT as shown in Fig. 4.6, which does not happen in PS-SWIPT, where the NLD is spread throughout the

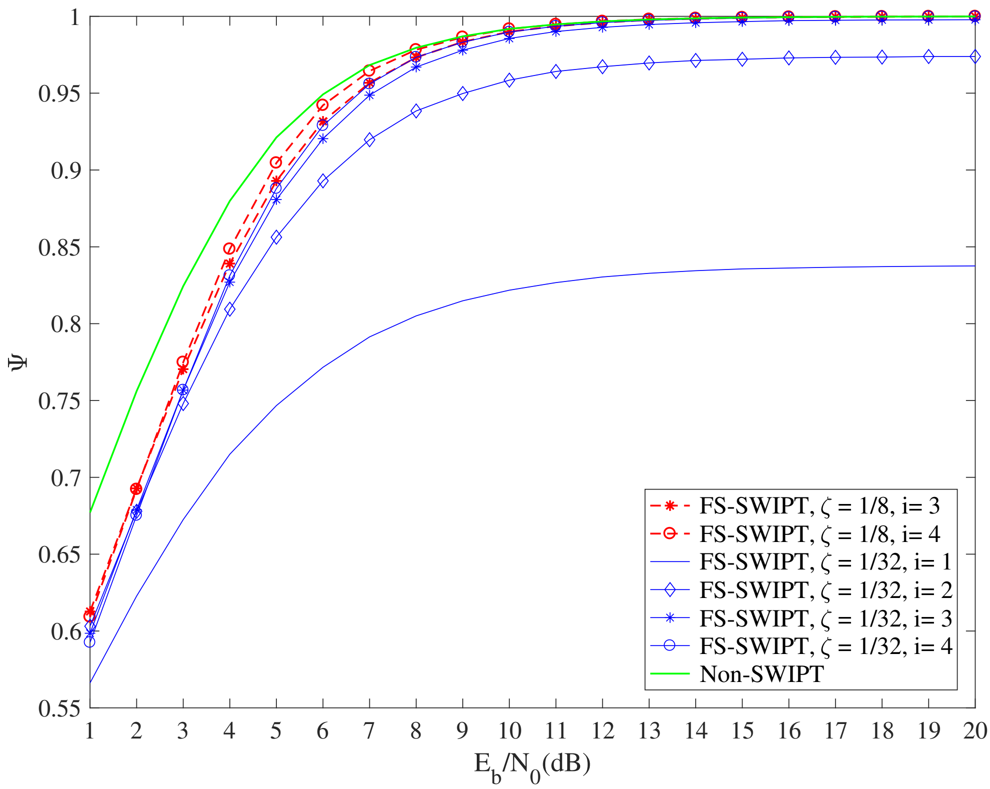

Figure 4.13: Evolution of Ψ based on the iterative function of the receiver with the normalized clipping level $s_M/\sigma_x = 1.5$, where $\beta = 15$ dB.

subcarriers instead of being concentrated in a particular spectrum region. However, after a few iterations, due to the use of known EH symbols of FS-SWIPT in (4.22), FS-SWIPT slightly outperforms PS-SWIPT with a performance gain of approximately 1 dB gain. In fact, at high SNR, the BER of FS-SWIPT ($\zeta = 1/8$) is almost equal to the linear case, which means that FS-SWIPT schemes are more robust against NLD.

Let us now consider the optimum detection of nonlinearly distorted FS-SWIPT. Fig. 4.15 presents the asymptotic BER for optimum receivers using (4.29).

From the figure, it can be observed that the optimum performance of the nonlinear FS-SWIPT OFDM signal is much better than the linear performance, with larger gains for smaller values of the normalized clipping level s_M/σ_x as is expected from Fig. 4.11. Although the gains are smaller for larger values of β (i.e., for stronger EH terms), there is always a diversity effect that is exploited by the optimum receiver, with the approximate BER dropping at a rate much higher than in the linear case.

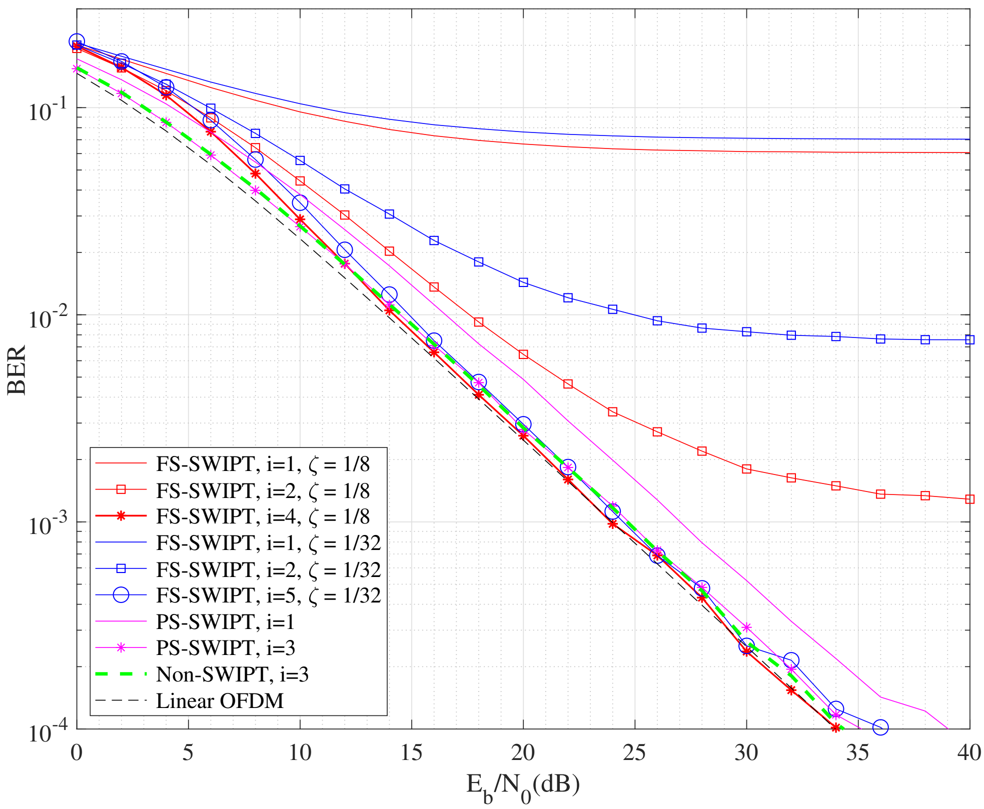

Figure 4.14: BER performance of the proposed iterative receiver for FS-SWIPT and PS-SWIPT schemes, both with the same nonlinear characteristics.

4.5 Conclusions

In this chapter, we considered an FS-SWIPT scheme combined with OFDM modulations for both energy harvesting and data transmission. We presented an analytical characterization of the transmitted signal and showed that FS-SWIPT OFDM signals are much more prone to nonlinear distortion than non-SWIPT schemes, especially when the EH term has much larger power than the data transmission term. However, we can overcome this degradation by employing receivers that estimate and remove the nonlinear distortion term in an iterative way, with small error propagation effects. Moreover, the performance of the proposed iterative receiver is shown to be more robust to NLD in FS-SWIPT OFDM than in PS-SWIPT OFDM. We also studied the optimum performance of nonlinear FS-SWIPT OFDM schemes and showed that it can be better than the linear performance, with gains that can be particularly high in frequency-selective channels (due to an inherent diversity effect that is created in the transmitted signals by the nonlinear device). The gains are higher for more severe nonlinear characteristics but decrease with the increase in the power of the EH term.

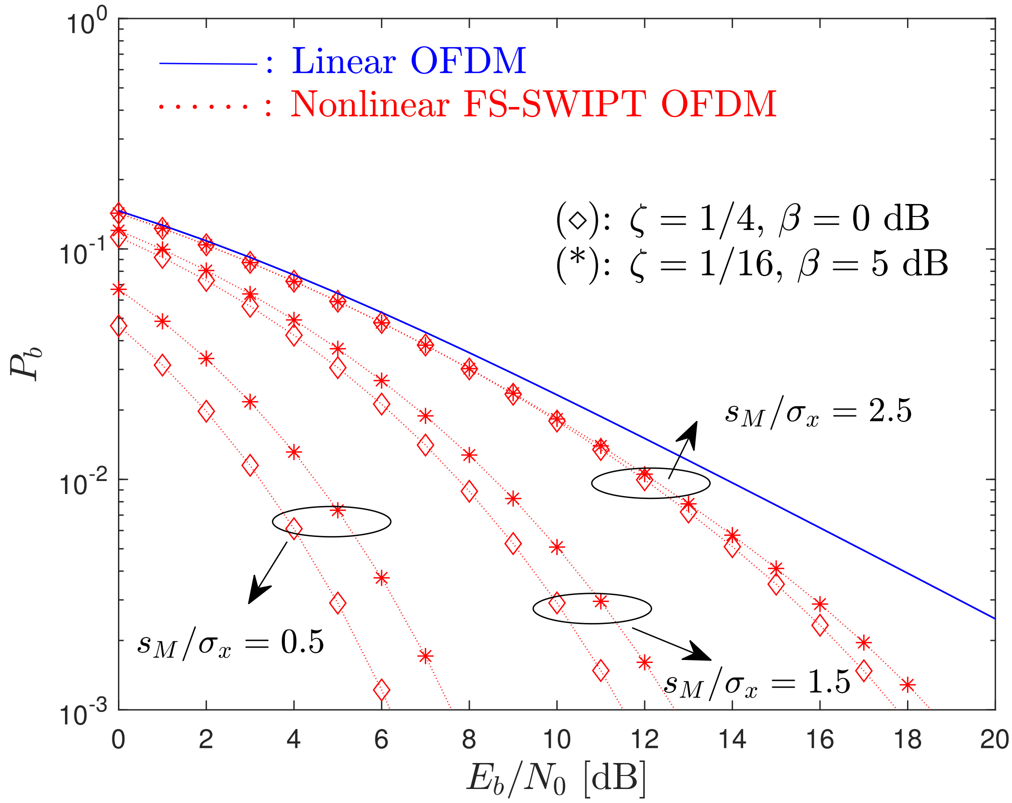

Figure 4.15: Asymptotic optimum performance of nonlinear FS-SWIPT OFDM schemes in frequency-selective channels.

5

Simultaneous wireless information and power transmission with joint CFO and channel estimation

In this chapter, we adopt a channel estimation technique with SWIPT and then optimise minimum power required for pilot signal and information to get better error rate performance. We use single-carrier SC-FDMA, which has several advantages over Orthogonal frequency-division multiple access (OFDMA) as mentioned in [95]. But it also has a main disadvantage as compared to OFDMA i.e. occurrence of CFO during signal transmission. SC-FDMA is sensitive to CFO as compared to OFDMA [95]. CFO often occurs when the local oscillator signal for down conversion in the receiver does not synchronize with the carrier signal contained in the received signal [96], [97], and due to Doppler shift, and the compensation techniques are studied in [98]. Thus, it is important to study CFO effects and the compensation technique for the SC-FDMA signal. Frequency errors due to CFO directly affect the performance of channel estimation and signal detection [99], [100]. There are many CFO estimation techniques proposed for OFDM schemes in [44]-[101]. Maximum likelihood frequency offset estimation technique was proposed in [44] and this method is suitable for small CFO, because it compares two consecutive and identical symbols with the symbol duration T_s and the frequency acquisition range is $\pm 1/(2T)$. To improve the acquisition range for the CFO, two separate pilot signals were employed in [102]. Based on [102], an algorithm called best linear unbiased estimator is proposed in [101] to improve the acquisition range.

To improve information decoding accuracy at receiver, an efficient iterative FDE for SC-FDE is introduced [24]. It is called as IB-DFE and this technique performs better than non-iterative methods [24]. Recently, an iterative linear minimum mean-square-error was proposed to estimate the individual channels used in multiple input and multiple antenna systems [103]. Thus, the iterative block based receiver structure is a predominantly researched area, especially the IB-DFE receiver. By using an IB-DFE receiver, the channel estimation is performed with the help of a pilot signal as in [104]. Since the optimum FDE coefficients are a function of the channel frequency response, channel estimates are required at the receiver.

In this chapter, we use Moose technique, assuming that the frequency acquisition range is within $\pm 1/(2T)$ and the CFO is small. Also we have the idea of using SWIPT in the point to point communication model of 5G networks and it is applicable to both the uplink and downlink. The 5G network uses both the single carrier modulation and the multi carrier modulation. The single carrier for uplink and multi carrier modulation for downlink as it proved to be the best choice [22]. The SC-FDMA with FDE is found to be suitable for the transmission of high data rate signals over severely time dispersive channels.

The channel estimates are obtained by using pilot symbols, which are either in time or frequency domain [43]. Most commonly, frequency domain is used for OFDM modulations while both time and frequency domain is used for SC modulations. In block transmission techniques, the channel impulse response may be very long and the record overheads for channel estimation is possibly very high. As a solution, the pilot symbols are superimposed with the information symbols, instead of multiplexing the pilot symbols with the information symbols. This increases the density of pilots with respect to information symbols without comprising spectral efficiency. This helps in improving the amount of EH. The disadvantages of using a superimposed pilot signal, is the interference of pilot signal with the information signal with increase in transmit power of pilot signal. Then, the interference of the pilot signal with the information signal can be reduced by averaging the channel estimate of the respective frequency. The proposed technique helps in estimating CFO as shown in [44] by using the highly energized identical pilot signal sequence on each block. Thereby with the help of SWIPT, pilot signals will be more robust for signal interference and noise.

The SWIPT improves the performance of the iterative receiver by allowing IB-DFE in exploiting the excessive power that was originally intended for EH, to estimate channel. This, recursively, can be used in the iterative receiver to decode. This reduces the nonlinear distortion effects and minimize the estimation overheads [105]. The effective use of SWIPT with IB-DFE not only increases the spectral efficiency, but also reduces the signal interference and helps in signal detection.

The contribution of this chapter:

- We design a receiver for SWIPT with joint CFO and channel estimation. The pilot symbols, which are superimposed, with the information symbols are used for EH, CFO and channel estimation. Here, the overall transmit power of the pilot signal is higher than that of other competitive models such as techniques which employ multiplexing pilot symbols with the information symbols.

- We improve the channel estimation accuracy with the help of IB-DFE and an algorithm is introduced with IB-DFE to increase the accuracy of the channel estimation with the estimated feedback in IB-DFE.

- We find the minimum power required for the pilot signal to estimate the channel condition and CFO with achievable accuracy for the given power of the information signal. Also, we find the optimum power allocation ratio between the information and the pilot signals by using simulation results.

The structure of the chapter as follows. The system model is explained in Sec. 5.1. The proposed channel estimation technique and signal detection is explained in Sec. 5.2. The performance results are analyzed in in sec. 5.3 and the conclusion is presented in sec. 5.4.

5.1 System Model

The system uses Quadrature phase shift keying (QPSK) modulation with SC-FDE over the Rayleigh fast fading channel. The receiver estimates the channel and information using an iterative receiver. The system harvests energy from the received signal as shown in Fig. 5.1. It is assumed that the system experiences AWGN with variance $N_0/2$ is modelled as zero mean complex Gaussian random variable and undergoes phase rotation. The system adopts a power splitting protocol based SWIPT (PS-SWIPT). The receiver is fitted with a special circuit at the antenna to split the total power of the signal for information decoding and energy harvesting [2]. The frame structure of the signal is presented in Fig. 5.2, where time duration per symbol, block duration and total time for all the blocks are denoted as T_s, T_l and $T_l L$, respectively. Frame structure is similar to the frame structure used in [106], where the pilot and the information signals are superimposed together as a single signal. The frame structure of the signal has a L number of signal blocks with each signal block has a N number of symbols. The signal blocks are denoted as l, where $l \in \{0, 1, ..., L\}$ and the symbol is denoted as n, where $n \in \{0, 1, ..., N-1\}$. The received signal $'Y_l'$ can be expressed as

$$Y_l = H_l(\sqrt{P_x} X_l + \sqrt{P_q} Q_l) + W_l, \quad l \in \{0, 1, ..., L-1\}, \tag{5.1}$$

where H_l is Rayleigh fading channel gain, X_l and Q_l are the information signal and pilot signal with the transmit power P_q and P_x, respectively. W_l is the corresponding AWGN noise.

The power allocation ratio for the ID and EH by using PS-SWIPT circuit are ζ_P and $(1-\zeta_P)$, respectively, where $0 < \zeta_P < 1$. The received signal obtained from the PS-SWIPT circuit for ID and EH are denoted as $Y_{l,i}$ and $Y_{l,e}$, respectively. Thus we have

$$\begin{aligned} Y_{l,i} &= \zeta_P\Big(H_l(\sqrt{P_x} X_l + \sqrt{P_q} Q_l) + W_l\Big) + W_e, \\ Y_{l,e} &= (1-\zeta_P)\Big(H_l(\sqrt{P_x} X_l + \sqrt{P_q} Q_l) + W_l\Big) + W_e, \end{aligned} \tag{5.2}$$

where W_e is the new AWGN noise that occurred due to the signal splitting by power splitter circuit at the receiver [2].

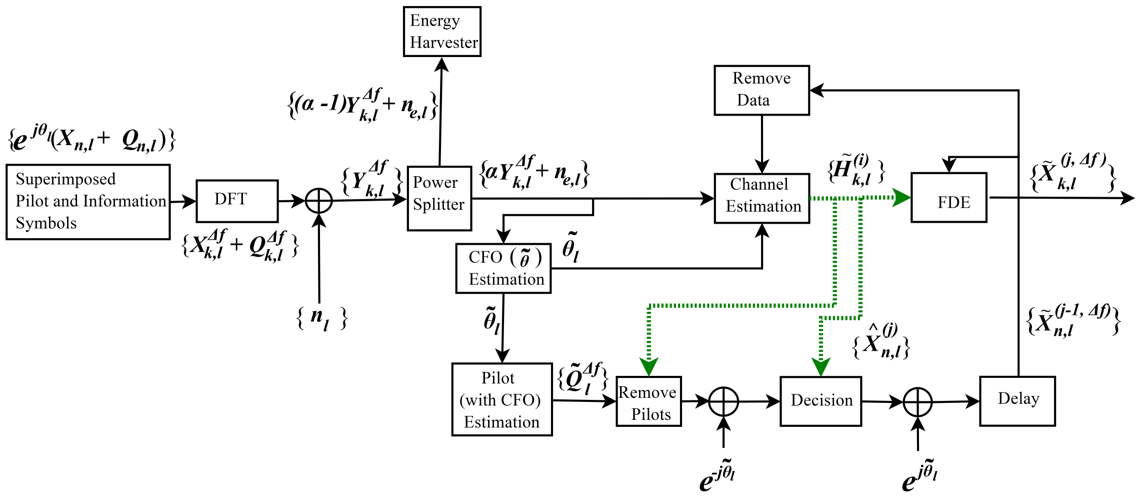

Figure 5.1: Receiver Design for SWIPT with Joint CFO and Channel Estimation.

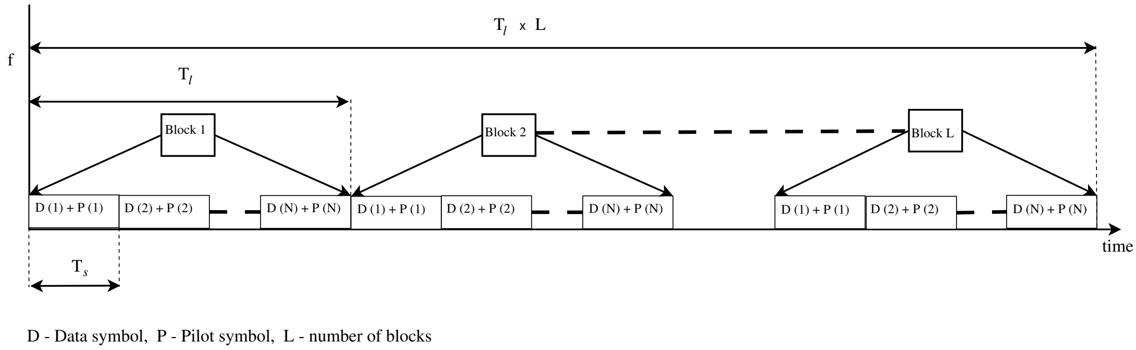

Figure 5.2: Frame structure of the proposed system, where T_s and T_l are the time duration of a symbol and a block, respectively.

The energy harvested at the receiver from the signal $Y_{l,e}$ is denoted as $\mathfrak{E}_{PS}$, which is expressed as

$$\mathfrak{E}_{PS} = \frac{\eta_{eh}(1-\zeta_P)(P_x+P_q)|h_l|T_l}{d^{\varkappa}} \tag{5.3}$$

where η_{eh} is the rectenna conversion efficiency and P is the power of the received signal. $|h_l|$ is the channel power gain, d is the distance between the transmitter and the receiver, and $\varkappa$ is the path loss factor.

The signal transmission for l^{th} block in time domain of SC-FDE modulation with appropriate phase rotation is written as

$$x_l^{T_s x}(t_i) = \sum_{n=-Ns}^{N-1} x_{n,l}^{T_s x} \exp(j\theta_n) r(t_i - nT_s), \tag{5.4}$$

where $r(.)$ and Ns are the pulse shaping filter function and the cyclic prefix, respectively. $x_l^{T_s x}(t_i)$ is the samples with time domain symbols n, $n \in \{0,1,...,N-1\}$ transmitted over a time-dispersive channel. The phase rotation of each symbol present in the l is denoted as θ_n and $\theta_n = 2\pi\Delta f T_l \frac{n}{N}$, where the CFO is denoted as Δf and it is assumed that Δf is constant for all the blocks. The information signal is superimposed with the pilot signal, thus we have

$$x_{n,l}^{T_s x} = \exp(j\theta_n)\{\sqrt{P_x}x_{n,l} + \sqrt{P_q}q_{n,l}\}, \tag{5.5}$$

where n is the number of blocks symbols present in each time blocks l, with $n = 0, 1, ..., N-1$ and $l = 0, 1, ..., L-1$. Since the symbols are superimposed, θ_n affects both $x_{n,l}$ and $q_{n,l}$. Then, the superimposed time domain signal is converted to frequency domain of SC-FDE as

$$X_{k,l}^{T_s x} = X_{k,l}^{(\Delta f)} + Q_{k,l}^{(\Delta f)}, \tag{5.6}$$

where k is the frequency of block l, $k = 0, 1, ..., K-1$ and $l = 0, 1, ..., L-1$. $X_{k,l}^{(\Delta f)} = DFT\{x_{n,l}\exp(j\theta_n); n = 0, 1, ..., N-1\}$ and $Q_{k,l}^{(\Delta f)} = DFT\{q_{n,l}\exp(j\theta_n); n = 0, 1, ..., N-1\}$. $X_{k,l}^{(\Delta f)}$ and $Y_{k,l,i}^{(\Delta f)}$ are the information and pilot signals converted from time to frequency domain, respectively.

By using (5.6) in (5.2), we get the received signal $Y_{k,l,i}^{(\Delta f)}$ used for information decoding purpose as

$$Y_{k,l,i}^{(\Delta f)} = \zeta_P\Big(H_{k,l}(\sqrt{P_x}X_{k,l}^{(\Delta f)} + \sqrt{P_q}Q_{k,l}^{(\Delta f)}) + W_l\Big) + W_{e,l}, \tag{5.7}$$

where $H_{k,l}$ is Rayleigh fast fading channel.

5.2 Joint CFO and Channel Estimation with IB-DFE

In this section, the joint CFO and channel estimation along with signal detection by using an iterative receiver based on the IB-DFE concept is presented as shown in Fig. 5.1. CFO and channel estimation comprise three steps as follows:

A Computes the average CFO estimate by using $Y_{k,l,i}^{(\Delta f)}$ and the CFO estimate is denoted as $\Delta\tilde{f}$. Estimate pilot signal with phase rotation by using $\Delta\tilde{f}$. The estimate of pilot signal with phase rotation is denoted as $\tilde{Q}_{k,l}^{(\Delta f)}$ and it should be used for channel estimation due to phase rotation on $Q_{k,l}$.

B To compute the average channel estimate $\tilde{H}_{k,l}^{av}$ over a set of blocks without using an iterative receiver and analyze conditions involved to estimate the channel condition.

C To compute the information estimate $\tilde{X}_{k,l}^{(j,\Delta f)}$ and new channel estimates $\tilde{H}_{k,l}^{(j)}$ by using an iterative receiver. In each iteration the new information estimate and channel estimate are found by using their previous value and received signals. The final information estimate found by repeating the same iterative blocks for an optimum number of times is denoted as $\tilde{X}_{k,l,F}^{(j,\Delta f)}$.

The above three steps are explained in the following subsections.

5.2.1 Carrier Frequency Offset Estimation

CFO is estimated by calculating phase rotation over a set of received signal blocks with help of pilot signal. CFO is estimated by using Moose technique [44, p. 21] on the received signal. The CFO estimate of each block is written as

$$\Delta\tilde{f}_l = \frac{1}{2\pi T_l} \arg\left\{ \sum_{n=0}^{N-1} y_{n,l,i}^{(\Delta f)} {y_{n,(l+1),i}^{(\Delta f)}}^* \right\}, \tag{5.8}$$

where $Y_{k,l,i}^{(\Delta f)} = \text{DFT}\,\{\exp(j\theta_n)\tilde{y}_{n,l,i}; n = 0,1,...,N-1\}$ and $Y_{k,(l+1),i}^{(\Delta f)} = \text{DFT}\,\{\exp(j\theta_n)\tilde{y}_{n,(l+1),i}; n = 0,1,...,N-1\}$. The mean CFO estimate of all the blocks is written as

$$\Delta\tilde{f} = \frac{1}{L-1}\left\{ \sum_{l=0}^{L-2} \Delta\tilde{f}_l \right\}, \tag{5.9}$$

where the phase rotation estimate is written as $\exp(j\tilde{\theta}_n) = 2\pi\Delta\tilde{f}\,T_l\frac{n}{N}$

The expected value of $H_{k,l}$, W_l, W_e, $X_{k,l}^{(\Delta f)}$ and $Q_{k,l}^{(\Delta f)}$, respectively is written as

$$\begin{aligned}
&\mathbb{E}[H_{k,l}] = 2\sigma_{h,k,l}^2 = 1,\ \mathbb{E}[W_l] = 2\sigma_{w,l}^2,\ \mathbb{E}[W_{e,l}] = 2\sigma_{w,e}^2,\\
&\mathbb{E}[X_{k,l}] = \mathbb{E}[X_{k,l}^{(\Delta f)}] = N\mathbb{E}[{x_{n,l}}^2] = 2\sigma_{x,n,l}^2,\\
&\mathbb{E}[Q_{k,l}] = \mathbb{E}[Q_{k,l}^{(\Delta f)}] = N\mathbb{E}[{q_{n,l}}^2] = 2\sigma_{q,n,l}^2,
\end{aligned} \tag{5.10}$$

where $\mathbb{E}[X_{k,l}] = \mathbb{E}[X_{k,l}^{(\Delta f)}]$ and $\mathbb{E}[Q_{k,l}] = \mathbb{E}[Q_{k,l}^{(\Delta f)}]$ because there is no change in variance with or without phase rotation. The expected values in (5.10) are used to analyze (5.8). To find CFO estimation from (5.8) and (5.9), the received signal should satisfy three conditions, they are:

1 At the transmitter, the pilot symbols present in each block should be same, i.e. $Q_{k,l} = Q_{k,0} = Q_{k,1} ... = Q_{k,L-1}$. With this condition, ideally by considering only the pilot signal (without noise and information signal), the angle between subsequent pilot blocks should give the perfect phase rotation estimate between the subsequent pilot blocks.

2 Since the CFO is constant for each symbol in the block, the phase rotation is linear and the angle between summation of all the symbols in l^{th} block and $(l+1)^{th}$ block, respectively, should give the mean phase rotation of l^{th} block.

3 At receiver, converting the received signal of l blocks from frequency to time domain, we get $\exp(j\theta_n)$ of l blocks. It is written as: $y_{k,l}^{(\Delta f)} = \text{DFT}\,\{\exp(j\theta_n)\tilde{y}_{n,l}; n = 0,1,...,N-1\}$. If $\sigma_{q,n,l}^2 > \{\sigma_{x,n,l}^2 + \sigma_{w,l}^2 + \sigma_{w,e}^2\}$ then, $\exp(j\theta_n)$ of $\tilde{Y}_{n,l}$ is approximately equal to $\exp(j\theta_n)$ of $q_{n,l}$. This means, if the signal strength of pilot signal is greater than information signal combined with noise in all the blocks, then $\Delta\tilde{f}$ is estimated using (5.8) and (5.9).

Due to phase rotation in the received signal, the pilot signal transmitted at the source is not used for channel estimation. Thereby, $\tilde{\theta}_n$ is used to find the pilot signal with phase rotation and it is written as

$$\tilde{Q}_{k,l}^{(\Delta f)} = \mathrm{DFT}\{\exp(j\tilde{\theta}_n)Q_{n,l}\}\,, \tag{5.11}$$

where $n = 0,1,...,N-1$ and $l = 0,1,...,L-1$. The estimated value of $\tilde{Q}_{k,l}^{(\Delta f)}$ is written as $\mathbb{E}[\tilde{Q}_{k,l}^{(\Delta f)}] = N\mathbb{E}[{q_{n,l}}^2] = 2\sigma_{q,n,l}^2$.

5.2.2 Channel Estimation

The channel is estimated using the received signal and the pilot signal estimate, is written as

$$\begin{aligned}
\tilde{H}_{k,l} &= \frac{Y_{k,l,i}^{(\Delta f)}}{P_q\tilde{Q}_{k,l}^{(\Delta f)}} \\
&= \zeta_P\left(\frac{H_{k,l}\sqrt{P_x}X_{k,l}^{(\Delta f)} + W_l}{\sqrt{P_q}\tilde{Q}_{k,l}^{(\Delta f)}}\right) + \zeta_P H_{k,l} + \frac{W_{e,l}}{P_q\tilde{Q}_{k,l}^{(\Delta f)}} \\
&= \zeta_P H_{k,l} + \varepsilon_{H\,k,l}.
\end{aligned} \tag{5.12}$$

The channel estimate $\tilde{H}_{k,l}$ can be improved by converting $\{\tilde{H}_{k,l}; k = 0,1,...,K-1\} =$ DFT $\{\tilde{h}_{n,l}g_n; n = 0,1,...,N-1\}$ if n_{th} time domain is inside the cycle prefix, then g_n is either 1 or 0. After forcing zeros to the time domain samples which are not inside the cycle prefix, again the time domain channel estimate is converted back to frequency domain $\{\tilde{h}_{n,l}; n = 0,1,...,N-1\} =$ IDFT $\{\tilde{H}_{k,l}g_n; k = 0,1,...,K-1\}$. The channel estimate error is written as

$$\varepsilon_{H\,k,l} = \zeta_P\left(\frac{H_{k,l}\sqrt{P_x}X_{k,l}^{(\Delta f)} + W_l}{\sqrt{P_q}\tilde{Q}_{k,l}^{(\Delta f)}}\right) + \frac{W_{e,l}}{P_q\tilde{Q}_{k,l}^{(\Delta f)}}, \tag{5.13}$$

where $\varepsilon_{H\,k,l}$ denotes the channel estimation error, where $\varepsilon_{H\,k,l}$ depends on the P_x, noise, P_q and pilot signal.

The frame structure is similar to [106], where each frame has N subcarriers per block. The data $X_{k,l}^{(\Delta f)}$ and the pilot signal $\tilde{Q}_{k,l}^{(\Delta f)}$ are in frequency domain and they have equal number of subcarriers. In order to reduce the envelope fluctuations of the transmitted signal, the pilot signal in the time domain should be constant. Then $\tilde{Q}_{k,l}^{(\Delta f)}$ and $\tilde{Q}_{n,l}$ are constants by using Chu sequence as in [104]. By using (5.10) in (5.13) gives

$$\mathbb{E}[\varepsilon_{H\,k,l}] = \zeta_P\left(\frac{\sigma_{h,k,l}^2\sigma_{x,n,l}^2 + \sigma_{w,l}^2}{\sigma_{\tilde{Q},n,l}^2}\right) + \frac{\sigma_{w,e}^2}{\sigma_{\tilde{Q},n,l}^2}. \tag{5.14}$$

The channel fades with the change in frequency, but remains constant for the respective frequency of a set of transmitted signals. Then based on this assumption, averaging the channel estimation reduces the error and then (5.14) can be is written as

$$\varepsilon_{H\,k,l}^{av} = \frac{1}{l}\sum_{l=0}^{L-1}\Big(\mathbb{E}[\varepsilon_{H\,k,l}]\Big), \quad l = 0,1,...,L-1, \tag{5.15}$$

$$\tilde{H}_{k,l}^{av} = \zeta_P(H_{k,l} + \varepsilon_{H_{k,l}^{av}}), \tag{5.16}$$

where the average of channel estimation error and channel estimation over l blocks are denoted as $\varepsilon_{H_{k,l}^{av}}$ and $\tilde{H}_{k,l}^{av}$, respectively.

Thus, the information estimated by using the received signal, pilot signal and the channel estimate $\tilde{H}_{k,l}^{av}$ is written as

$$\begin{aligned}\tilde{X}_{k,l}^{(z,\Delta f)} &= \frac{Y_{k,l,i}^{(\Delta f)}}{\tilde{H}_{k,l}^{av}} - \zeta_P\sqrt{P_q}\tilde{Q}_{k,l}^{(\Delta f)} \\ &= \frac{\zeta_P\Big(H_{k,l}(\sqrt{P_x}X_{k,l}^{(\Delta f)} + \sqrt{P_q}\tilde{Q}_{k,l}^{(\Delta f)}) + W_l\Big) + W_{e,l}}{\zeta_P(H_{k,l} + \varepsilon_{H_{k,l}^{av}})} \\ &\quad - \zeta_P\sqrt{P_q}\tilde{Q}_{k,l}^{(\Delta f)},\end{aligned} \tag{5.17}$$

where $\tilde{X}_{k,l}^{(z,\Delta f)}$ is the information estimate computed by using Zero forcing (ZF) decoder. The expected value of information estimate error is calculated by using mean square error (MSE) and it is written as

$$\mathbb{E}[\varepsilon_{X_{k,l}^{(j,\Delta f)}}] = \frac{1}{n^2}\frac{1}{l}\sum_{k=0}^{K-1}\sum_{l=0}^{L-1}\mathbb{E}[|X_{k,l}^{(\Delta f)} - \tilde{X}_{k,l}^{(z,\Delta f)}|^2]. \tag{5.18}$$

From the (5.14) and (5.17), we can infer the following two conditions for successful channel estimation and information decoding:

1 if $\sigma_{q,n,l}^2 > \sigma_{x,n,l}^2$, then interference from the information symbol would be lesser on the channel estimates.

2 if $\sigma_{x,n,l}^2 > \sigma_{w,l}^2$, then interference from the channel noise would be lesser on the channel estimates and also on the information estimates.

Based on the above conditions, $\frac{\sigma_{Q,n,l}^2}{\sigma_{x,n,l}^2}$ and $\frac{\sigma_{x,n,l}^2}{\sigma_{w,l}^2}$ are denoted as β_Q and β_X. The value of β_Q and β_X are used in Sec. 5.3 to find the optimum error rate performance.

5.2.3 Channel Estimation and Information Detection with IB-DFE

We employ an iterative receiver to improve the accuracy of the information estimates. This process is explained below

$$\tilde{X}_{k,l}^{(j,\Delta f)} = (Y_{k,l,i}^{(\Delta f)} - \zeta_P\sqrt{P_q}Q_{k,l}^{(\Delta f)}\tilde{H}_{k,l}^{(j)})F_{k,l}^{(j)} - \tilde{X}_{k,l}^{(j-1,\Delta f)}B_{k,l}^{(j)}, \tag{5.19}$$

where $\tilde{X}_{k,l}^{(j-1,\Delta f)}$ is the previous iteration value of $\tilde{X}_{k,l}^{(j,\Delta f)}$ and j is the number of iteration followed in IB-DFE receiver and, $j = 0, 1, ..., J$. In the first iteration, the channel estimate obtained from (5.16) is used to estimate information in the IB-DFE receiver, then $\tilde{H}_{k,l}^{(0)} = \tilde{H}_{k,l}^{av}$. $F_{k,l}^{(j)}$ is the feed forward coefficient and it is written as

$$F_{k,l}^{(j)} = \frac{\tilde{F_{k,l}^{(j)}}}{\frac{1}{K}\sum_{k=0}^{K-1}\left(\tilde{F_{k,l}^{(j)}}\tilde{H}_{k,l}^{(j)}\right)}, \tag{5.20}$$

where $\tilde{F}_{k,l}^{(j)}$ is written as

$$\tilde{F}_{k,l}^{(j)} = \frac{\tilde{H}_{k,l}^{(j)*}}{\left(\frac{\sigma_{n,k,l}^2}{\sigma_{x,n,l}^2}\right) + |\tilde{H}_{k,l}^{(j)}|^2\left(1 - (\rho^{(j-1)})^2\right)}, \tag{5.21}$$

and the correlation factor $\rho^{(j-1)} = \frac{\mathbb{E}[\hat{X}_{n,l}^{(j)} X_{n,l}^*]}{\mathbb{E}[|X_{n,l}^2|]}$. The feedback co-efficient $B_{k,l}^{(j)}$ is written as

$$B_{k,l}^{(j)} = F_{k,l}^{(j)} \tilde{H}_{k,l}^{(j)} - 1. \tag{5.22}$$

The channel estimates can be further refined by using information estimates obtained from the iterative receiver. The expected value of information estimate error is calculated by using MSE is written as

$$\mathbb{E}[\varepsilon_{X_{k,l}^{(j,\Delta f)}}] = \frac{1}{n^2}\frac{1}{l}\sum_{k=0}^{K-1}\sum_{l=0}^{L-1}\mathbb{E}[|X_{k,l}^{(\Delta f)} - \tilde{X}_{k,l}^{(j,\Delta f)}|^2]. \tag{5.23}$$

By using $\tilde{X}_{k,l}^{(j,\Delta f)}$ and $Q_{k,l}^{(\Delta f)}$ in (5.12), the new channel estimates can be written as

$$\begin{aligned}\tilde{H}_{k,l}^{(j)} = \zeta_P\Bigg(&\frac{H_{k,l}(\sqrt{P_x}\tilde{X}_{k,l}^{(j,\Delta f)} + \sqrt{P_q}\tilde{Q}_{k,l}^{(\Delta f)}) + W_l}{\sqrt{P_x}\tilde{X}_{k,l}^{(j,\Delta f)} + \sqrt{P_q}\tilde{Q}_{k,l}^{(\Delta f)}}\Bigg) \\ &+ \frac{W_{e,l}}{\sqrt{P_x}\tilde{X}_{k,l}^{(j,\Delta f)} + \sqrt{P_q}\tilde{Q}_{k,l}^{(\Delta f)}}.\end{aligned} \tag{5.24}$$

There are two channel estimates that are obtained from this receiver:

1 The channel estimation value obtained without using iterative receiver, i.e. (5.16).

2 The channel estimation value obtained from the iterative receiver, i.e. (5.24), this channel estimate improves with each IB-DFE iteration.

Applying (5.24) instead of (5.16) in (5.19) gives improved information estimates than the previous estimates, which is denoted as

$$\tilde{X}_{k,l,F}^{(j,\Delta f)}. \tag{5.25}$$

The expected value of information estimate error of $\tilde{X}_{k,l,F}^{(j,\Delta f)}$ is calculated by using MSE is written as

$$\mathbb{E}[\varepsilon_{X_{k,l,F}^{(j,\Delta f)}}] = \frac{1}{n^2}\frac{1}{l}\sum_{k=0}^{K-1}\sum_{l=0}^{L-1}\mathbb{E}[|X_{k,l}^{(\Delta f)} - \tilde{X}_{k,l,F}^{(j,\Delta f)}|^2]. \tag{5.26}$$

There are three information estimates obtained from this receiver:

1 The information estimation value obtained by using average channel estimate (5.16) without the help of iterative receiver, i.e., (5.17).

2 The information estimation value obtained by using average channel estimate (5.16) and also using iterative receiver, i.e., (5.19).

3 The information estimation value obtained by using improved channel estimate obtained with the help of iterative receiver, i.e., (5.24) and also by using iterative receiver, i.e., $\tilde{X}_{k,l,F}^{(j,\Delta f)}$[1] as in (5.25).

The extrinsic information of $\tilde{X}_{k,l,F}^{(j,\Delta f)}$ and $\tilde{X}_{k,l}^{(z,\Delta f)}$ are calculated by compensating the phase rotation on the estimated symbols present in $\tilde{X}_{k,l,F}^{(j,\Delta f)}$ and $\tilde{X}_{k,l}^{(z,\Delta f)}$, respectively. Converting $\tilde{X}_{k,l,F}^{(j,\Delta f)}$ and $\tilde{X}_{k,l}^{(z,\Delta f)}$ to time domain gives $\exp(j\tilde{\theta}_n)\{\tilde{X}_{n,l,F}^{(j)}\} = \text{IDFT}\{\tilde{X}_{k,l,F}^{(j,\Delta f)}; k = 0,1,...,K-1\}$, and $\exp(j\tilde{\theta}_n)\{\tilde{X}_{n,l}^{(z)}\} = \text{IDFT}\{\tilde{X}_{k,l}^{(z)}; k = 0,1,...,K-1\}$, respectively, where $n = 0,1,...,N-1$ and $l = 0,1,...,L-1$. Then, the extrinsic information of $\tilde{X}_{k,l,F}^{(j,\Delta f)}$ and $\tilde{X}_{k,l}^{(z,\Delta f)}$ respectively, are written as

$$\begin{aligned} \widehat{X}_{n,l,F}^{(j)} &= \exp(j\theta_n)\exp(-j\tilde{\theta}_n)\{\tilde{X}_{n,l,F}^{(j)}\}, \\ \widehat{X}_{n,l}^{(z)} &= \exp(j\theta_n)\exp(-j\tilde{\theta}_n)\{\tilde{X}_{n,l}^{(z)}\}, \end{aligned} \tag{5.27}$$

where $n = 0,1,...,N-1$ and $l = 0,1,...,L-1$.

5.3 Numerical results

In this section, we discuss the simulation setup and demonstrate the performance of the channel estimation method using IB-DFE receiver and SWIPT protocol. The bit error rate (BER) performance of the system is calculated by averaging BER of 1000 signal blocks, where $N = 256$ and $T_l = 1$ second. We assume $\eta_{EH} = 0.9$, path loss factor is 2 and $\Delta f = 0.2$ with distance $d = 3$ m. The value of ζ_P is kept as 0.7, thus 70% of total transmit power is allocated for EH and 30% of power is allocated for ID. The power of superimposed signal is denoted as P_{si} and it is calculated as $P_{si} = 10^{\frac{P_x}{10}} + 10^{\frac{P_q}{10}}$. By using (5.2) and (5.3), the energy harvested from the received signal can be calculated. The CFO estimation error is denoted as $\varepsilon_{\Delta f}$, where $\varepsilon_{\Delta f} = \frac{|\Delta\tilde{f} - \Delta f|}{\Delta f}$. This section has 2 subsections and the subsections are explained as follows:

A Performance Analysis of CFO Estimation - in this section, the results of $\varepsilon_{\Delta f}$ based on Δf, L and P_q are listed in Tab. 5.1 and Tab. 5.2. Further the effect of $\varepsilon_{\Delta f}$ on the channel estimation and information decoding based on L and P_q is demonstrated in Fig. 5.3 and Fig. 5.4, respectively.

B Performance Analysis of Channel Estimation - in this section, the signal is considered to have no CFO (i.e. $\Delta f = 0$) to study the impact of channel estimation. The channel and estimation error based on the P_q are demonstrated in Fig. 5.5. BER performance of the signal based on L and P_q is demonstrated in Fig. 5.7 and Fig. 5.6, respectively. In Fig. 5.8, BER performance improvement due to IB-DFE is

[1] Where F in the subscript denotes the final IB-DFE iteration.

demonstrated. Further, Tab. 5.3 illustrates the result of EH at receiver and Fig. 5.9 demonstrates the optimum β_Q value for the received signal depending on the noise power at the receiver.

5.3.1 Performance Analysis of CFO Estimation

Table 5.1: CFO estimate error ($\varepsilon_{\Delta f}$) based on L blocks are used for the estimation

Δf \ L	2	3	5	7	9	10
0.10	0.0351	0.0067	0.0055	0.0045	0.0049	0.0035
0.15	0.0679	0.0126	0.0042	0.0053	0.0051	0.0043
0.20	0.0571	0.0081	0.0062	0.0047	0.0053	0.0038

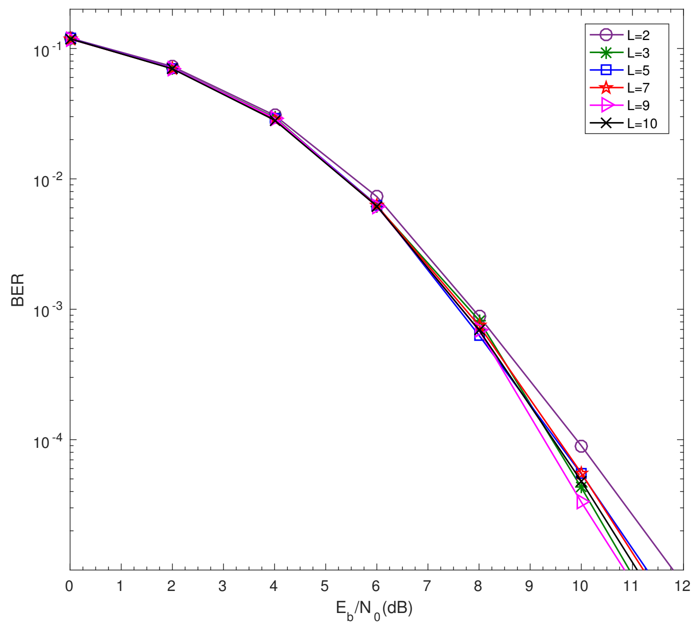

Figure 5.3: Comparison of BER performance of system with CFO based on L blocks used for CFO estimation with constant P_q and P_x.

The performance of the CFO estimation method based on the number of blocks used in the signal to find $\Delta\tilde{f}$ is demonstrated in Tab. 5.1 and Fig. 5.3.

In Tab. 5.1, $\varepsilon_{\Delta f}$ of the received signal is measured for various blocks with P_x and P_q are constant at 21 dBm and 25 dBm, respectively. The results show that at $\Delta f = 0.1$, $\varepsilon_{\Delta f}$ of the received signal with $\Delta f = 0.1$ has significant change between $L = 2$ to $L = 3$, but from $L = 3$ to $L = 10$, the changes are not significant and does not increase or decrease consistently. Similarly, the received signal with $\Delta f = 0.15$ and $\Delta f = 0.2$ has characteristics as $\Delta f = 0.1$. Therefore, it is better to fix $L = 3$ to improve estimation and keep the signal transmission more practical.

In Fig. 5.3, BER performance of the received signal is demonstrated with CFO estimation along with the channel and information estimation by using IB-DFE as in (5.24) and (5.25), respectively. P_x and P_q are constant at 21 dBm and 25 dBm, respectively and $\Delta f = 0.2$. The comparison of the signal with $L = 2$ over the signal with $L = 3$, illustrates that the BER improves significantly for the signal with $L = 3$ (i.e. SNR from 12 dB to 11 dB). But comparing the signal with $L = 3$ over the signal with $L > 3$, the improvement is relatively small by considering L blocks used (i.e. from 11 dB to 10.7 dB) and the relative improvement in BER performance with increase in every single block is inconsistent. The results of Fig. 5.3 is similar to Tab. 5.1 and it implies that the performance of the CFO estimation has a direct effect on channel and information estimation. In Tab. 5.2, $\varepsilon_{\Delta f}$ of

Table 5.2: CFO estimate based on the power of the pilot signal is used for the estimation

Δf \ P_q	17 dBm	19 dBm	21 dBm	23 dBm	25 dBm	27 dBm
0.10	0.0089	0.0084	0.0037	0.0042	0.0016	0.0018
0.15	0.0119	0.0078	0.0031	0.0016	0.0018	0.0014
0.20	0.0153	0.0090	0.0020	0.0018	0.0027	0.0021

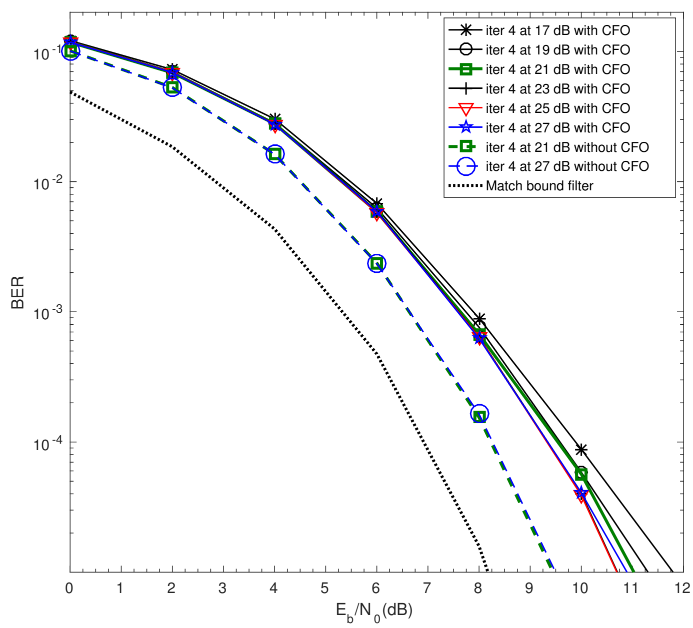

Figure 5.4: Comparison of BER performance of system based on the power of the transmitted signal. Each curve demonstrates system performance based on P_q.

the received signal is measured for various P_q values with P_x is constant at 25 dBm and $L = 3$. The results illustrates that $\varepsilon_{\Delta f}$ of the received signal with $\Delta f = 0.1$ has significant change between $P_q = 17$ to 21 dBm, from $P_q = 21$ to 27 dBm, there are relatively small change and it is inconsistent. Similarly, the received signal with $\Delta f = 0.15$ and $\Delta f = 0.2$ has characteristics as $\Delta f = 0.1$.

In Fig. 5.4, BER performance of the received signal is demonstrated with CFO estimation along with the channel and information estimation by using IB-DFE as in (5.24) and (5.25), respectively. BER is simulated for a signal with $P_q = 14$ to 25 and $P_x = 25$ dBm and $L = 3$ and $\Delta f = 0.2$. Similar to the results in Tab. 5.2, the signal with $P_q = 17$ dBm to 21 dBm has significant change in BER i.e. from 11.8 dB to 11 dB. BER performance for signal with $P_q = 21$ dBm to 25 dBm has only 0.3 dB BER gain i.e. from 11 dB to 10.7 dB.

5.3.2 Performance Analysis of Channel Estimation

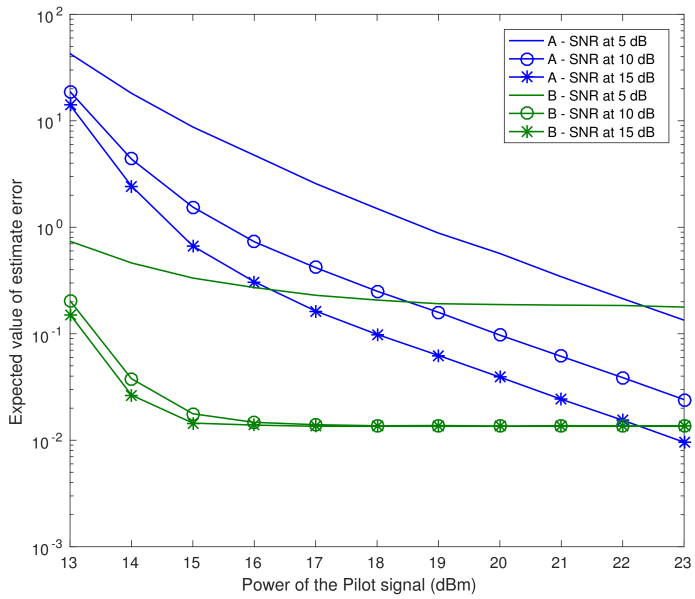

Figure 5.5: The figure demonstrates the results of estimate error versus the P_q at SNR 5 dB, 10 dB and 15 dB, respectively. The expected value of channel estimate error with iterative receiver is denoted as A and the expected value of information estimate error with IB-DFE receiver is denoted as B.

Fig. 5.5 illustrates the optimum power to be used to transmit a pilot signal when the information signal is transmitted at 25 dB and $L = 1$. The figure illustrates that curve A i.e. the expected value of channel estimate error drastically decreases approximately when pilot power is at 15 dBm to 17 dBm. After $P_q = 17$ dBm, the expected value decreases gradually with respect to the increase in P_q. Curve B i.e the expected value of information estimate error decreases with increase in P_q and after $P_q = 17$ dBm, the curve B is showing constant gradient. A and B performance at high SNR is better than at low SNR. When P_x is at 25 dB, the optimum P_q is fixed 17 dBm since the curves of B at 10 dB and 15 dB SNR saturates when P_q is at 17 dBm.

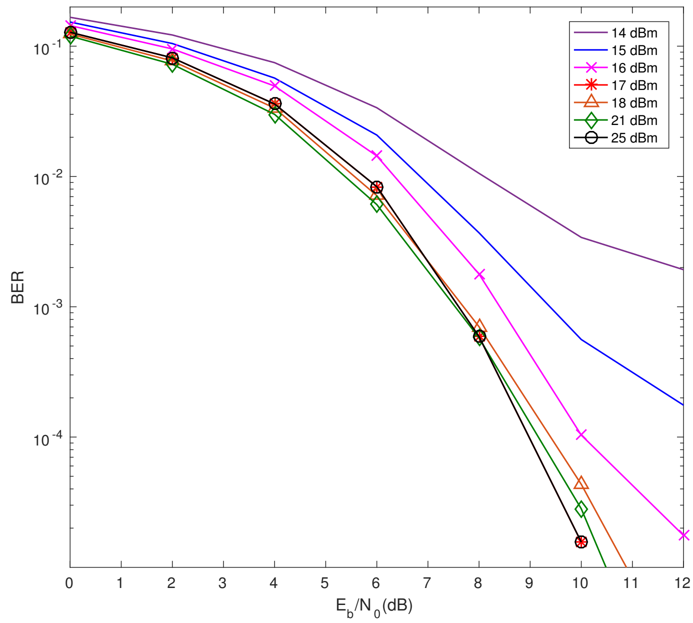

Figure 5.6: Comparison of BER performance of system based on the power of the transmitted signal. Each curve demonstrate system performance based on P_q.

Similar to Fig. 5.5, Fig. 5.6 gives a conclusion based on the BER performance of the system with increase in P_q. P_x is 25 dBm, P_q varies from at 14 dBm to 21 dBm and $L = 1$. The results demonstrate that if P_q is more than 17 dBm, then there is no significant improvement in BER performance. Fig. 5.7 demonstrates that an increase in the number of signal blocks to find the channel estimate average as in (5.16) improves the accuracy of the channel estimate and thereby improves the BER performance of the system. The signal blocks are averaged to improve the channel estimate accuracy by considering an assumption that the channel fading co-efficient is same for all the blocks. The figure also demonstrates that after using 2 slots, the channel estimate saturates to the ideal channel condition. Based on the results, we set $L = 1$ in Fig. 5.5, Fig. 5.6, Fig. 5.8, Fig. 5.9 and Tab. 5.3 to make the simulation more practical.

Fig. 5.8 demonstrates the BER performance of a system based on two different methods to estimate information using an iterative receiver. The curve A denotes the information estimate with the ideal channel condition. The information estimate obtained by using IB-DFE receiver only with information feedback is denoted as B. The information estimate obtained by using IB-DFE receiver with both channel feedback and information feedback is denoted as C. The information estimate found using match bound filter is denoted as D. P_x is 25 dBm, P_q is 21 dBm and $L = 1$. Fig. 5.8 demonstrates the improved BER performance of the system with the IB-DFE receiver using both the channel and information estimate feedback. Due to the usage of both using channel estimate feedback

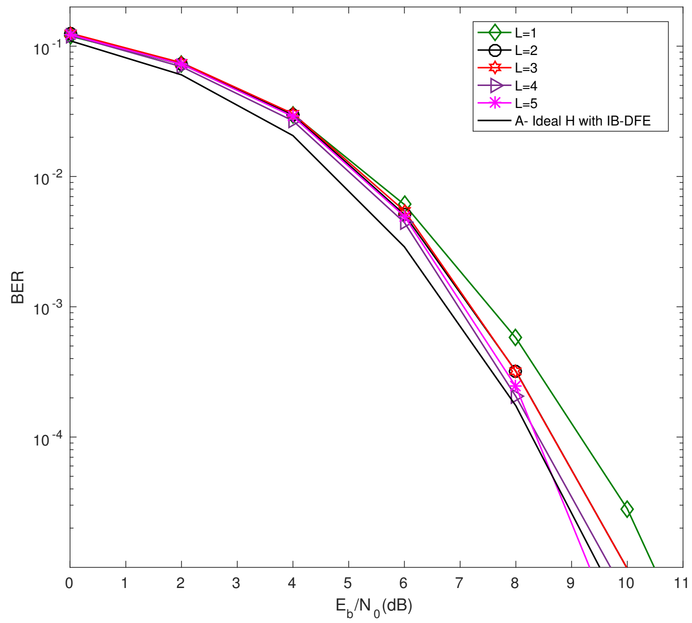

Figure 5.7: Comparison of BER performance of system with iterative receiver based on the number of slots used to average the channel estimates. P_q and P_x is at 21 dBm and 25 dBm, respectively.

Table 5.3: The amount of energy harvested at receiver and the expected value of information estimate error based on the power of pilot signal.

P_q (dBm)	14	15	16	17	18	19	20	21
P_{si} (dBm)	25.332	25.414	25.515	25.639	25.790	25.973	26.193	26.455
EH (mJ)	0.021	0.022	0.022	0.023	0.023	0.024	0.026	0.027
$\mathbb{E}[\varepsilon_{X_{k,l,F}^{(j,\Delta f)}}]$ at 5 dB SNR	0.412	0.276	0.210	0.181	0.159	0.156	0.152	0.141
$\mathbb{E}[\varepsilon_{X_{k,l,F}^{(j,\Delta f)}}]$ at 10 dB SNR	0.036	0.018	0.014	0.014	0.014	0.014	0.014	0.014
$\mathbb{E}[\varepsilon_{X_{k,l,F}^{(j,\Delta f)}}]$ at 15 dB SNR	0.023	0.014	0.013	0.013	0.013	0.013	0.013	0.013

and information estimate feedback recursively in the IB-DFE receiver, the BER performance of the information estimated as $\tilde{X}_{k,l,F}^{(j,\Delta f)}$ is better than the information estimated at (5.19). With each IB-DFE iteration, both the channel and information estimates improve, but this improvement ceases at 3^{rd} iteration compared to 4^{th} iteration. To validate our estimation techniques, the results are compared with the information estimate with the ideal channel and match bound filter.

Tab. 5.3 illustrates the value of P_{si}, E_y and $\mathbb{E}[\varepsilon_{X_{k,l,F}^{(j,\Delta f)}}]$ based on the value of P_q. $P_x = 25$ dBm and P_q varies from 14 dBm to 21 dBm. E_y increases proportionally with increase P_{si}. It is understood that the increase in P_q reduces $\mathbb{E}[\varepsilon_{X_{k,l,F}^{(j,\Delta f)}}]$ up to a certain limit. Since P_q is

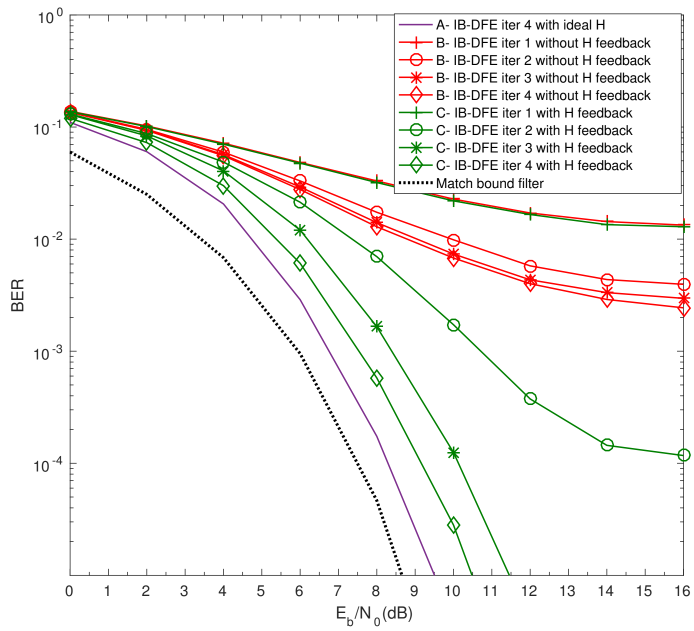

Figure 5.8: Comparison of BER performance of the system based on two different methods to estimate information.

considerably lower than P_x, the percentage of increase in P_q value is higher as compared to percentage of increase in P_{si} value. Thereby, even with a slight increase in P_{si}, it is possible to improve the BER performance drastically. Thus, this scheme is effective even at low SNR region.

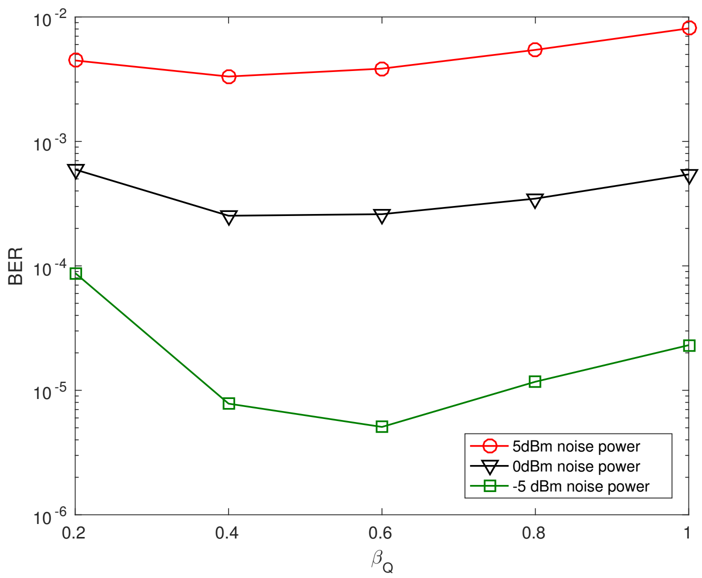

Figure 5.9: BER performance based on the ratio of power between pilot and information in the superimposed signal.

Fig. 5.9 demonstrates the BER performance based on the ratio of power between pilot and information in the superimposed signal and the optimum β_Q value for the received signal depending on the noise power at the receiver. This figure has different simulation setup, where $\Delta f = 0$, $L = 1$, $\varkappa = 2$, $d = 3$ m, $\zeta_P = 0.3$, $P_{si} = 28$ dBm with β_Q is varying from 0.2 to 1. There are three curves in the figure based on the signals with the fixed noise power −5 dBm, 0 dBm and 5 dBm, respectively at the receiver. The results prove that both the conditions $\sigma^2_{q,n,l} > \sigma^2_{x,n,l}$ and $\sigma^2_{x,n,l} > \sigma^2_{w,l}$ are necessary for better BER performance. The system with $\sigma^2_{w,l} = 5$ has better BER performance at $\beta_Q = 0.4$ and the system with $\sigma^2_{w,l} = -5$ has better BER performance at $\beta_Q = 0.6$. The curves explains that with the increase in noise power, the optimum β_Q reduces in order to allocate more power for the information signal and subsequently increasing β_X. Another important observation on β_Q by considering the curve with $\sigma^2_{w,l} = -5$, the BER performance is better only if $\beta_Q = 0.6$ and not less than 0.6, otherwise channel estimation error will increase as compared to channel estimation error at $\beta_Q = 0.6$ and subsequently degrades the BER performance.

5.4 Conclusion

In this work, the simultaneous wireless information and power transmission scheme is employed to harvest energy, and to estimate CFO and channel condition by using the superimposed pilot and information signal. We find the optimum ratio of the power required for the pilot signal and information signal to achieve a desirable error rate performance in respect to varying SNR conditions. Also, an algorithm is implemented at the receiver by using the feedback of the channel and information estimation to improve the performance. The presented analytical results are in line with the numerical results.

6 Secure Information Transmission in a Wiretap Channel

In the dense WCNs, both the energy and security reliability needs to be assured. This represents a challenge in the case of a network with a huge number of nodes [2]. Thus, in order to keep up with the energy demands of the increasing number of network nodes, new radio frequency EH techniques like SWIPT are investigated for 5G networks [2, 4, 107].

In this chapter, we consider the presence of multiple eavesdroppers for the purpose of channel estimation and information estimation, and this leads to wiretap channel system models. Therefore, smart indoor WCN requires energy efficient secure communication and, therefore, green communication technologies, such as WPT, which can be adapted for PLS [3]. High power signals can be used for WPT and other signal processing applications such as channel estimation [45, 107] and as a jamming signal [46, 57].

In a wiretap channel, by using AN, the jammer can degrade the SINR of the eavesdroppers [3]. In general, the secrecy rate of legitimate users in a wiretap channel are improved by degrading SINR eavesdroppers, as in [48, 49], and by employing MIMO system models, as in [50]. Contrary to SINR degradation at eavesdroppers, the jammer avoids SINR degradation at the legitimate receiver by introducing AN in the null space of the legitimate receiver's channel matrix. Therefore, the jammer improves secrecy rate without compromising the quality of the legitimate users' signal [51]. However, this is considered as a challenge in imperfect CSI condition [53]. Eavesdropper can reduce the impact of AN with the knowledge of CSI of the channel between jammer and receiver but, under normal circumstances, it is highly unlikely for the eavesdropper to have the CSI of the receiver to jammer channel link. Therefore, AN can be effectively used against many robust eavesdroppers, as in [52, 108].

In this chapter, we present two wiretap system models. In the first model, we explain a basic wiretap channel model and study the impact of channel estimation errors and an unexpected channel correlation between eavesdropper and legitimate network. In the second system model, we present cooperative eavesdroppers at a wiretap channel, where we provide solutions by optimizing the transmitting power of EH components in SWIPT to improve energy efficiency and to improve the secrecy rate of information components.

6.1 Secure Information Transmission by using Self Jamming SWIPT with IB-DFE receiver

In this section, we use energy signals as a source of AN for secure communication but also to harvest energy at the receiver. We consider a conventional MIMO system model with separate antennas for data and energy signal transmission and reception. AN is created by the transmitter by using channel precoding based on the CSI of the receiver. In this section, we analyse the impact on channel precoding based on imperfect CSI. Furthermore, we also consider high channel correlation between eavesdroppers and the legitimate receiver as one of the challenges in the analysis. Our main contribution in this section involves improving the error rate and secrecy rate performance of the legitimate receiver using IB-DFE. IB-DFE is an efficient low complex receiver and performs better than non-iterative methods [24]. IB-DFE is effectively used with SC-FDMA transmission technique and its performance is studied in detail [109, 110]. IB-DFE can also be used to improve channel estimation at the transmitter side against imperfect CSI by using robust superimposed pilot signal method for accurate channel estimate as in [45, 104]. For a fair comparison between legitimate user and eavesdroppers, we also analyse the impact of imperfect CSI on the legitimate user's performance.

6.1.1 System model

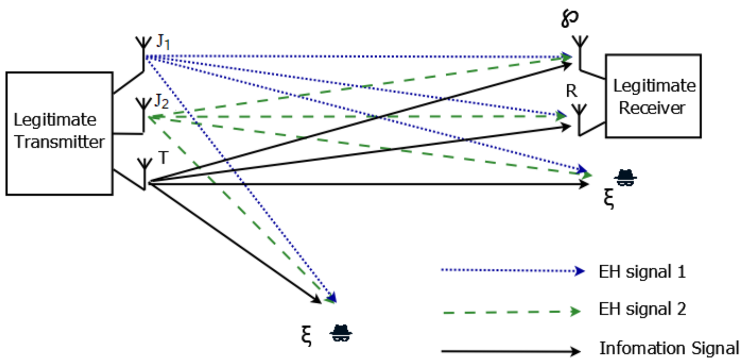

Figure 6.1: System model of Self Jamming SWIPT in a wiretap channel.

The MIMO system model is shown in Figure 6.1. It is composed of 3 transmitting antennas and 2 receiving antennas, with a dedicated transmitting antenna and a receiving antenna for information transmission, denoted as T and R, respectively. Other two transmitting antennas (Jamming antennas), J_1 and J_2, are used for energy transmission and the rectenna $\wp$ is used to harvest energy from the Physical layer network coded (PLNC) signal. The eavesdropper(s) are generally denoted as ξ. It is assumed that J_1, J_2 and T are not spatially correlated. In Figure 6.1, based on the location of ξ, if ξ is very close to R, ξ is considered to have high channel correlation with R [55]. The system adopts Quadrature amplitude modulation (QAM) signal over Rayleigh frequency selective fading channel by using SC-FDMA for simultaneously transfer information from T, and high energy signal from J_1 and J_2 to both R and $\wp$. The frequency domain signals transmitted from T, J_1 and J_2 are denoted as $X_I^{(k)}$, $X_{J_1}^{(k)}$ and $X_{J_2}^{(k)}$, respectively, where k represents the index of the symbol with $k = 0,1,...,K$ and K is the total number of symbols in the respective signal stream. The frame structure of $\mathbf{X}_I$, $\mathbf{X}_{J_1}$ and $\mathbf{X}_{J_2}$ is illustrated in Figure 6.2, where the time duration per symbol, block duration and total time for all the blocks are denoted as T_s, T_l and T_lL, respectively. A frame consists of L signal blocks where each signal block contains N symbols. The signal blocks are denoted as l, where $l = 0,1,...,L$. We assume that $X_I^{(k)}$, $X_{J_1}^{(k)}$ and $X_{J_2}^{(k)}$ are transmitted with perfect time synchronization and in equal block size. The following system equations are considered for a single block and therefore, we set $l = 1$. S_{J_1}, S_{J_2} and S_I are the unamplified version of $\mathbf{X}_{J_1}$, $\mathbf{X}_{J_2}$ and $\mathbf{X}_I$, respectively and the

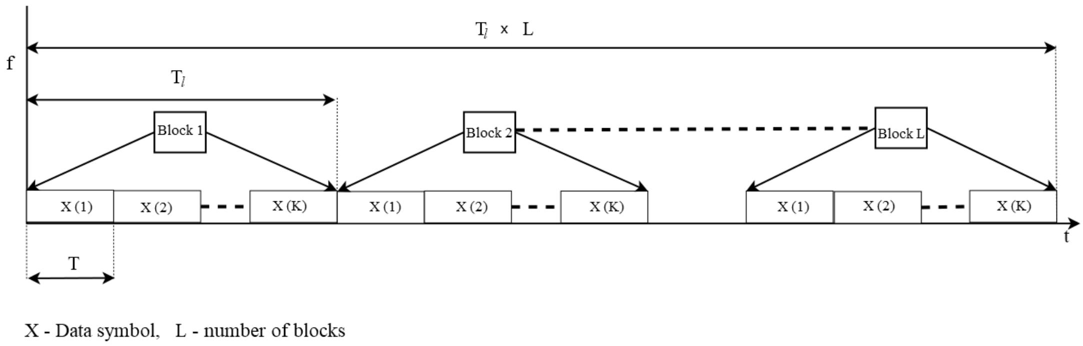

Figure 6.2: Frame structure of the proposed system, where T_s and T_l are the time duration of a symbol and a block, respectively.

power amplification levels of energy symbols and information symbols are at different levels. P_{J_1}, P_{J_2} and P_I denote the transmit powers of $\mathbf{X}_{J_1}$, $\mathbf{X}_{J_2}$ and $\mathbf{X}_I$, respectively. For the sake of simplicity, without loss of generality, we assume that $P_{J_1} = P_{J_2}$. The relationship between the power levels of energy and information symbols is given as

$$\begin{aligned} &X_I^{(k)} = S_I^{(k)} P_I; \;\; X_{J_1}^{(k)} = S_{J_1}^{(k)} P_{J_1}; \;\; X_{J_2}^{(k)} = S_{J_2}^{(k)} P_{J_2}; \\ &\beta = \frac{2P_{J_1}}{P_I}, \end{aligned} \tag{6.1}$$

where β is the ratio between the transmit power of energy and information signal.

Throughout this section, the channel coefficient for the channel link between two nodes i.e. for an example node T and R is denoted as $H_{TR}^{(k)}$, where k represents the index of channel coefficient with respect to the transmitted symbol in the signal stream. Then, $H_{TR}^{(k)}$ is characterised as $H_{TR}^{(k)} \sim \mathscr{CN}(0, \sigma_{H,TR}^2)$ and its channel gain is given as $|(H_{TR}^{(k)})^2| \sim \text{Exp}\{\sigma_{H,TR}^2\}$, where $\sigma_{H,TR}^2$ is the variance of $H_{TR}^{(k)}$. Since all the channel links between the nodes are Rayleigh frequency selective fading channel, they follow similar notation and channel characterisation as like $H_{TR}^{(k)}$. Similarly, the channel coefficients corresponding to the channel link between J_1 and R, J_2 and R, T and $\wp$, J_1 and $\wp$, J_2 and $\wp$, T and ξ, J_1 and ξ, and J_2 and ξ are denoted as $H_{J1R}^{(k)}$, $H_{J2R}^{(k)}$, $H_{T\wp}^{(k)}$, $H_{J1\wp}^{(k)}$, $H_{J2\wp}^{(k)}$, $H_{T\xi}^{(k)}$, $H_{J1\xi}^{(k)}$, and $H_{J2\xi}^{(k)}$, respectively. The received signals at R, $\wp$ and ξ experience AWGN modelled as zero mean complex Gaussian random variable, and their respective AWGNs are given as $N^{(k)} \sim \mathscr{CN}(0,\sigma_N^2)$, $W^{(k)} \sim \mathscr{CN}(0,\sigma_W^2)$, and $J^{(k)} \sim \mathscr{CN}(0,\sigma_J^2)$, respectively.

The system model exploits the CSI of $H_{J2R}^{(k)}$ and $H_{J1R}^{(k)}$, to cancel the interference of the energy signals to the information signal at R. $X_{J_1}^{(k)}$ and $X_{J_2}^{(k)}$ will be precoded to equalize $H_{J2R}^{(k)}$ and $H_{J1R}^{(k)}$, respectively. Unlike R, the eavesdropper ξ, receives a highly distorted signal, which makes the decoding process difficult. In general, ξ can decode the information based on the estimated value of $X_{J_1}^{(k)}$, $X_{J_2}^{(k)}$, $H_{J2R}^{(k)}$ and $H_{J1R}^{(k)}$. Also, to reduce the accuracy of these estimated values at ξ, EH signal should act as AN. Similar to ξ, $\wp$ will receive the combination of all the transmitted signals as a PLNC signal. Furthermore, $\wp$ can effectively take advantage of the PLNC signal for harvesting energy, and the received PLNC signal at $\wp$ is given as

$$Y_{\wp}^{(k)} = H_{J1\wp}^{(k)} X_{J_1}^{(k)} + H_{J2\wp}^{(k)} X_{J_2}^{(k)} + H_{T\wp}^{(k)} X_I^{(k)} + W^{(k)}. \tag{6.2}$$

The performance of this secure self jamming SWIPT technique is analysed based on the secrecy rate and the bit error rate (BER). Here, three different scenarios are considered and in all the scenarios, R and ξ considered to have CSI of $\mathbf{H}_{TR}$ and $\mathbf{H}_{T\xi}$, respectively. Here, both R and ξ do not have CSI of $\mathbf{H}_{J1R}$ and $\mathbf{H}_{J2R}$. The assumptions behind the three scenarios are explained as follows

A scenario **A**: T has the CSI of $\mathbf{H}_{J1R}$ and $\mathbf{H}_{J2R}$. ξ is assumed to be far away from R and ξ does not have channel correlation. In this scenario, ξ is denoted as $\xi(a)$ and R is denoted as $R(a)$.

B scenario **B**: T does not have the CSI of $\mathbf{H}_{J1R}$ and $\mathbf{H}_{J2R}$, and T estimates $\mathbf{H}_{J1R}$ and $\mathbf{H}_{J2R}$. ξ is assumed to be very close to R and their channel correlation is very high. In this scenario, ξ is denoted as $\xi(b)$ and R is denoted as $R(b)$.

C scenario **C**: This scenario is similar to **A** where T has the CSI of $\mathbf{H}_{J1R}$ and $\mathbf{H}_{J2R}$ but here, ξ is assumed to be very close R and their channel correlation is very high. In this scenario, ξ is denoted as $\xi(c)$. Based on perfect CSI condition, R is same in scenario **A** and scenario **C**.

Then, the received signal at $R(a)$ is given as

$$Y_{R(a)}^{(k)} = \begin{cases} H_{TR}^{(k)} X_I^{(k)} + N^{(k)}; & \text{if } \mathscr{L}(\mathscr{V}^{(k)}) = 0, \\ H_{TR}^{(k)} X_I^{(k)} + N^{(k)} + H_{J1R}^{(k)} X_{J_1}^{(k)} + H_{J2R}^{(k)} X_{J_2}^{(k)}; & \text{otherwise}, \end{cases} \tag{6.3}$$

where $\mathscr{L}(.)$ denotes linear subspace of a vector and $\mathscr{V}^{(k)} = H_{J1R}^{(k)} X_{J_1}^{(k)} + H_{J2R}^{(k)} X_{J_2}^{(k)}$. Here, $H_{J1R}^{(k)} X_{J_1}^{(k)}$ is the additive inverse of $H_{J2R}^{(k)} X_{J_2}^{(k)}$, and this allows T to nullify the interference of $X_{J_1}^{(k)}$ and $X_{J_2}^{(k)}$. To achieve $\mathscr{L}(H_{J1R}^{(k)}X_{J_1}^{(k)} + H_{J2R}^{(k)}X_{J_2}^{(k)}) = 0$, both $X_{J_1}^{(k)}$ and $X_{J_2}^{(k)}$ should be precoded based on the CSI of the EH signals; thereby the inference of EH signals to $X_I^{(k)}$ can be reduced to a negligible level as in (6.3). The precoded $X_{J_1}^{(k)}$ and $X_{J_2}^{(k)}$ are given as

$$\begin{aligned} X_{J_1}^{(k)} &= A_{J_1}^{(k)} H_{J2R}^{(k)}, \\ X_{J_2}^{(k)} &= A_{J_2}^{(k)} H_{J1R}^{(k)}, \end{aligned} \tag{6.4}$$

where $A_{J_1}^{(k)}$ and $A_{J_2}^{(k)}$ are the k^{th} entry of the precoding vectors $\mathbf{A}_{J_1}$ and $\mathbf{A}_{J_2}$, respectively. The precoding vectors are chosen such that, under any SINR condition $\mathscr{L}(H_{J1R}^{(k)}X_{J_1}^{(k)} + H_{J2R}^{(k)}X_{J_2}^{(k)}) = 0$.

Therefore, due to precoding, the SINR of $\mathbf{Y}_{R(a)}$ at $R(a)$ does not experience any interference from EH signals, which is given as

$$\gamma_{R(a)} = \frac{\mathbb{E}[|\mathbf{X}_I^T \mathbf{H}_{TR}|^2]}{\mathbb{E}[||\mathbf{N}||^2]} = \frac{\sigma_{X,I}^2 \sigma_{H,TR}^2}{\sigma_N^2}, \tag{6.5}$$

where $\mathbb{E}[|\mathbf{X}_I|^2] = \sigma_{X,I}^2$. Thus, under the perfect channel condition, the EH signal does not affect the performance of the legitimate receiver R.

Irrespective of its location, ξ receives the signal with low SINR due to the EH signal interference. The received signal at $\xi(a)$ is given as

$$Y_\xi^{(k)}(a) = H_{T\xi}^{(k)} X_I^{(k)} + H_{J1\xi}^{(k)} X_{J_1}^{(k)} + H_{J2\xi}^{(k)} X_{J_2}^{(k)} + J^{(k)}, \tag{6.6}$$

where $Y_\xi^{(k)}(a)$ is PLNC signal and $H_{T\xi}^{(k)}X_I^{(k)}$ is the useful information component and the EH signal components ($H_{J1\xi}^{(k)}X_{J_1}^{(k)}$ and $H_{J2\xi}^{(k)}X_{J_2}^{(k)}$) are considered as an interference to $X_I^{(k)}$. Hence, the SINR of $\mathbf{Y}_\xi(a)$ at $\xi(a)$ is given as

$$\gamma_{\xi(a)} = \frac{\mathbb{E}[|\mathbf{X}_I^T \mathbf{H}_{T\xi}|^2]}{\mathbb{E}[|\mathbf{X}_{J_1}^T \mathbf{H}_{J1\xi}|^2] + \mathbb{E}[|\mathbf{X}_{J_2}^T \mathbf{H}_{J2\xi}|^2] + \mathbb{E}[||\mathbf{J}||^2]} = \frac{\sigma_{X,I}^2 \sigma_{H,T\xi}^2}{\sigma_{H,J1\xi}^2 \sigma_{X,J_1}^2 + \sigma_{H,J2\xi}^2 \sigma_{X,J_2}^2 + \sigma_J^2}. \tag{6.7}$$

Note that, the performance of the legitimate user is dependent on perfect channel condition, that allow J_1 and J_2 to perform signal precoding using CSI. With imperfect channel condition, the performance of R is dependent on a robust channel estimation technique as in [45], [4]. The channel estimates of $\mathbf{H}_{J1R}$, $\mathbf{H}_{J2R}$ are obtained by using training symbols from R to J_1 and J_2, respectively. The channel estimates of $H_{J1R}^{(k)}$ and $H_{J2R}^{(k)}$, respectively are given as $\hat{H}_{J1R}^{(k)} = H_{J1R}^{(k)} + \varepsilon_{J1R}^{(k)}$ and $\hat{H}_{J2R}^{(k)} = H_{J2R}^{(k)} + \varepsilon_{J1R}^{(k)}$. Here, $\varepsilon_{J1R}^{(k)}$ and $\varepsilon_{J2R}^{(k)}$ are the channel estimation errors of $H_{J1R}^{(k)}$ and $H_{J2R}^{(k)}$, respectively. Then, the new precoded EH signals denoted as $X'^{(k)}_{J_1}$ and $X'^{(k)}_{J_2}$, are expressed as

$$\begin{aligned} X'^{(k)}_{J_1} &= X_{J_1}^{(k)} + \varepsilon_{A,J_1}^{(k)} = A_{J_1}^{(k)}(H_{J2R}^{(k)} + \varepsilon_{J2R}^{(k)}), \\ X'^{(k)}_{J_2} &= X_{J_2}^{(k)} + \varepsilon_{A,J_2}^{(k)} = A_{J_2}^{(k)}(H_{J1R}^{(k)} + \varepsilon_{J1R}^{(k)}), \end{aligned} \tag{6.8}$$

where $\varepsilon_{A,J_1}^{(k)}$ and $\varepsilon_{A,J_2}^{(k)}$ are the precoding errors due to $\varepsilon_{J2R}^{(k)}A_{J_1}^{(k)}$ and $\varepsilon_{J1R}^{(k)}A_{J_2}^{(k)}$, respectively.

Similarly, the received signal at $R(b)$ based on the impact of $\hat{H}^{(k)}_{J1R}$ and $\hat{H}^{(k)}_{J2R}$ is given as

$$Y^{(k)}_{R(b)} = \begin{cases} H^{(k)}_{TR}X^{(k)}_{I} + N^{(k)} + \varepsilon^{(k)}_{R(b),J_1} + \varepsilon^{(k)}_{R(b),J_2}; & \text{if } \mathscr{L}(\mathscr{V}^{(k)}) = \varepsilon^{(k)}_{R(b)}, \\ H^{(k)}_{TR}X^{(k)}_{I} + N^{(k)} + H^{(k)}_{J1R}X'^{(k)}_{J_1} + H^{(k)}_{J2R}X'^{(k)}_{J_2}; & \text{otherwise,} \end{cases} \tag{6.9}$$

where $\varepsilon^{(k)}_{R(b),J_1} = H^{(k)}_{J1R}\varepsilon^{(k)}_{A,J_2}$, $\varepsilon^{(k)}_{R(b),J_2} = H^{(k)}_{J2R}\varepsilon_{A,J_1}{}^{(k)}_{A,J_1}$, and $\varepsilon^{(k)}_{R(b),J_1}$ and $\varepsilon^{(k)}_{R(b),J_2}$ are the additional noise components to $Y^{(k)}_{R(b)}$ due to precoding error. Then, $\mathscr{L}(H^{(k)}_{J1R}X^{(k)}_{J_1} + H^{(k)}_{J2R}X^{(k)}_{J_2}) = \varepsilon^{(k)}_{R(b)}$, where $\varepsilon^{(k)}_{R(b)} = \varepsilon^{(k)}_{R(b),J_1} + \varepsilon^{(k)}_{R(b),J_2}$. The SINR of $\mathbf{Y}_{R(b)}$ for the condition $\mathscr{L}(\mathscr{V}^{(k)}) = \varepsilon^{(k)}_{R(b)}$ is given as

$$\gamma_{R(b)} = \frac{\mathbb{E}[|\mathbf{X}_I^T\mathbf{H}_{TR}|^2]}{\mathbb{E}[(\sum_{k=0}^{K-1}|\varepsilon^{(k)}_{R(b),J_1}|)^2] + \mathbb{E}[(\sum_{k=0}^{K-1}|\varepsilon^{(k)}_{R(b),J_2}|)^2] + \mathbb{E}[\|\mathbf{N}\|^2]} = \frac{\sigma^2_{X,I}\sigma^2_{H,TR}}{\sigma^2_{\varepsilon,R(b),J_1} + \sigma^2_{\varepsilon,R(b),J_2} + \sigma^2_N}. \tag{6.10}$$

Note that, since R does not need to equalize $H^{(k)}_{J1R}$ and $H^{(k)}_{J2R}$, their respective channel estimation errors $\varepsilon^{(k)}_{J1R}$ and $\varepsilon^{(k)}_{J2R}$ are neglected in (6.10).

The performance of $\xi(b)$ is better than $\xi(a)$ due to high channel correlations between $\mathbf{H}_{J1\xi}$ and $\mathbf{H}_{J1R}$, and also between $\mathbf{H}_{J2\xi}$ and $\mathbf{H}_{J2R}$. Lets denote the the channel correlation between $\mathbf{H}_{J1\xi}$ and $\mathbf{H}_{J1R}$ as ρ_{J_1}. Also, lets denote the channel correlation between between $\mathbf{H}_{J2\xi}$ and $\mathbf{H}_{J2R}$ as ρ_{J_2}. ρ_{J_1} and ρ_{J_2} are expressed as

$$\begin{aligned} \rho_{J_1} &= \frac{\mathbb{E}[\|\mathbf{H}_{J1R}\mathbf{H}^H_{J1\xi}\|]}{\sqrt{\mathbb{E}[\|\mathbf{H}_{J1R}\|^2]\mathbb{E}[\|\mathbf{H}_{J1\xi}\|^2]}}, \\ \rho_{J_2} &= \frac{\mathbb{E}[\|\mathbf{H}_{J2R}\mathbf{H}^H_{J2\xi}\|]}{\sqrt{\mathbb{E}[\|\mathbf{H}_{J2R}\|^2]\mathbb{E}[\|\mathbf{H}_{J2\xi}\|^2]}}. \end{aligned} \tag{6.11}$$

The error due to ρ_{J_1} and ρ_{J_2} is denoted as ε_{ρ,J_1} and ε_{ρ,J_2}, respectively. The channel precodings at J_1 and J_2 from $\xi(b)$ perspective, respectively are given as

$$\begin{aligned} X'^{(k)}_{J_1}(1+\varepsilon_{\rho,J_2}) &= (X^{(k)}_{J_1} + \varepsilon^{(k)}_{A,J_1})(1+\varepsilon_{\rho,J_2}) = A^{(k)}_{J_1}(H^{(k)}_{J2R} + \varepsilon^{(k)}_{J2R})(1+\varepsilon_{\rho,J_2}), \\ X'^{(k)}_{J_2}(1+\varepsilon_{\rho,J_1}) &= (X^{(k)}_{J_2} + \varepsilon^{(k)}_{A,J_2})(1+\varepsilon_{\rho,J_1}) = A^{(k)}_{J_2}(H^{(k)}_{J1R} + \varepsilon^{(k)}_{J1R})(1+\varepsilon_{\rho,J_1}). \end{aligned} \tag{6.12}$$

From ξ perspective, $(1+\varepsilon_{\rho,J_2})$ and $(1+\varepsilon_{\rho,J_2})$ are the impacts on the $X'^{(k)}_{J_1}$ and $X'^{(k)}_{J_2}$, respectively, which degrade the precoded EH signals and increase the precoding errors.

The received signal at $\xi(b)$ is given as

$$Y^{(k)}_{\xi(b)} = \begin{cases} H^{(k)}_{T\xi}X^{(k)}_{I} + J^{(k)} + \varepsilon^{(k)}_{\xi(b),J_1} + \varepsilon^{(k)}_{\xi(b),J_2}; & \text{if } \mathscr{L}(\mathscr{V}^{(k)}) = \varepsilon^{(k)}_{\xi(b)}, \\ H^{(k)}_{T\xi}X^{(k)}_{I} + J^{(k)} + H^{(k)}_{J1R}X'^{(k)}_{J_1}(1+\varepsilon_{\rho,J_2}) + H^{(k)}_{J2R}X'^{(k)}_{J_2}(1+\varepsilon_{\rho,J_1}); & \text{otherwise.} \end{cases} \tag{6.13}$$

where $\varepsilon^{(k)}_{\xi(b),J_1} = \frac{H^{(k)}_{J1R}(X^{(k)}_{J_1}+\varepsilon^{(k)}_{A,J_1})(1+\varepsilon_{\rho,J_2})}{X^{(k)}_{J_2}}$, $\varepsilon^{(k)}_{\xi(b),J_2} = \frac{H^{(k)}_{J2R}(X^{(k)}_{J_2}+\varepsilon^{(k)}_{A,J_2})(1+\varepsilon_{\rho,J_2})}{X^{(k)}_{J_1}}$ and, $\varepsilon^{(k)}_{\xi(b),J_1}$ and $\varepsilon^{(k)}_{\xi(b),J_2}$ are the additional noise components to $Y^{(k)}_{\xi(b)}$. Then, $\mathscr{L}(H^{(k)}_{J1\xi}X^{(k)}_{J_1} + H^{(k)}_{J2\xi}X^{(k)}_{J_2}) = \varepsilon^{(k)}_{\xi(b)}$, where

$\varepsilon_{\xi(b)}^{(k)} = \varepsilon_{\xi(b),J_1}^{(k)} + \varepsilon_{\xi(b),J_2}^{(k)}$. The SINR of $\mathbf{Y}_{\xi(b)}$ for the condition $\mathscr{L}(\mathscr{V}^{(k)}) = \varepsilon_{\xi(b)}^{(k)}$ is given as

$$\gamma_{\xi(b)} = \frac{\mathbb{E}[|\mathbf{X}_I^T\mathbf{H}_{T\xi}|^2]}{\mathbb{E}[(\sum_{k=0}^{K-1}|\varepsilon_{\xi(b),J_1}^{(k)}|)^2] + \mathbb{E}[(\sum_{k=0}^{K-1}|\varepsilon_{\xi(b),J_2}^{(k)}|)^2] + \mathbb{E}[||\mathbf{J}||^2]} = \frac{\sigma_{X,I}^2\sigma_{H,T\xi}^2}{\sigma_{\varepsilon,\xi(b),J_1}^2 + \sigma_{\varepsilon,\xi(b),J_2}^2 + \sigma_J^2}. \tag{6.14}$$

The best scenario for ξ is $\xi(c)$, where the precoding errors due to the channel estimation errors can be avoided at T. However, there will be a precoding error due to $H_{J1R}^{(k)}(1+\varepsilon_{\rho,J_1})$ and $H_{J2R}^{(k)}(1+\varepsilon_{\rho,J_2})$. Hence, the precoded EH signals can be written as

$$\begin{aligned} X_{J_1}^{(k)}(1+\varepsilon_{\rho,J_2}) &= A_{J_1}^{(k)}H_{J2R}^{(k)}(1+\varepsilon_{\rho,J_2}), \\ X_{J_2}^{(k)}(1+\varepsilon_{\rho,J_1}) &= A_{J_2}^{(k)}H_{J1R}^{(k)}(1+\varepsilon_{\rho,J_1}). \end{aligned} \tag{6.15}$$

Then, the received signal at $\xi(c)$ is given as

$$Y_{\xi(c)}^{(k)} = \begin{cases} H_{T\xi}^{(k)}X_I^{(k)} + N^{(k)} + \varepsilon_{\xi(c),J_1}^{(k)} + \varepsilon_{\xi(c),J_2}^{(k)}; & \text{if } \mathscr{L}(\mathscr{V}^{(k)}) = \varepsilon_{\xi(c)}^{(k)}, \\ H_{T\xi}^{(k)}X_I^{(k)} + N^{(k)} + H_{J1R}^{(k)}X_{J_1}^{(k)}(1+\varepsilon_{\rho,J_2}) + H_{J2R}^{(k)}X_{J_2}^{(k)}(1+\varepsilon_{\rho,J_1}); & \text{otherwise}, \end{cases} \tag{6.16}$$

where $\varepsilon_{\xi(c),J_1}^{(k)} = H_{J1R}^{(k)}(1+\varepsilon_{\rho,J_2})$ and $\varepsilon_{\xi(c),J_2}^{(k)} = H_{J2R}^{(k)}(1+\varepsilon_{\rho,J_1})$. Then, $\mathscr{L}(H_{J1\xi}^{(k)}X_{J_1}^{(k)} + H_{J2\xi}^{(k)}X_{J_2}^{(k)}) = \varepsilon_{\xi(c)}^{(k)}$, where $\varepsilon_{\xi(c)}^{(k)} = \varepsilon_{\xi(c),J_1}^{(k)} + \varepsilon_{\xi(c),J_2}^{(k)}$. The SINR of $\mathbf{Y}_{\xi(c)}$ for the condition $\mathscr{L}(\mathscr{V}^{(k)}) = \varepsilon_{\xi(c)}^{(k)}$ is given as

$$\gamma_{\xi(c)} = \frac{\mathbb{E}[|\mathbf{X}_I^T\mathbf{H}_{T\xi}|^2]}{\mathbb{E}[(\sum_{k=0}^{K-1}|\varepsilon_{\xi(c),J_1}^{(k)}|)^2] + \mathbb{E}[(\sum_{k=0}^{K-1}|\varepsilon_{\xi(c),J_2}^{(k)}|)^2] + \mathbb{E}[||\mathbf{J}||^2]} = \frac{\sigma_{X,I}^2\sigma_{H,T\xi}^2}{\sigma_{\varepsilon,\xi(c),J_1}^2 + \sigma_{\varepsilon,\xi(c),J_2}^2 + \sigma_J^2}. \tag{6.17}$$

For all the scenarios of ξ and $R(b)$, the channel precoding error is denoted as ε_A and its variance is denoted as σ_A^2. In this system model, both the channel estimate errors and the channel correlation errors are considered to be the sole contributors of ε_A, and ε_A proportionally increases with the increase in β. To form generalised SINR equation, $\sigma_{H,TR}^2$ and $\sigma_{H,T\xi}^2$ are assumed as 1; then, the SINR of received signal at R and ξ can be written as

$$\gamma = \frac{\sigma_{X,I}^2}{\sigma_N^2 + \beta\sigma_A^2}, \tag{6.18}$$

At a very high SINR of the information signal, σ_N^2 can be neglected. Then (6.18), can be written as

$$\gamma \approx \frac{\sigma_{X,I}^2}{\beta\sigma_A^2}. \tag{6.19}$$

Therefore, even at very high SINR condition, $\beta\sigma_A^2$ can be used to degrade the performance of ξ. The secrecy of $\mathbf{X}_I$ can be improved at $R(a)$ and $R(b)$ by increasing β under the condition that σ_A^2 value in $\mathbf{Y}_{R(a)}$ and $\mathbf{Y}_{R(b)}$ is lesser than σ_A^2 value in $\mathbf{Y}_{\xi(a)}$, $\mathbf{Y}_{\xi(b)}$ and $\mathbf{Y}_{\xi(c)}$. Another observation from (6.18) indicates that, if $\beta \geq 1$, then $\xi(a)$ will always be in negative SINR region.

6.1.1.1 Secrecy rate analysis

The secrecy rate analysis of this system model is based on the Gaussian wiretap channel secrecy capacity, which deduces the difference between Shannon's capacity of R and ξ. The maximum achievable secrecy rate is the secrecy capacity of R [48, 49]. The secrecy capacity of $R(a)$ with respect to $\xi(a)$ and secrecy capacity of $R(a)$ with respect to $\xi(c)$, respectively are given (The notation for the secrecy rate of $R(a)$ with respect to $\xi(c)$ is given as $C_{(c),A}$, where (c) denotes $\xi(c)$ and A denotes $R(a)$. Similar rule is followed for the other three secrecy rate notions.) as:

$$\begin{aligned} C_{(a),A} &= \frac{\Delta f}{k}\sum_{k=0}^{K-1}\left(\log\left(\frac{1+|H_{TR}^{(k)}|^2\gamma_{R(a)}}{1+|H_{T\xi}^{(k)}|^2\gamma_{\xi(a)}}\right)\right), \\ C_{(c),A} &= \frac{\Delta f}{k}\sum_{k=0}^{K-1}\left(\log\left(\frac{1+|H_{TR}^{(k)}|^2\gamma_{R(a)}}{1+|H_{T\xi}^{(k)}|^2\gamma_{\xi(c)}}\right)\right), \end{aligned} \tag{6.20}$$

where $2\Delta f$ is the bandwidth and Δf is the peak frequency deviation. The secrecy capacity of $R(b)$ with respect to $\xi(a)$ and secrecy capacity of $R(b)$ with respect to $\xi(b)$, respectively are given as

$$\begin{aligned} C_{(a),B} &= \frac{\Delta f}{k}\sum_{k=0}^{K-1}\left(\log\left(\frac{1+|H_{TR}^{(k)}|^2\gamma_{R(b)}}{1+|H_{T\xi}^{(k)}|^2\gamma_{\xi(a)}}\right)\right), \\ C_{(b),B} &= \frac{\Delta f}{k}\sum_{k=0}^{K-1}\left(\log\left(\frac{1+|H_{TR}^{(k)}|^2\gamma_{R(b)}}{1+|H_{T\xi}^{(k)}|^2\gamma_{\xi(b)}}\right)\right). \end{aligned} \tag{6.21}$$

Here, the interference of EH signals is used as the external noise to improve the maximum achievable secrecy rate of R, and by increasing β, secrecy capacity can be improved in all scenarios. Even though β can reduce the capacity of $R(b)$ due to the amplification of channel estimation errors, since $\xi(b)$ also has channel correlation error in addition to the channel estimate errors, β will improve R's secrecy capacity.

6.1.1.2 Iterative block decision feedback equalization receiver

In this system model, it is assumed that both R and ξ employ IB-DFE to improve the accuracy of information estimates as proposed in [24]. The IB-DFE based estimate for $X_I^{(k)}$ at R is given as

$$\tilde{X}_I^{(j,k)} = Y_I^{(k)}F^{(j,k)} - \tilde{X}_I^{(j-1,k)}B^{(j,k)}, \tag{6.22}$$

where $j = 0,1,...,J$ and j is the number of iteration followed in IB-DFE receiver and $\tilde{X}_I^{(j-1,k)}$ is the previous iteration value of $\tilde{X}_I^{(j,k)}$, $F^{(j,k)}$ is the iteration of feed forward coefficient and it is given as

$$F^{(j,k)} = \frac{\tilde{F}^{(j,k)}}{\frac{1}{K}\sum_{k=0}^{K-1}\left(\tilde{F}^{(j,k)}H_{TR}^{(j,k)}\right)}, \tag{6.23}$$

where $\tilde{F}^{(j,k)}$ is written as

$$\tilde{F}^{(j,k)} = \frac{H_{TR}^{(j,k)*}}{\left(\frac{\sigma_N^2}{\sigma_{X,I}^2}\right) + |H_{TR}^{(j,k)}|^2 \left(1 - (\rho^{(j-1)})^2\right)}, \tag{6.24}$$

and the correlation factor $\rho^{(j-1)} = \frac{\mathbb{E}[\hat{x}_i^{(j,n)} x_i^{(j,n*)}]}{\mathbb{E}[|x_i^{(j,n)^2}|]}$, where $x_i^{(j,n)}$ is time domain equivalent of $X_I^{(j,k)}$ and $\hat{x}_i^{(j,n)}$ is the extrinsic information of $x_i^{(j,n)}$. Furthermore, $\{X_I^{(j,k)}; k = 0, 1, ..., K-1\} =$ DFT $\{x_i^{(j,n)} g_n; n = 0, 1, ..., N-1\}$, and if the n_{th} time domain inside the cycle prefix, then g_n is either 1 or 0. The feedback co-efficient $B^{(j,k)}$ is written as

$$B^{(j,k)} = F^{(j,k)} H_{TR}^{\widetilde{(j,k)}} - 1. \tag{6.25}$$

In fact, the accuracy of $\tilde{X}_I^{(j,k)}$ increases with each iteration up to its saturation point. Similarly, the accuracy of information estimate can be improved at R and ξ for all the scenarios except $\xi(a)$. For $\xi(a)$, $\tilde{X}_I^{(j,k)}$ is completely distorted by EH signals.

The performance of IB-DFE receiver can be improved at $R(b)$ with improved feed forward input in the iteration. The feed forward estimate, $\tilde{F}^{(j,k)}$ is derived in (6.24) and this estimate can be improved by including the impact of $\beta\sigma_A^2$ in the SINR of the information signal. Therefore, by using (6.18) in (6.24), we get

$$\tilde{F}^{(j,k)} = \frac{H_{TR}^{(j,k)*}}{\left(\frac{\sigma_N^2 + \beta\sigma_A^2}{\sigma_{X,I}^2}\right) + |H_{TR}^{(j,k)}|^2 \left(1 - (\rho^{(j-1)})^2\right)}. \tag{6.26}$$

Here, unlike the eavesdropper, $R(b)$ can take advantage of the available knowledge from the legitimate transmitter and improve the performance of $R(b)$ and therefore, $R(b)$ with improved feedback estimates can perform better than ξ.

6.1.2 Numerical results

In this section, the BER performance of the legitimate user and the eavesdroppers in the system model is analyzed by using Monte Carlo simulations. The signal uses 2.4 GHz frequency band, $T_l = 4 \times 10^{-6}$ and it is considered that all the communication nodes including the eavesdroppers are operating in non line of sight channel condition. The secrecy rate is another performance metric of legitimate user in presence of eavesdropper at various conditions and is analyzed through simulations. In the following simulations, system adopts 4-QAM signal with $K = 256$ and $L = 200$, and IB-DFE receiver is used in R and ξ for improving their error rate performance. The channel estimate error of $\mathbf{H}_{J1R}$ and $\mathbf{H}_{J2R}$ links i.e. ε_{J1R} and ε_{J2R}, respectively are assumed to be equal i.e. $\varepsilon_{J1R} = \varepsilon_{J2R}$ and ε_{J1R} is either 0.02 or 0.1. We assume, that under an exceptionally favorable circumstance, $\rho_{J_1} = \rho_{J_2} = 0.99$ and 0.98; this allows $\xi(b)$ and $\xi(c)$ to perform better than $\xi(a)$. In the following figures, the BER performance results by default illustrates the 4^{th} iteration of IB-DFE decoder unless it is specified as ZF decoding.

Figure 6.3 demonstrates the BER performance of $R(a)$ and $R(b)$. We see that the BER performance of $R(a)$ does not vary with the change in β, due to the successful channel precoding, which is based on complete CSI of EH signals i.e. jamming signals. Also the results of $R(a)$, demonstrate the performance of IB-DFE receiver and BER improves up to 4^{th} iteration. In 1^{st} iteration, without any feedforward and feedback values, the resultant BER of 1^{st} iteration is equal to the ZF decoding. For $R(b)$, channel precoding error occurs due ε_{J1R}, where $\varepsilon_{J1R} = 0.02$ and 0.1 and the results demonstrate that due to precoding error at transmitter, the BER performance of $R(b)$ is poorer as compared $R(a)$. When $\varepsilon_{J1R} = 0.2$, up to $\beta = 4$, the performance of $R(b)$ is equivalent to that of $R(a)$, whereas for $\beta > 4$, the performance of $R(b)$ degrades with the increase in β. The precoding error increases proportionally with the increase in ε_{J1R} and β acts as a multiplication factor in increasing the precoding error.

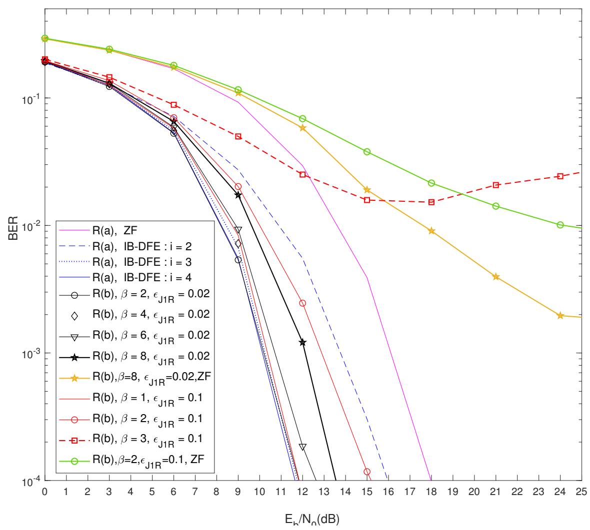

Figure 6.3: BER performance of $R(a)$ and $R(b)$.

Figure 6.4 demonstrates the BER performance of ξ in all the scenarios with comparison to BER of R, and $\xi(a)$ receives an incompatible signal for decoding the information. Unlike $\xi(a)$, with $\rho_{J_1} = \rho_{J_2} = 0.99$ and 0.98, $\xi(b)$ and $\xi(c)$ can partially decode the signal and their performance degrades with the decrease in ρ_{J_1} as in turn increases the precoding errors. Due to high channel correlation between $\mathbf{H}_{J1\xi}$ and $\mathbf{H}_{J1R}$ and similarly between $\mathbf{H}_{J1\xi}$ and $\mathbf{H}_{J1R}$, the jamming EH signals are partially cancelled out in $\xi(b)$ and $\xi(c)$ and allows them to perform better than $\xi(a)$. With $\varepsilon_{J1R} = 0.02$, $\xi(b)$ performs slightly poorer as compared to $\xi(c)$. Even though $\xi(b)$ and $\xi(c)$ can decode information in high channel correlation condition, the BER results of R demonstrate that, by increasing β, the jamming signals can degrade ξ performance, while R suffers a negligible loss.

Figure 6.5 demonstrates the impact of inclusion of $\beta\sigma_A^2$ in the IB-DFE receiver and the results validate the advantage of using (6.26) over (6.24) in the iterative loop. R_i has significant SINR gain over $R(b)$ with the increase in β. At $\beta = 10$, R_i has 0.5 dB SINR gain

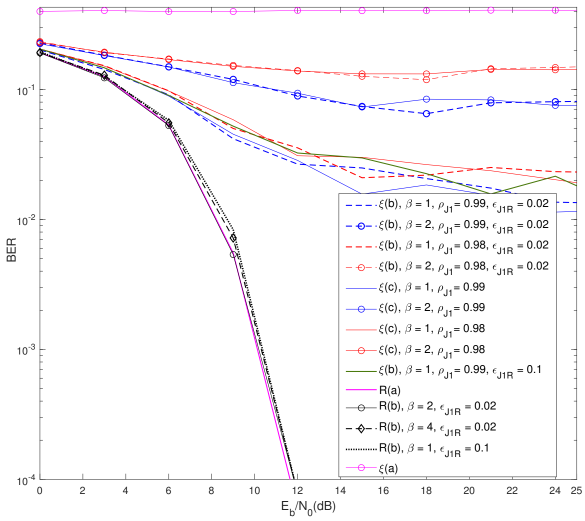

Figure 6.4: BER performance of ξ in all the scenarios with $\varepsilon_{J1R} = 0.02$ in scenario **B**.

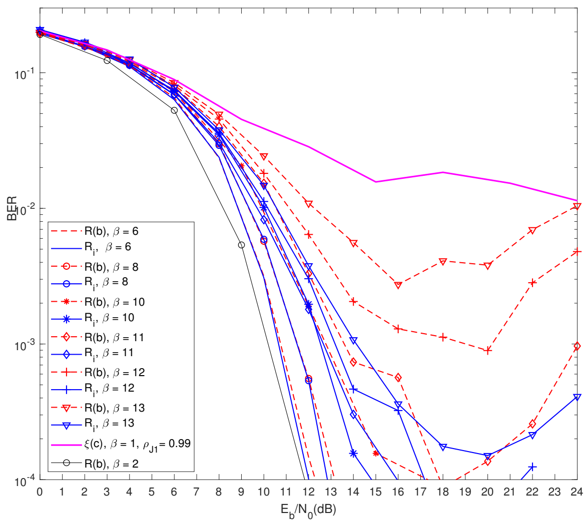

Figure 6.5: BER Performance of $R(b)$ and R_i with $\varepsilon_{J1R} = 0.02$, where R_i denotes $R(b)$ with an improved feedback loop in the IB-DFE receiver.

over $R(b)$ and when $\beta > 12$, R_i has more than 6 dB SINR gain over $R(b)$. The results also illustrate the BER difference between the best performance of $\xi(c)$ i.e. $\xi(c)$ with $\beta = 1$ and $\rho_{J_1} = \rho_{J_2} = 0.99$ versus the performance of R_i with $\beta = 13$.

In Figure 6.6, we compare the BER performance of R_i in Rician fading and Rayleigh frequency flat fading channel conditions. For the simulation of Rician fading, we set, $T_l = 4 \times 10^{-6}$ for 256 symbols, multi path gain range is $0 : -3 : -45$, Doppler shift is 50 and k factor is 10. The results of Figure 6.6 demonstrates that the BER performance of R_i under both the fading conditions have similar effects on the signal performance. The fading effects are relatively low due to the application of SC-FDMA and the BER performance improves with the IB-DFE receiver.

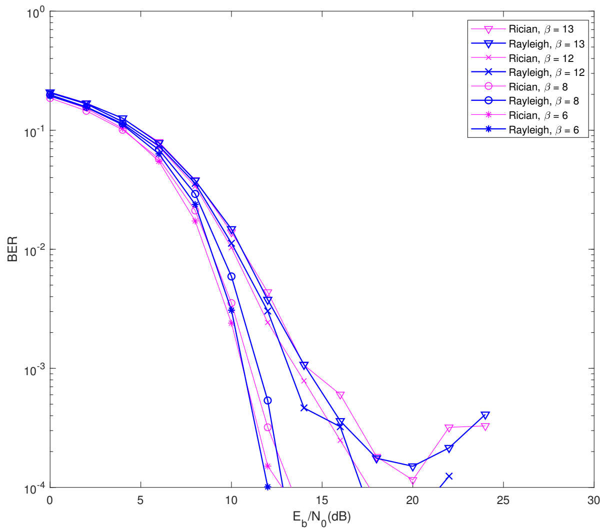

Figure 6.6: BER performance of R_i in Rician fading and Rayleigh fading condition.

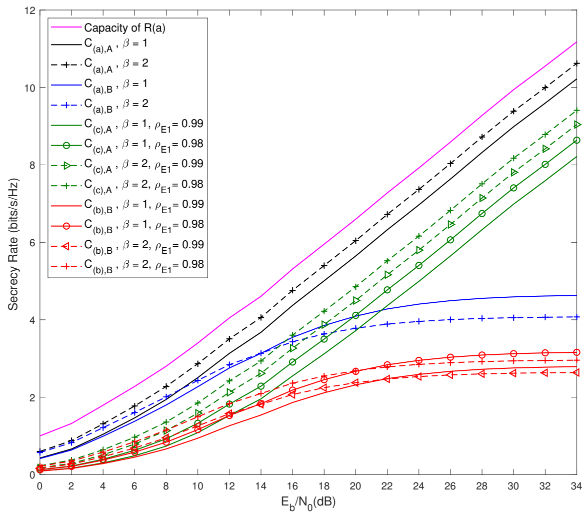

Figure 6.7: The secrecy rate of $R(a)$ and $R(b)$, and in scenario **B**, $\varepsilon_{J1R} = 0.02$.

Figure 6.7 demonstrates the secrecy rate of $R(a)$ and $R(b)$ based on (6.20) and (6.21), respectively. Since $\xi(a)$ is always in negative SINR region, $C_{(a),A}$ has the best performance over $C_{(c),A}$, $C_{(a),B}$ and $C_{(b),B}$. For any given β value, $C_{(c),A}$ always performs better than $C_{(b),B}$ because in $C_{(c),A}$ both $\xi(c)$ and $R(a)$ does not experience channel estimation error. The performance of $C_{(a),B}$ and $C_{(b),B}$ does not improve, when SINR is greater than 20 dB because $R(b)$ experience precoding error due to channel estimate error of EH signals, which is $\varepsilon_{J1R} = 0.02$ and it is independent of SINR of information signal as observed in (6.18) and (6.19). The results of $C_{(c),A}$ and $C_{(a),B}$ proves that, at high SINR (i.e greater than 20 dB) $C_{(c),A}$ can perform better than $C_{(a),B}$, irrespective of ξ's condition. At low SINR (i.e less than 20 dB), performance of $C_{(a),B}$ as compared to $C_{(c),A}$ is better because $R(b)$

takes advantage of $\xi(a)$'s poor performance and this characteristics validates (6.18) and (6.19). Similar to the BER results, the secrecy rate performance of $C_{(c),A}$ and $C_{(b),B}$ are better when $\rho_{J_1} = 0.98$, than their performance when $\rho_{J_1} = 0.99$. The secrecy rate of $R(a)$ improves with the increase in β but in case of $R(b)$, on contrary to the BER results, the secrecy rate degrades with the increase in β due to channel estimate error. Unlike the secrecy rate results of $R(b)$, the impact of channel estimate error on the BER of $R(b)$ is reduced due to the implementation IB-DFE receiver.

Therefore, the results show that the secrecy rate can be improved with the support of accurate channel estimates of legitimate network links and, also by taking advantage of the IB-DFE receiver.

6.2 Energy Efficient Secure Communication Model Against Cooperative Eavesdropper

In the first wiretap model, the system was considered to have a passive eavesdropper with high channel correlation to the legitimate receiver, which is considered as a major limitation of jammers in a wiretap channel. It is mitigated by increasing the jamming signal power that amplifies the error due to the difference in CSI between both channels. The increment in jamming signal power can degrade the eavesdropper's signal to noise ratio (SNR), but this can also increase the negative impact of the jammer's precoding error at legitimate receiver. The effect of the jammer's precoding error at a legitimate receiver can be reduced by using the expected jammer's precoding error as additional noise power feedback in the IB-DFE decoder [57]. Even though the increase in jamming signal power can increase SNR degradation at the eavesdropper, this is not energy efficient and can degrade the performance of the legitimate receiver, if there is any channel estimation error or precoding error in the legitimate network. In [57], the passive eavesdropper does not estimate jamming signal and in this research, the idea of cooperative eavesdropper is explored to estimate jamming signal. Therefore, it is necessary to optimize the jamming signal power and explore counter measures for a cooperative eavesdropper scenario.

In this research work, we consider that the eavesdropper can estimate the CSI between the eavesdropper and its nearest node. With this assumption, we explore the limitation of a legitimate network to act against a robust MIMO cooperative eavesdropper network. There are several studies focused on optimum power allocation at jammer nodes and information transmitter nodes [3, 111]. In [111], the power optimization of the jamming signal based on the CSI of a legitimate receiver to save energy and avoid interference to the legitimate receiver based on its CSI. There are few research works that are focused on multiple eavesdropper scenarios in a wire-tap channel [112–114]. In [113], the eavesdroppers cooperate with each other to detect the information transmission between the transmitter and relays and do not consider detecting jamming signals to remove interference. In [114], the research work is focused on a scenario where multiple eavesdroppers decode information from the base station and the legitimate network with the help of multiple friendly jammers to degrade the SINR of the cooperative eavesdroppers. However, in our work, we consider that the MIMO eavesdropper is closer to the jammer and detects the jamming signal and cooperates with the eavesdropper nearer to the transmitter to estimate information. Thus, under these special circumstances, the research work is focused on hardware configuration and optimum power allocation for the jammer node. We consider that the eavesdropper employs MIMO IB-DFE. IB-DFE is an efficient low complex receiver, as compared to the non-iterative decoder [24, 109] and it can be effectively used with SC-FDMA transmission techniques [110, 115].

In this section, we present an unique scenario in which one eavesdropper detects the jamming signal and another eavesdropper estimates the information signal, and then cooperate with each other to improve both the jamming and information signal estimate. The SINR of improved jamming signal estimate and information signal estimate at the eavesdroppers is derived. The performance of the MIMO IB-DFE receiver with the change in antenna configuration and the impact of change in the SNR of the jamming signal is analysed with the simulated results. The ratio between jamming signal power and information signal power for the given operating SNR is optimized with the support of simulated results. Furthermore, we make the system model more energy efficient by optimizing the power of the jamming signal.

6.2.1 System Model

The system model consists of transmitter A, receiver B, jammer J, and eavesdroppers ξ_1 and ξ_2 in a wire tap channel. It is assumed that ξ_1 is closer to A, while ξ_2 is closer to J. A and B use a single input and single output antenna (SISO) system for information transmission and reception. B has an additional antenna for energy harvesting application. J uses MIMO system for broadcasting jamming signals and it has a separate communication setup to find the location of B and to avoid jamming B. Eavesdroppers use MIMO system model for receiving information and jamming signals. All the nodes in the system model experience Rayleigh frequency selective fading channels. The SISO channel link between A and B is denoted as H_{AB}, whereas the MIMO channel link between J and ξ_1 is denoted as $\mathbf{H}_{J\xi_1}$ and, likewise, all the MIMO single inputs with multiple outputs and the multiple inputs with single output channel links are denoted by using $\mathbf{H}$ and their respective nodes. $\mathbf{H}_{J\xi_1}$ is characterized as $\mathbf{H}_{J\xi_1} \sim \mathcal{CN}(0, \sigma^2_{H,J\xi_1})$, where $\sigma^2_{H,AB}$ is the channel variance. It is assumed that the expected values of channel variances of all the channel links in the system model are equal. All communication nodes experience AWGN and are modeled as zero mean complex Gaussian random variables. AWGN, experienced by A, is denoted as N_A and is characterized as $N_A \sim \mathcal{CN}(0, \sigma^2_{N,A})$, where $\sigma^2_{N,A}$ is the noise variance. Similarly, AWGN is experienced by how all nodes are denoted and characterized. All the legitimate users and jammers are considered to have full channel knowledge. Eavesdroppers are considered to have the channel estimate of all the nodes and this channel estimate depends on the SNR at the eavesdropper node. The channel estimate and the channel estimation error of $\mathbf{H}_{A\xi_1}$ are denoted as $\tilde{\mathbf{H}}_{A\xi_1}$ and $\varepsilon_{H,A\xi_1}$, respectively, where A is the transmitting node and ξ_1 is the receiving node. In similar way, the channel estimate and channel estimation error of the channel between eavesdropper and remaining nodes are denoted. The SNR and SINR of the receiving node ξ_1 are denoted as γ_{ξ_1} and γ_{ξ_1}, respectively. In a similar way, the SNR and SINR are denoted for all the receiving nodes. The SNR of the receiving node considers the power ratio between the received signal and AWGN in an AWGN channel and, therefore, SNR excludes fading coefficient. The SINR of the receiving node considers the power ratio between the received signal and the interference of other signal along with AWGN. The information signal from A, jamming signals from J are denoted as X_I and $\mathbf{X}_J$. The distance between A and ξ_1 is denoted as D_{A,ξ_1}; similarly, the distance between any two nodes in the system model is denoted. In general, the index of transmitting antennas and receiving antennas are denoted as t_a and r_a, respectively, where $t_a = 1, ..., T_a$ with T_a is denoted as the total number of transmitting antennas and $r_a = 1, ..., R_a$, with R_a denoted as the total number of receiving antennas. The total number of R_{ξ_2} transmitting antennas at J is denoted as T_J. The total number of receiving antennas at ξ_1 and ξ_2 are denoted as R_{ξ_1} and R_{ξ_2}, respectively.

6.2.1.1 System Model Equations

The relationship between transmit power of jamming signal and information symbols is given as

$$\begin{aligned} &X_I = S_I P_I; \;\; \mathbf{X}_J = \mathbf{S}_J P_J; \\ &\beta = \frac{T_J P_J}{P_I}. \end{aligned} \tag{6.27}$$

The unamplified version of $\mathbf{X}_I$ and X_J are denoted as S_I and S_J, respectively. $\mathbf{S}_J = [S_{J1} S_{J2} ... S_{JT_J}]^T$, where S_{J1}, $S_{J1} ... S_{JT_J}$ are the unamplified version of modulated signals $(X_{J1} X_{J2} ... X_{JT_J})$ transmitted from J. The transmit powers of $\mathbf{X}_I$ and $\mathbf{X}_J$ are denoted as P_I and $T_J P_J$, respectively, where P_J is the transmit power of single jamming signal stream and all the jamming signal streams are considered to have equal expected values. The ratio between the total transmit power of the Jamming signal and information signal is denoted as β. The relationship between transmit SNR at A and J is given as

$$\begin{aligned} &\gamma_A = \frac{\mathbb{E}[|X_I|^2]}{\mathbb{E}[|N_{\xi_1}|^2]} = \frac{\sigma^2_{X,I}}{\sigma^2_{N,A}} = \frac{P_I}{\sigma^2_{N,A}}; \\ &\gamma_J = \frac{\mathbb{E}[\|\mathbf{X}_J^T\|^2]/T_J}{\mathbb{E}[|N_{\xi_1}|^2]} \frac{\sigma^2_{X,J}/T_J}{\sigma^2_{N,J}} = \frac{P_J}{\sigma^2_{N,J}}; \\ &\frac{\gamma_J T_J}{\gamma_A} = \beta = \frac{T_J P_J}{P_I}, \end{aligned} \tag{6.28}$$

where $\sigma^2_{N,A} = \sigma^2_{N,J}$. The received power of $\mathbf{X}_J$ and X_I at ξ_1 and ξ_2 are, respectively, given in the following equations and for the sake of simplicity, only the path loss factor is considered and the channel fading co-efficient is neglected. The received power of $\mathbf{X}_J$ and X_I at ξ_1 are denoted as $T_J P_{J,\xi_1}$ and P_{I,ξ_1}, respectively. The received power of $\mathbf{X}_J$ and X_I at ξ_2 are denoted as P_{J,ξ_2} and P_{I,ξ_2}, respectively. Then, the relationships between transmit power and received power at ξ_1 and ξ_2 are, respectively, given as

$$\begin{aligned} P_{J,\xi_1} &= P_J{}^{-D_{J,\xi_1}}; \;\; P_{I,\xi_1} = P_I{}^{-D_{A,\xi_1}}; \;\; \beta_{\xi_1} = \frac{T_J P_{J,\xi_1}}{P_{I,\xi_1}}, \\ P_{J,\xi_2} &= P_J{}^{-D_{J,\xi_2}}; \;\; P_{I,\xi_2} = P_I{}^{-D_{A,\xi_2}}; \;\; \beta_{\xi_2} = \frac{T_J P_{J,\xi_2}}{P_{I,\xi_2}}, \end{aligned} \tag{6.29}$$

where β_{ξ_1} and β_{ξ_2} are denoted as the ratio between the total received power of jamming signal and information signal at ξ_1 and ξ_2, respectively. The received signal at B is given as

$$Y_R = \begin{cases} H_{AB}X_I + N_B; & \text{if } \mathscr{L}(\mathscr{V}) = 0, \\ H_{AB}X_I + N_B + \mathbf{H}_{JB}\mathbf{X}_J; & \text{otherwise}, \end{cases} \tag{6.30}$$

where $\mathscr{L}(\mathscr{V}) = 0$ denotes the null space vector of the precoded jamming signal for the respective channel link. The received signal at ξ_1 is

$$Y_{\xi_1} = H_{A\xi_1}X_I + \mathbf{H}_{J\xi_1}\mathbf{X}_J + N_{\xi_1}, \tag{6.31}$$

where $\mathbf{H}_{J\xi_1}\mathbf{X}_{J1}$ is considered as a noise term. The channel estimate error at ξ_1 is given as $\varepsilon_{H,A\xi_1} = f_{MSE}\{\tilde{\mathbf{H}}_{A\xi_1} - \mathbf{H}_{A\xi_1}\}$, where $f_{MSE}(x)$ represents the expected minimum mean square error function. In similar way, the channel estimates and the channel estimate errors of other channels are denoted. The SINR of Y_{ξ_1} are, respectively, given as

$$\begin{aligned} \gamma_{\xi_1} &= \frac{\mathbb{E}[|H_{A\xi_1}X_I|^2]}{\varepsilon_{H,A\xi_1}\mathbb{E}[|X_I|^2] + \mathbb{E}[\|\mathbf{H}_{J\xi_1}\mathbf{X}_J^T\|^2] + \mathbb{E}[|N_{\xi_1}|^2]} \\ &= \frac{\sigma_{X,I}^2\sigma_{H,A\xi_1}^2}{\varepsilon_{H,A\xi_1}\sigma_{X,I}^2 + \sigma_{X,J}^2\sigma_{H,J\xi_1}^2 + \sigma_{N,\xi_1}^2} \\ &= \frac{P_{I,\xi_1}}{(\varepsilon_{H,A\xi_1} + \beta_{\xi_1})P_{I,\xi_1} + \sigma_{N,\xi_1}^2}. \end{aligned} \tag{6.32}$$

For the sake of simplicity, $\sigma_{H,A\xi_1}^2$ and $\sigma_{H,J\xi_1}^2$ are set to 1. The received signal at ξ_2 is given as

$$Y_{\xi_2} = H_{A\xi_2}X_I + \mathbf{H}_{J\xi_2}\mathbf{X}_J + N_{\xi_2}, \tag{6.33}$$

where $\mathbf{H}_{J\xi_1}\mathbf{X}_{J1}$ is considered as a noise term. The SINR of Y_{ξ_2} is given as

$$\begin{aligned} \gamma_{\xi_2} &= \frac{\mathbb{E}[\|\mathbf{H}_{J\xi_2}\mathbf{X}_J^T\|^2]/T_J}{\varepsilon_{H,J\xi_2}\mathbb{E}[\|\mathbf{X}_J\|^2] + \mathbb{E}[|H_{A\xi_2}X_I|^2] + \mathbb{E}[|N_{\xi_2}|^2]} \\ &= \frac{\sigma_{X,J}^2\sigma_{H,\xi_2}^2/T_J}{\varepsilon_{H,J\xi_2}\sigma_{X,J}^2 + \sigma_{X,I}^2\sigma_{H,A\xi_2}^2 + \sigma_{N,\xi_2}^2} \\ &= \frac{P_{J,\xi_2}}{T_J(\varepsilon_{H,J\xi_2} + (1/\beta_{\xi_2}))P_{J,\xi_2} + \sigma_{N,\xi_2}^2}, \end{aligned} \tag{6.34}$$

where the SINR of each jamming signal stream is estimated separately. For the sake of simplicity, $\sigma^2_{H,J\xi_2}$ and $\sigma^2_{H,A\xi_2}$ are considered as 1. γ_{ξ_1} and γ_{ξ_2} can be improved by reducing the signal interference.

We consider that ξ_2 is closer to J and the information signal strength is lower than the jamming signal and, with this condition, by using IB-DFE, the impact of signal interference can be reduced. The following section briefly explains IB-DFE for the MIMO model.

6.2.1.2 Iterative Block Decision Feedback Equalization Decoder

All the communicating nodes use the SC-FDMA transmission technique and the decoders use IB-DFE. It is assumed that $R_a \geq T_a$ with perfect receiver synchronization for all antennas. The information symbol in the time and frequency domains are denoted as $\{x_n^{(t_i)}; n = 0, 1, ..., N-1\}$ and $\{X_k^{(t_i)}; k = 0, 1, ..., K-1\}$, respectively, where x and X are the information symbol in time and frequency domain, n and k are the index of the symbol in time and frequency domain, respectively. The received signal in the time and frequency domains are denoted as $\{y_n^{(r)}; n = 0, 1, ..., N-1\}$ and $Y_k^{(r)}; k = 0, 1, ..., K-1$, respectively. The received signal in matrix format is denoted as $Y_k^{(r)} = [Y_k^{(1)}, Y_k^{(2)}, ..., Y_k^{(R)}]^T$ and Y_k at the receiver is given as

$$Y_k = H_k^{(r,t)} X_k + N_k, \tag{6.35}$$

where $H_k^{(r,t)}$ denotes the $R \times T$ channel matrix with k^{th} frequency. N_k is AWGN with variance $N_0/2 = \sigma_n^2$. The linear minimum mean square error (LMMSE) decision of $x_n^{(t_i)}$ from the IB-DFE receiver is $\tilde{X}_k = [\tilde{X}_k^{(1)}, \tilde{X}_k^{(2)}, ..., \tilde{X}_k^{(R)}]^T$, which is given as

$$\tilde{X}_k = \frac{Y_k H_k^H}{H_k H_k^H + I_N (\gamma_{X_k})^{-1}}, \tag{6.36}$$

where $\gamma_{X_k} = \frac{|\mathbb{E}[|X_k^{(t_i)}|^2]}{|\mathbb{E}[|N_k|^2]}$, and γ_{X_k} is assumed to be equal for all the values of t_a and r_a. The LMMSE for the massive MIMO low complex receiver is given in [116],

$$\tilde{X}_k = Y_k F_k - \bar{X}_k B_k, \tag{6.37}$$

where F_k and B_k are the feed forward and feedback of the IB-DFE receiver. B_k reduces the residual interface in each iteration. F_k and B_k are, respectively, given as

$$\begin{aligned} F_k &= \Psi \Lambda_k^H H_k^H, \\ B_k &= H_k F_k - I_N, \end{aligned} \tag{6.38}$$

where $[\Lambda]_{(i,i')} = exp(j\arg[H]_{(i,i')})$, and $(i, i^{'})$ denotes the index of an element in the matrix. Ψ denotes a diagonal matrix and its $(t,t)^{th}$ element is given as $\sum_{k=0}^{K-1} \sum_{r=1}^{R} |H_k^{(r,t)}|^2$.

6.2.1.3 Decoding Information by Using Jamming Signal Estimate

The information signal can be decoded at ξ_1 by following the next steps.

1 The information signal estimate and estimate error are given as $\tilde{\mathbf{X}}_I$ and $\varepsilon_{X,I}$, respectively. Estimate the jamming signal at ξ_2, by using $\varepsilon_{X,I}$, $\tilde{\mathbf{H}}_{A\xi_2}$ and $\tilde{\mathbf{H}}_{J\xi_2}$ in (6.37).

2 The jamming signal estimate and estimate error are given as $\tilde{\mathbf{X}}_J$ and $\varepsilon_{X,J}$, respectively. Estimate the information signal at ξ_1, by using $\varepsilon_{X,J}$, $\tilde{\mathbf{H}}_{A\xi_1}$ and $\tilde{\mathbf{H}}_{J\xi_1}$ in (6.37).

The SINR of jamming signal at ξ_2 can be improved by using $\tilde{\mathbf{H}}_{A\xi_2}$ and (6.34) can be written as

$$\begin{aligned}\gamma_{\xi_2} &= \frac{\mathbb{E}[\|\mathbf{H}_{J\xi_2}\mathbf{X}_J^T\|^2]/T_J}{\varepsilon_{H,J\xi_2}\mathbb{E}[\|\mathbf{X}_J^T\|^2] + \varepsilon_{H,A\xi_2}\mathbb{E}[\|X_I\|^2] + \mathbb{E}[|N_{\xi_1}|^2]} \\ &= \frac{P_{J,\xi_2}}{T_J P_{J,\xi_2}(\varepsilon_{H,J\xi_2} + \frac{\varepsilon_{H,A\xi_2}+\varepsilon_{X,I}}{\beta_{\xi_2}}) + \sigma^2_{N,\xi_2}}.\end{aligned} \tag{6.39}$$

The SINR of the information signal at ξ_1 can be improved by using $\tilde{\mathbf{H}}_{A\xi_1}$, and (6.32) can be written as

$$\begin{aligned}\gamma_{\xi_1} &= \frac{\mathbb{E}[|H_{A\xi_1}X_I|^2]}{\varepsilon_{H,A\xi_1}\mathbb{E}[\|X_I\|^2] + (\varepsilon_{H,J\xi_1} + \varepsilon_{X,J})\mathbb{E}[\|\mathbf{X}_J^T\|^2] + \mathbb{E}[|N_{\xi_1}|^2]} \\ &= \frac{P_{I,\xi_1}}{P_{I,\xi_1}(\varepsilon_{H,A\xi_1} + (\varepsilon_{H,J\xi_1} + \varepsilon_{X,J})\beta_{\xi_1}) + \sigma^2_{N,\xi_1}} \\ &= \frac{T_J P_{J,\xi_1}}{T_J P_{J,\xi_1}(\varepsilon_{H,A\xi_1} + (\varepsilon_{H,J\xi_1} + \varepsilon_{X,J})\beta_{\xi_1}) + \sigma^2_{N,\xi_1}}.\end{aligned} \tag{6.40}$$

From the legitimate users' perspective for the given scenario, as in Figure 6.8, where ξ_1 is located in such a way that reduces the interference of $\mathbf{X}_J$ in the best possible way at ξ_1 and ξ_2 is located in such a way that reduces the interference of X_I in the best possible way at ξ_2. If J reduces the transmit power of jamming signal to reduce the SINR at ξ_2, then this will reduce the interference of $\mathbf{X}_J$ at ξ_1 but, at the same time, the quality of jamming signal estimate will reduce at ξ_2. Thus, J needs to find an optimum transmit power for the jamming signal.

The jammer can take counter measures against the active cooperative eavesdropper by adjusting β. The desired value of β_{ξ_1} and β_{ξ_2} for the legitimate users is $\beta_{\xi_1} \geq 1$ and $\beta_{\xi_2} \leq 1$, respectively, but this desired condition is not feasible, since received power will change for eavesdroppers at different locations. If $\beta_{\xi_2} = 1$ or $\beta_{\xi_2} < 1$, then from (6.34) and (6.39), we can understand that the SINR will be below the threshold to estimate $\mathbf{X}_J$. Even though $\beta_{\xi_2} = 1$ or $\beta_{\xi_2} < 1$ is the desired condition for countering ξ_2 from estimating $\mathbf{X}_J$, and this condition will eventually allow ξ_1 to estimate X_I, even without estimating $\mathbf{X}_J$, since the interference of $\mathbf{X}_J$ is minimal. Therefore, J should keep $\beta_{\xi_2} > 1$ and $\beta_{\xi_2} < 1$ and should also maintain the best possible balanced $\mathbf{X}_J$ interference at ξ_1 and X_I at ξ_2. One of the main advantages of J is that two jamming signals combined to form the artificial

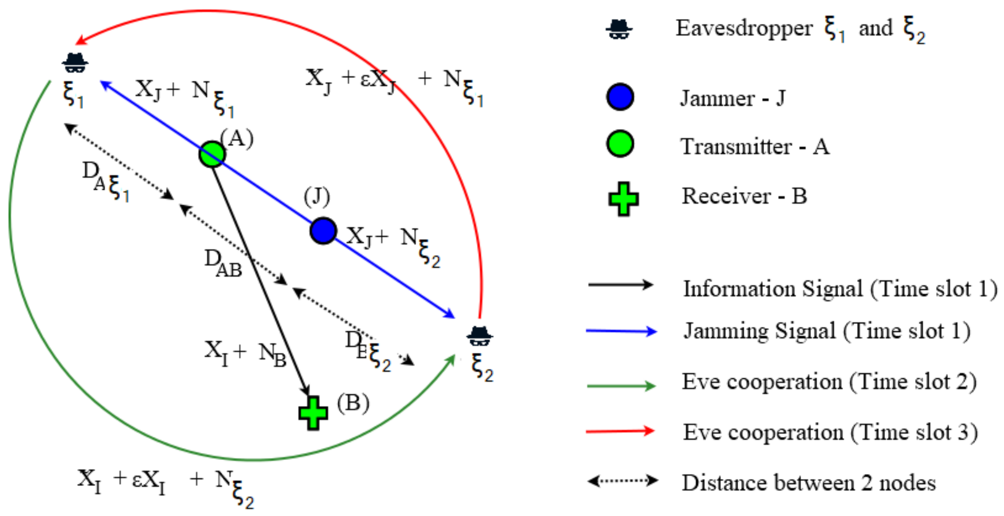

Figure 6.8: Cooperative eavesdroppers in the system model. In this model, the jamming signal does not interfere with legitimate users.

noise interference for eavesdroppers, but ξ_2 should estimate both the jamming signals individually, and this is evident from (6.34) and (6.39). From (6.28), it is evident that J can use two jamming signals with approximately equal power to create artificial noise. Contrary to J, this adversely affects ξ_2 estimation of $\mathbf{X}_J$, the SNR of X_{J1} and X_{J2} as an independent signal stream is half the SNR of $\mathbf{X}_J$. Thus, J can counteract against the active cooperative eavesdropper network by adjusting β value while considering the SINR value from (6.34), (6.39), (6.32) and (6.40). The following steps are required to find the optimum β value.

1 Find the approximate SNR value for the system model and it is denoted as γ_{sys}. Follow further steps to determine optimum β, based on γ_{sys}.

2 Set the maximum acceptable BER performance level of ξ_1 at γ_{sys} under the non cooperative scenario and the SINR is given in (6.32) and under the non cooperative scenario T_J does not impact the BER of ξ_1. In cooperative eavesdropper scenario, for both ξ_1 and ξ_2, their BER performance for a given γ_{sys} is dependent on SINR, T_J, the number of receiving antenna and IB-DFE, the BER performance of ξ_1.

3 Then, the BER performances of ξ_2 and ξ_1 can be degraded by optimizing the β value and by increasing T_J.

The equation for $\varepsilon_{X,J}$ at ξ_2 is given as

$$\varepsilon_{X,J} = f_{MSE}\left\{\frac{P_J}{\sigma^2_{N,J} + (\varepsilon_{X,I}/\beta_{\xi_2})(1+\varepsilon_{H,J\xi_2})}\right\} \quad ; \quad P_J = \frac{\sigma^2_{X,J}}{T_J}. \tag{6.41}$$

In general, $\varepsilon_{X,I}$ increases with the increase in β_{ξ_2} but in contrast $1/\beta_{\xi_2}$ decreases the $\varepsilon_{X,J}$ value. Therefore, for a given γ_{sys}, the optimum β_{ξ_2} is the maximum β_{ξ_2} value at which the value of $(\varepsilon_{X,I}/\beta_{\xi_2})$ is maximum. In general, the rate of increase in $\varepsilon_{X,I}$ will gradually decrease after certain β_{ξ_2} value.

In the following Section, we estimate the approximate β value through Monte Carlo simulation.

6.2.2 Numerical Results

In this section, the BER performance of the information signal estimate at ξ_1 and the expected error estimate of the Jamming signal estimate at ξ_2 are demonstrated and analyzed by using Monte Carlo simulations. The signal uses a 2.4 GHz frequency band and it is considered that all the communication nodes including the eavesdroppers are operating at line of sight channel condition. As in the Figure 6.8, $D_{A,\xi_1} = 5$ m, $D_{A,J} = 5$ m, $D_{\xi_1,\xi_2} = 15$ m, $D_{\xi_1,J} = 10$ m, $D_{\xi_2,J} = 5$ m and $D_{A,\xi_2} = 10$ m. The path loss factor for an indoor environment is considered as 2. In the following simulations, the system uses the 4-QAM modulation signal and adopts the IB-DFE receiver at ξ_1 and ξ_2 for improving their error rate performance. We have adopted 4-QAM modulation over other higher order modulations because 4-QAM signal has better error-rate performance over other higher-order modulation signals. This approach gives an advantage to eavesdroppers in estimating information signal and, if the jammer can successfully obscure eavesdroppers from estimating the 4-QAM signal, then this jamming approach can be easily adopted for other higher-order modulation signals. The channel estimate error for the channel links between the nearest node to ξ_1 and ξ_2 are considered as 0.01 (In this system model, for the indoor environment with slow varying fading scenario, we consider SC-FDMA model with Rayleigh frequency selective fading channel condition between all the nodes. The channel estimation error of the Rayleigh frequency selective fading channel for the system that uses a robust channel estimation technique is less than 0.01 [45]. Since A and J are in a fixed location, to estimate the channel condition between A and ξ_1, the passive eavesdropper transmits a low power pilot signal to ξ_1 from the location of A, and then ξ_1 estimates the channel condition. Similarly, the channel condition between J and ξ_2 can be estimated. To avoid detection, passive eavesdroppers use a low power pilot signal, but this can lead to an increase in the channel estimation error with the increase in distance between the passive eavesdropper and the active eavesdropper. Therefore, in this system model, the channel estimation between A and ξ_2, and J and ξ_1, are not considered. For the sake of simplicity, the passive eavesdroppers that are used for estimating A to ξ_1, and J to ξ_2 channel links are not mentioned in the system model.). In the following figures, all BER curves, by default, illustrate the 4^{th} iteration of the IB-DFE decoder unless specified as ZF decoder and, by default, $T_I = 1$. For this system model to find the optimum β value, P_J is changed in order to change the β value and $P_I = 1$ in all simulations. P_I is constant to avoid performance degradation at an legitimate receiver.

Figure 6.9 demonstrates the BER performance of ξ_1 with $R_{\xi_1} = 2$. In this simulation, ξ_1 does not receive the jamming signal estimate feedback from ξ_2. The BER performance degrades with the increase in β_{ξ_1} value and also by increasing R_{ξ_1}. In Figure 6.10, the comparison of BER results demonstrates that ξ_1 can improve BER by increasing R_{ξ_1} when $\beta_{\xi_1} = 0.375$, as compared to that of when $\beta_{\xi_1} = 1$.

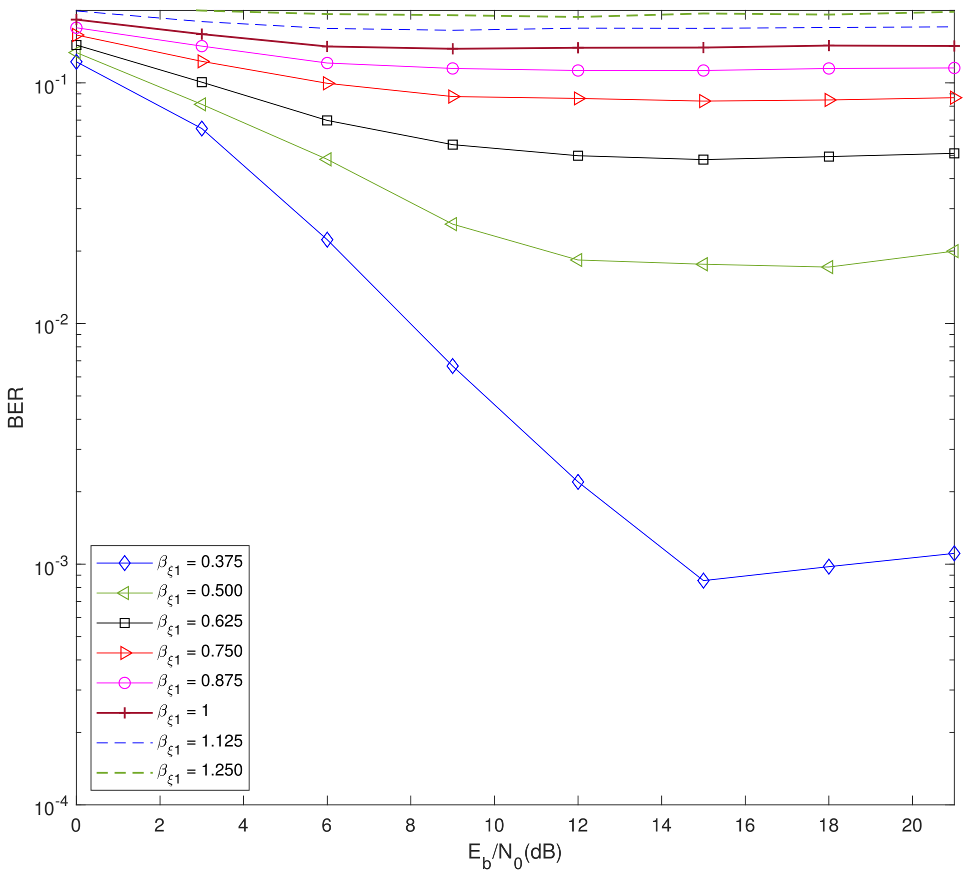

Figure 6.9: The BER results of ξ_1 without the feedback of jamming signal estimate, where $R_{\xi_1} = 2$, $T_I = 1$.

Table 6.1 is an tabulation of Figure 6.9 values and, with this, β_{ξ_1} and β_{ξ_2} are calculated based on the path loss factor, distance between signal transmitting node and receiving node, and P_J and P_I.

In the following simulations, $\gamma_{sys} = 12$ dB is considered as an operating SNR and, for this operating SNR, we determine the optimum β_{ξ_1} that is suitable for legitimate users to degrade the performance of the cooperative eavesdropper. In Figures 6.11 and 6.12, for the fixed operating SNR, i.e., 12 dB, the performance of ξ_2 is measured for β_{ξ_2} values against the expected jamming signal estimate error. Since the jamming signal is random in nature, instead of BER, the expected error for detecting jamming signal is considered for performance measurement.

Figure 6.11 demonstrates that the expected error of the jamming signal estimate error

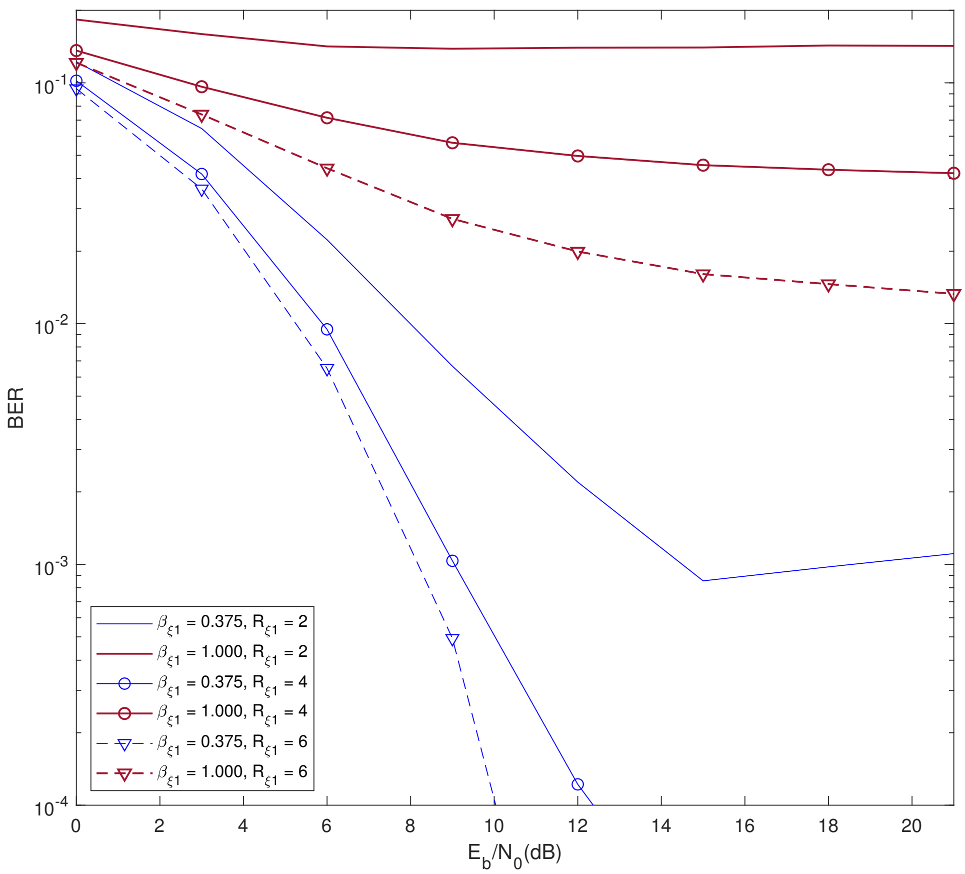

Figure 6.10: The BER results of ξ_1 without the feedback of jamming signal estimate, where $R_{\xi_1} = 2$, $T_J = 1$.

reduces with the increase in β_{ξ_2} value, but the rate of reduction in error saturates with the increase in β_{ξ_2}. In this simulation, the performance of ξ_2 can be degraded by increasing T_J at the J. By increasing the T_J, we can reduce the SNR of individual jamming signals while keeping the total power of combined jamming signals at constant. In order to use the IB-DFE receiver, ξ_2 should satisfy $R_{\xi_2} \geq T_J$. Thus, in this simulation, we set $R_{\xi_2} = T_J$. The observation of the results of Figure 6.11, based on the increase in T_J, degrades the performance of ξ_2, even if $R_{\xi_2} = T_J$, which satisfies (6.41). Therefore, by increasing T_J, J can degrade ξ_2 performance. Figure 6.12 demonstrates the drastic performance improvement of ξ_2 with the application of the IB-DFE decoder over the ZF decoder with the increase in R_{ξ_2}. The increase in T_J, degrades SNR, as in (6.41), but this SNR degradation impact is reduced with the increase in feedback diversity order in IB-DFE, due to R_{ξ_2}. Therefore, with the increase in R_{ξ_2}, the performance degradation due to SNR degradation is lower in IBDFE, as compared to ZF.

Figure 6.13 demonstrates the BER results of the information signal after reducing

Table 6.1: The received signal power of $\mathbf{X}_J$ and X_I at ξ_1 and ξ_2, β_{ξ_1} and β_{ξ_2} for the given transmit power, and $\varepsilon_{X,J}$ (is considered at 12 dB SNR) from Figure 6.9.

	P_I	$T_J P_J$	P_{I,ξ_1}	P_{J,ξ_1}	β_{ξ_1}	P_{I,ξ_2}	P_{J,ξ_2}	β_{ξ_2}	$\varepsilon_{X,I}$
1	100	150	4	1.5	0.375	1	3	3	0.0022
2	100	200	4	2.0	0.500	1	4	4	0.0184
3	100	250	4	2.5	0.625	1	5	5	0.048
4	100	300	4	3.0	0.750	1	6	6	0.086
5	100	350	4	3.5	0.875	1	7	7	0.1125
6	100	400	4	4.0	1.000	1	8	8	0.1399
7	100	450	4	4.5	1.125	1	9	9	0.1685
8	100	500	4	5.0	1.250	1	10	10	0.1878

the interference of the jamming signal by using the jamming signal estimate from ξ_2. The expected jamming signal estimate error is tabulated in Table 6.2. To degrade the performance of ξ_1 and ξ_2, J increases T_J, this is observed from the BER results. When T_J is increased, the performance of ξ_2 degrades and the error in the jamming signal estimate feedback increases, as in Table 6.2. The BER results show that, by increasing the β_{ξ_1} value above 1 and by increasing T_J, J can degrade ξ_1 performance. Even though increase in β_{ξ_1} degrades the BER results of ξ_1, it is optimal to set $\beta_{\xi_1} = 1$ instead of increasing β_{ξ_1} above 1. This is observed with the increase in T_J. Therefore, from the simulated results, for operating SNR at 12 dB, it is optimal to set $\beta_{\xi_1} = 1$.

Table 6.2: Tabulation of $E[\{\varepsilon_{X,J}\}]$ from Figure 6.11.

	T_J	$E[\{\varepsilon_{X,J}\}]$ at $\beta_{\xi_1} = 1$	$E[\{\varepsilon_{X,J}\}]$ at $\beta_{\xi_1} = 1.125$	$E[\{\varepsilon_{X,J}\}]$ at $\beta_{\xi_1} = 1.250$
1	6	0.2522	0.2210	0.2087
2	8	0.3374	0.2615	0.2477
3	10	0.3880	0.3203	0.2797
4	11	0.4790	0.4087	0.3450

Figure 6.14 demonstrates the advantage of using IB-DFE over the ZF decoder at ξ_1. Even though IB-DFE performs better than ZF, the increase in T_J can degrade the performance of IB-DFE and the performance gap between IB-DFE and ZF decreases with the increase in T_J. Therefore, with the help of T_J and β, J can degrade cooperative eavesdropper performance with the least possible energy expenditure. The comparison of results of the ZF and IB-DFE decoder at $T_J = 11$ shows that the performance of IB-DFE is better than that of ZF. The comparison of IDBFE performance in terms of SNR shows that there is a slight performance degradation at SNR—18 dB over SNR 15 dB—and this result is contrary to the expected result. The reason for this unexpected degradation in BER is due to the incorrect noise power input in the feed forward in (6.38), and for the single antenna case, refer to [57] (eq. 21). The amount of energy saved at J, when $\beta_{\xi_1} = 1$ over $\beta_{\xi_1} = 1.25$, is calculated as 25%.

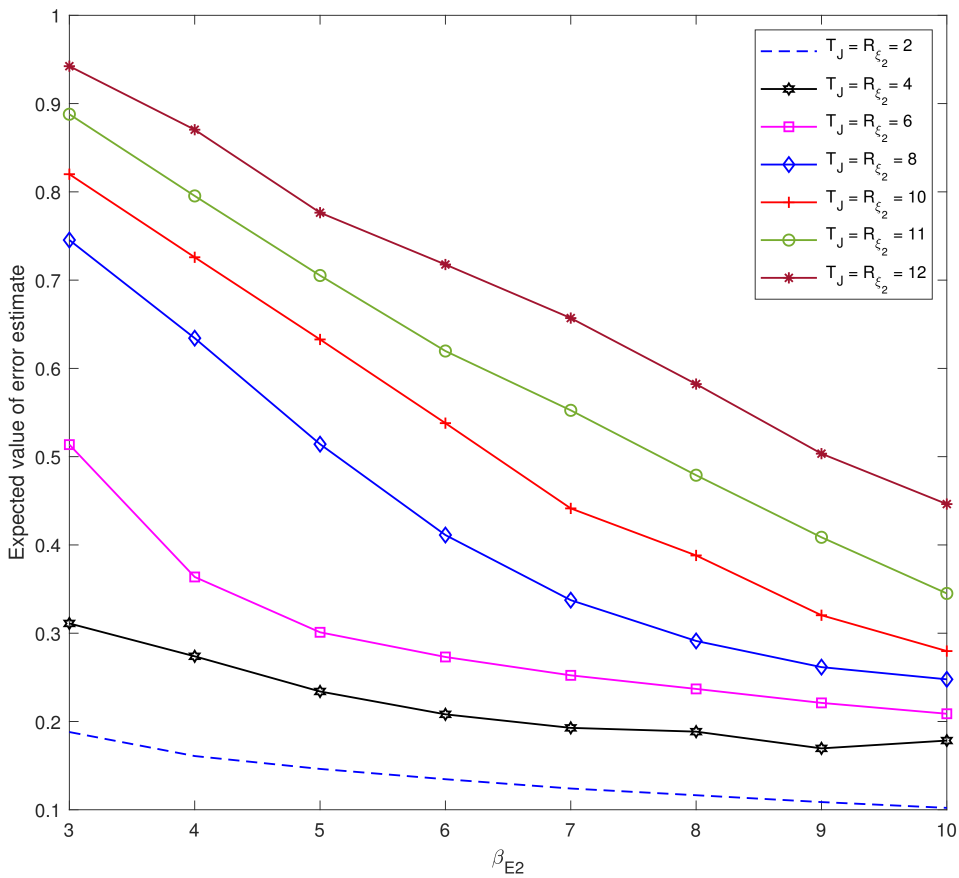

Figure 6.11: The expected jamming signal estimate error at ξ_2 with the feedback of information signal estimate, where $T_J = R_{\xi_2}$.

6.3 Conclusions

In this chapter, we present two wiretap physical layer security models in two different scenarios and study threats from passive and active eavesdroppers, further we provide countermeasures against those eavesdroppers and improve the secrecy rate of the legitimate network. In both the models, energy harvesting signals are used as jamming signals against eavesdroppers. In the first system model, we implemented a SWIPT based self jamming physical layer security model which relies on the channel precoding method to securely transmit information to the legitimate user. We considered different case studies by assuming that eavesdropper has high channel correlation with the legitimate user. We also consider the possibility of channel estimate error (channel link between jamming antennas to the legitimate user) that negatively affects the channel precoding. All the study cases are analysed with the theoretical expressions supported by the simulation results.

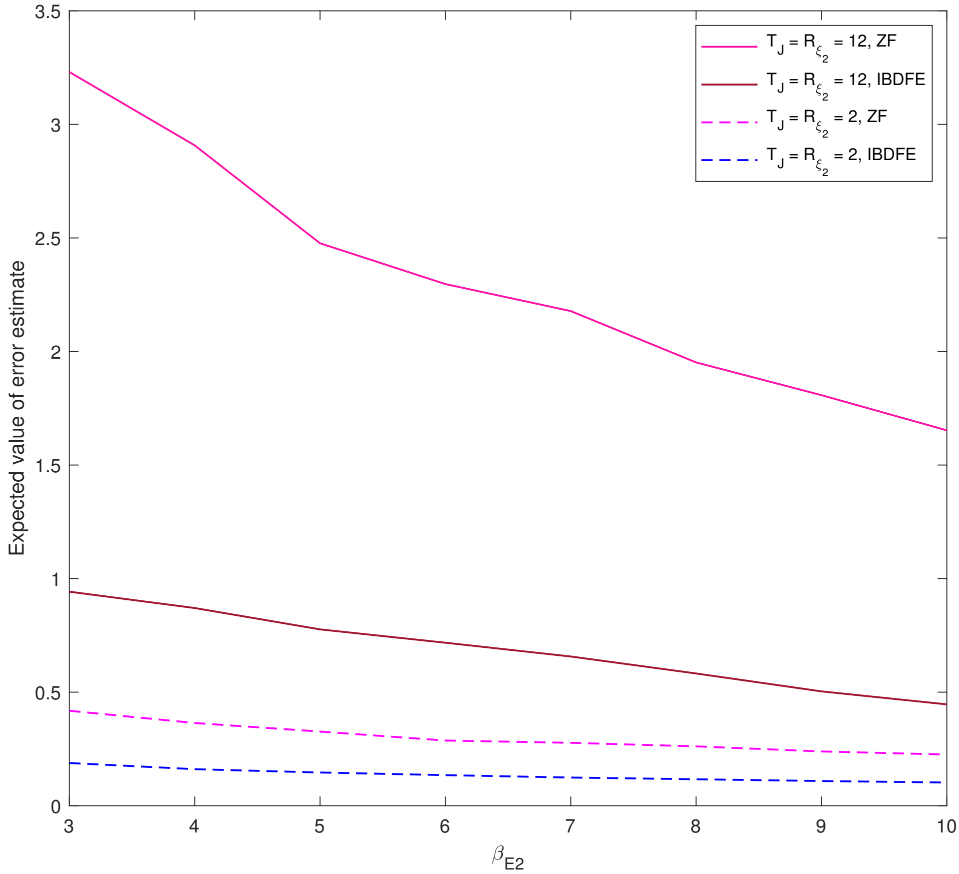

Figure 6.12: The performance of IB-DFE versus ZF at ξ_2, where the feedback of information signal estimate is included to reduce interference.

The BER performance of legitimate user and eavesdropper are improved by using IB-DFE receiver and we conclude that, the channel precoding error can be further reduced at legitimate user by taking advantage of all the available knowledge (i.e. including variance of channel precoding error) in IB-DFE receiver. Thus, legitimate users could perform better than the eavesdropper and the performance of legitimate users improves over eavesdropper with the increase in jamming signal power. The secrecy rate analysis of legitimate users demonstrates that the performance of legitimate users with the channel precoding error does not improve beyond 20 dB SINR and slightly degrades with increase in jamming signal power. In case of perfect channel precoding, the secrecy rate performance of legitimate users improves proportionally with the increase in SINR and with the increase in jamming signal power.

Since the result of the first model shows that the secrecy rate of legitimate networks can be improved if it has lower channel estimation error than eavesdroppers. Therefore, in the second system model, we study a cooperative eavesdropper model in a wire-tap

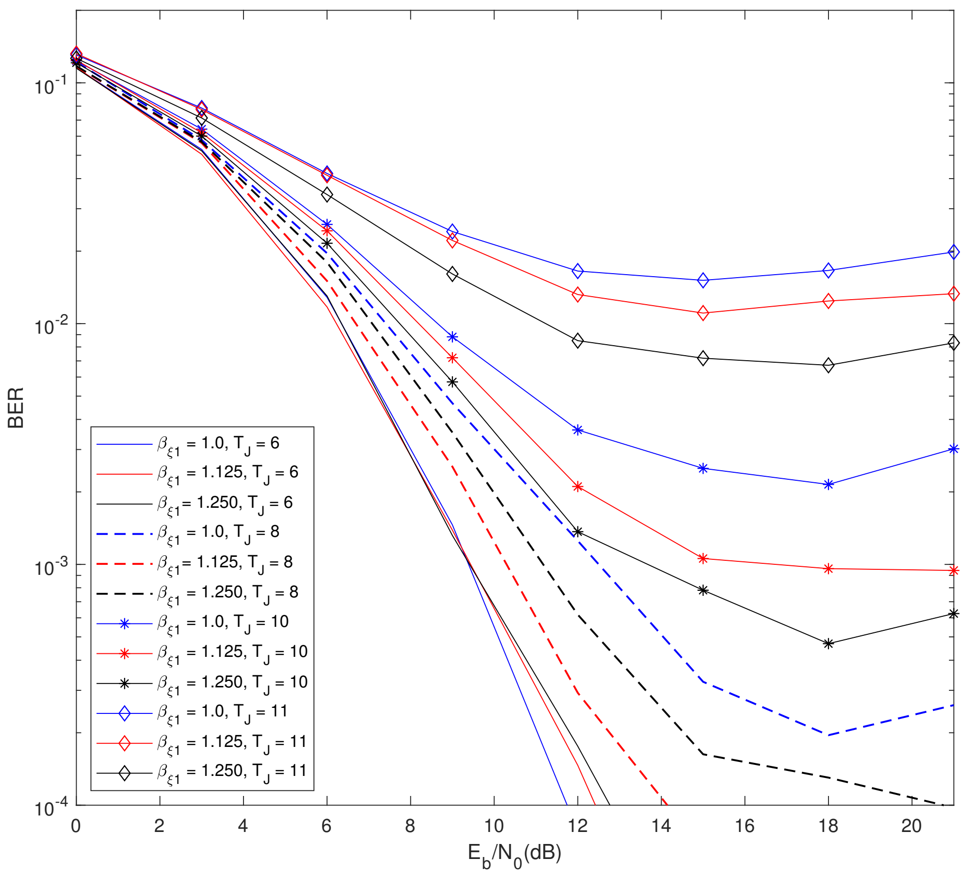

Figure 6.13: The BER results of ξ_1 with the feedback of the jamming signal estimate, where $T_J = R_{\xi_2}$.

channel and derive the SINR of the jamming signal and information signal for the cooperative eavesdroppers network. We specifically consider that the eavesdropper has the CSI of the nearest node with negligible channel estimate error in order to study the optimum β (i.e., power ratio between the jamming signal and information signal). The simulated results of the expected jamming signal estimate error at the nearest eavesdropper (i.e., ξ_2) to the jammer shows that, by increasing the total of number of antennas at the jammer, the jammer can degrade the performance of ξ_2, even if ξ_2 has an equal number of receiving antennas. Therefore, jamming the signal SNR degradation at ξ_2 can degrade the performance of the MIMO IB-DFE receiver.

The BER results of the information signal at the nearest eavesdropper (i.e., ξ_1) to the transmitter show that the BER of ξ_1 can be degraded by optimizing the β value at ξ_1 to 1. The optimization of β leads to energy efficient and secure communication, since $\beta = 1$ at ξ_1 is better for the legitimate network than for using a β greater than 1. Therefore, we conclude that, under a severely restricted environment, a legitimate network can improve

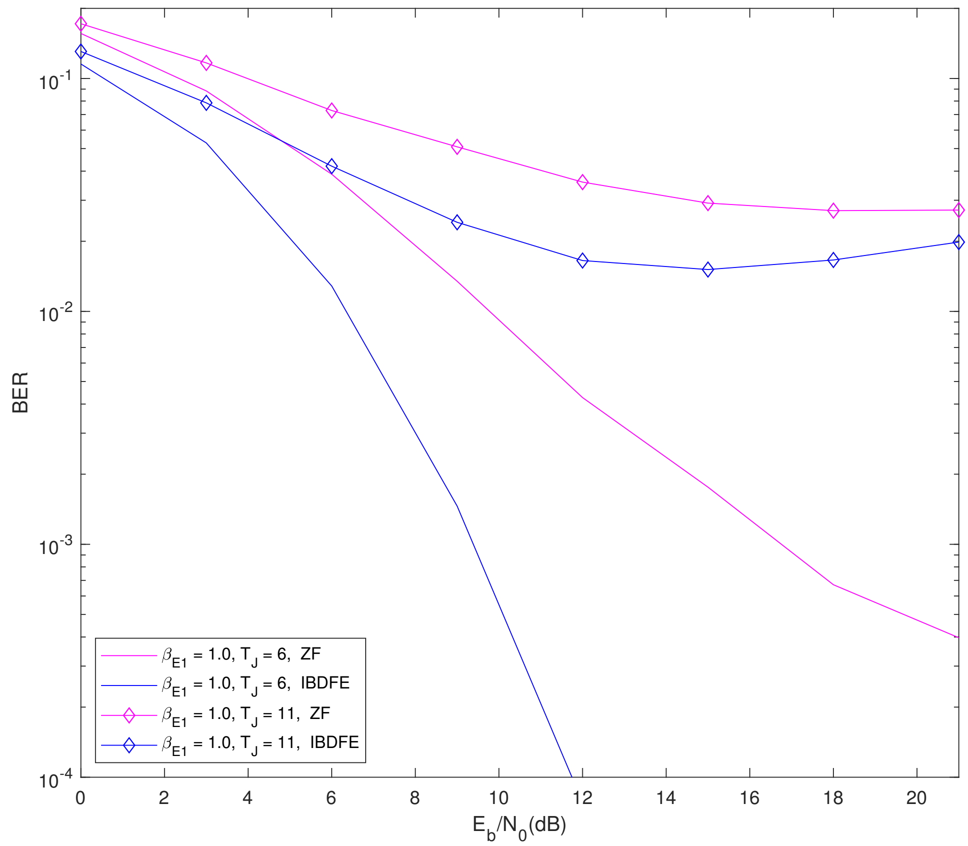

Figure 6.14: The performance of IB-DFE versus ZF at ξ_1, where the feedback of the jamming signal estimate is included to reduce interference.

the secrecy rate and can achieve better energy efficiency by increasing the number of antennas at a jammer and by optimizing β.

7 Conclusion

This thesis studies novel SWIPT techniques and adopts SWIPT for channel estimation and physical layer security purposes.

In chapter 3, we introduced a new SWIPT technique described as M-SWIPT technique. This scheme can be implemented in any M-QAM modulation and with the help of HCS, we can increase the power of low amplitude symbols and thus increase the SNR of low amplitude symbols. Furthermore, this improves the energy efficiency of low amplitude symbols as compared to traditional PS-SWIPT. We studied the impact of CPs in EH using hybrid constellation shaping to improve the spectral efficiency. It was shown that M-SWIPT has better SER performance as compared to PS-SWIPT. It can also outperform PS-SWIPT in terms of achievable rates. Especially at low SNR regions, the performance of M-SWIPT is much better than PS-SWIPT. In terms of maximum achievable rate, M-SWIPT has a SNR gain between 2 to 7 dB at the low SNR region (i.e. between 2 to 18 dB). Therefore, M-SWIPT could be a suitable candidate for low powered IoT sensors.

In chapter 4, we considered a FS-SWIPT scheme combined with OFDM modulations for both energy harvesting and data transmission. We presented an analytical characterization of the transmitted signal and showed that FS-SWIPT OFDM signals are much more prone to nonlinear distortion than non-SWIPT schemes, especially when the EH term has much larger power than the data transmission term. However, we can overcome this degradation by employing receivers that estimate and remove the nonlinear distortion term in an iterative way, with small error propagation effects. Moreover, the performance of our iterative receiver is shown to be more robust to NLD in FS-SWIPT OFDM than in PS-SWIPT OFDM. We also studied the optimum performance of nonlinear FS-SWIPT OFDM schemes, and showed that it can be better than the optimum linear performance, with gains that can be particularly high in frequency-selective channels (due to an inherent diversity effect that is created in the transmitted signals by the nonlinear device). The gains are higher for more severe nonlinear characteristics, but decreases with the increase in the power of the EH term. In future work, we will consider imperfect channel estimation and explore novel methods to estimate the channel for the data subcarriers by using the limited number of known EH symbols.

In chapter 5, PS-SWIPT scheme is employed to harvest energy by using superimposed pilot and information signals. We present a systematic model to estimate CFO and channel condition by using the pilot signal, and improve the channel and information estimation accuracy with the help of IB-DFE. We find the optimum ratio of the power required for the pilot signal and information signal to achieve a desirable error rate performance in respect to varying SNR conditions. Also, an algorithm is implemented at the receiver by using the feedback of the channel and information estimation to improve the performance. The presented analytical results are in line with the numerical results. This system can be extended to a massive MIMO system model.

In chapter 6, we study two wiretap physical layer security models in two different scenarios and study threats from passive and active eavesdroppers, further we provide countermeasures against those eavesdroppers and improve the secrecy rate of the legitimate network. In both the models, energy harvesting signals are used as jamming signals against eavesdroppers. In the first system model, we implemented a SWIPT based self jamming physical layer security model which relies on channel precoding method to securely transmit information to the legitimate user. We considered different case studies by assuming that eavesdropper has high channel correlation with the legitimate user. We also consider the possibility of channel estimate error (channel link between jamming antennas to the legitimate user) that negatively affects the channel precoding. All the study cases are analysed with the theoretical expressions supported by the simulation results. Furthermore, BER performance of legitimate users and eavesdroppers are improved by using IB-DFE receiver and we conclude that IB-DFE can be used to improve the performance of legitimate networks and eventually improve secrecy rate of the network.

The second model presents a solution to overcome challenges posed by two active cooperative eavesdroppers, where one located near the transmitter and other located near the receiver of the legitimate network. Even though we present robust cooperative eavesdroppers, we could present solutions based on the analysis antenna diversity order and transmission power of jamming and information signals. We specifically consider that the eavesdropper has the CSI of the nearest node with negligible channel estimate error in order to study the optimum β (i.e., power ratio between the jamming signal and information signal). The simulated results of the expected jamming signal estimate error at the nearest eavesdropper (i.e., ξ_2) to the jammer shows that, by increasing the total of number of antennas at the jammer, the jammer can degrade the performance of ξ_2, even if ξ_2 has an equal number of receiving antennas. Therefore, jamming the signal SNR degradation at ξ_2 can degrade the performance of the MIMO IB-DFE receiver. The BER results of the information signal at the nearest eavesdropper (i.e., ξ_1) to the transmitter show that the BER of ξ_1 can be degraded by optimizing the β value at ξ_1 to 1. The optimization of β leads to energy efficient and secure communication, since $\beta = 1$ at ξ_1 is better for the legitimate network than for using a β greater than 1. Therefore, we conclude that, under a severely restricted environment, a legitimate network can improve the secrecy rate and can achieve better energy efficiency by increasing the number of antennas at a jammer and by optimizing β. In future, this work can be extended with multi-user scenerio under imperfect channel conditions as well as adopting this model with novel SWIPT techniques.

We summarise that in this thesis, we study SWIPT techniques for energy constrained networks and adopt SWIPT in signal processing applications. We introduce M-SWIPT technique, which is even compatible with the low powered sensors at low SNR region and thus improving network reachability. We also provide solutions for nonlinear distortion problems associated with the multi carrier signals and illustrate that the performance gain of the nonlinear signal can be even greater than the linear signal. We optimize energy requirements in a way to improve error and secrecy rate performance of the networks.

Bibliography

[1] J. Wu, S. Rangan, and H. Zhang. *Green communications: Theoretical fundamentals, algorithms, and applications*. CRC Press, 2016. ISBN: 9781138199804 (cit. on p. 1).

[2] D. N. K. Jayakody et al. *Wireless Information and Power Transfer: A New Paradigm for Green Communications*. New York: Springer, 2017 (cit. on pp. 1, 8, 28, 62, 77).

[3] R. Khan et al. "A Survey on Security and Privacy of 5G Technologies: Potential Solutions, Recent Advancements, and Future Directions". In: *IEEE Communications Surveys & Tutorials* 22.1 (2020), pp. 196–248. DOI: 10.1109/COMST.2019.2933899 (cit. on pp. 3, 25, 77, 89).

[4] T. D. Ponnimbaduge Perera et al. "Simultaneous Wireless Information and Power Transfer (SWIPT): Recent Advances and Future Challenges". In: *IEEE Communications Surveys & Tutorials* 20.1 (2018), pp. 264–302 (cit. on pp. 8, 12, 28, 77, 81).

[5] V. Liu et al. "Ambient backscatter: Wireless communication out of thin air". In: *ACM SIGCOMM computer communication review* 43.4 (2013), pp. 39–50 (cit. on p. 9).

[6] I. Flint et al. "Performance Analysis of Ambient RF Energy Harvesting with Repulsive Point Process Modeling". In: *IEEE Transactions on Wireless Communications* 14.10 (2015), pp. 5402–5416 (cit. on p. 9).

[7] A. Rajaram, D. N. K. Jayakody, and V. Skachek. "Store-then-cooperate: Energy harvesting scheme in cooperative relay networks". In: *2016 International Symposium on Wireless Communication Systems (ISWCS)*. 2016, pp. 445–450 (cit. on p. 9).

[8] A. Rajaram et al. "Opportunistic-Harvesting: RF Wireless Power Transfer Scheme for Multiple Access Relays System". In: *IEEE Access* 5 (2017), pp. 16084–16099 (cit. on p. 9).

[9] T. M. Cover and J. A. Thomas. "Information theory and statistics". In: *Elements of information theory* 1.1 (1991), pp. 279–335 (cit. on p. 10).

[10] C. E. Shannon and W. Weaver. "The mathematical theory of communication. University of Illinois". In: *Urbana* 117 (1949) (cit. on p. 10).

[11] M. K. Simon and M.-S. Alouini. *Digital communication over fading channels*. New York: Wiley, 2001 (cit. on p. 11).

[12] L. Szczecinski and A. Alvarado. *Bit-Interleaved Coded Modulation: Fundamentals, Analysis and Design*. IEEE Press. Wiley, 2014. ISBN: 9781118694022 (cit. on p. 11).

[13] T. Fehenberger et al. "On Probabilistic Shaping of Quadrature Amplitude Modulation for the Nonlinear Fiber Channel". In: *Journal of Lightwave Technology* 34.21 (2016), pp. 5063–5073 (cit. on pp. 11, 34, 35).

[14] D. M. Arnold et al. "Simulation-Based Computation of Information Rates for Channels With Memory". In: *IEEE Transactions on Information Theory* 52.8 (2006), pp. 3498–3508 (cit. on pp. 11, 34).

[15] R. Zhang and C. K. Ho. "MIMO Broadcasting for Simultaneous Wireless Information and Power Transfer". In: *IEEE Transactions on Wireless Communications* 12.5 (2013), pp. 1989–2001 (cit. on p. 12).

[16] K. Huang and E. Larsson. "Simultaneous Information and Power Transfer for Broadband Wireless Systems". In: *IEEE Transactions on Signal Processing* 61.23 (2013), pp. 5972–5986 (cit. on p. 12).

[17] X. Zhou, R. Zhang, and C. K. Ho. "Wireless Information and Power Transfer: Architecture Design and Rate-Energy Tradeoff". In: *IEEE Transactions on Communications* 61.11 (2013), pp. 4754–4767 (cit. on p. 15).

[18] A. Rajaram et al. "Modulation-Based Simultaneous Wireless Information and Power Transfer". In: *IEEE Communications Letters* 24.1 (2020), pp. 136–140 (cit. on p. 16).

[19] A. Rajaram et al. "Performance Evaluation of Nonlinear Effects in Frequency-Splitting SWIPT Signals". In: *2020 IEEE 91st Vehicular Technology Conference (VTC2020-Spring)*. 2020, pp. 1–5 (cit. on p. 16).

[20] Y. Lin, J. Shen, and Z. Zhao. "Chapter 5 - 5G flexible scheduling". In: *5G NR and Enhancements*. Ed. by J. Shen et al. Elsevier, 2022, pp. 167–281. ISBN: 978-0-323-91060-6. DOI: https://doi.org/10.1016/B978-0-323-91060-6.00005-2. URL: https://www.sciencedirect.com/science/article/pii/B9780323910606000052 (cit. on p. 16).

[21] A. Gusmao et al. "Comparison of two modulation choices for broadband wireless communications". In: *VTC2000-Spring. 2000 IEEE 51st Vehicular Technology Conference Proceedings (Cat. No.00CH37026)*. Vol. 2. 2000, 1300–1305 vol.2. DOI: 10.1109/VETECS.2000.851335 (cit. on pp. 16, 17).

[22] H. Sari, G. Karam, and I. Jeanclaude. "An analysis of orthogonal frequency-division multiplexing for mobile radio applications". In: *Proceedings of IEEE Vehicular Technology Conference (VTC)*. 1994, 1635–1639 vol.3. DOI: 10.1109/VETEC.1994.345373 (cit. on pp. 19, 20, 61).

[23] D. Falconer et al. "Frequency domain equalization for single-carrier broadband wireless systems". In: *IEEE Communications Magazine* 40.4 (2002), pp. 58–66. DOI: 10.1109/35.995852 (cit. on p. 19).

[24] M. Benvenuto and S. Tomasin. "Block iterative DFE for single carrier modulation". In: *Electronics Letters* 38 (19 2002), 1144–1145(1). URL: https://digital-library.theiet.org/content/journals/10.1049/el_20020767 (cit. on pp. 20, 60, 78, 84, 90).

[25] R. Dinis, A. Gusmao, and N. Esteves. "Iterative block-DFE techniques for single-carrier-based broadband communications with transmit/receive space diversity". In: *1st International Symposium on Wireless Communication Systems, 2004.* 2004, pp. 347–351. DOI: 10.1109/ISWCS.2004.1407267 (cit. on p. 20).

[26] R. Dinis et al. "Iterative layered space-time receivers for single-carrier transmission over severe time-dispersive channels". In: *IEEE Communications Letters* 8.9 (2004), pp. 579–581. DOI: 10.1109/LCOMM.2004.835339 (cit. on p. 20).

[27] R. Dinis et al. "Frequency-domain multipacket detection: a high throughput technique for SC-FDE systems". In: *IEEE Transactions on Wireless Communications* 8.7 (2009), pp. 3798–3807. DOI: 10.1109/TWC.2009.081275 (cit. on p. 20).

[28] G. Huang, A. Nix, and S. Armour. "Decision feedback equalization in SC-FDMA". In: *2008 IEEE 19th International Symposium on Personal, Indoor and Mobile Radio Communications*. 2008, pp. 1–5. DOI: 10.1109/PIMRC.2008.4699507 (cit. on p. 20).

[29] H. G. Myung, J. Lim, and D. J. Goodman. "Single carrier FDMA for uplink wireless transmission". In: vol. 1. 3. 2006, pp. 30–38. DOI: 10.1109/MVT.2006.307304 (cit. on p. 21).

[30] R. Dinis, D. Falconer, and B. Ng. "Iterative frequency-domain equalizers for adjacent channel interference suppression". In: *GLOBECOM '05. IEEE Global Telecommunications Conference, 2005.* Vol. 6. 2005, 5 pp.–3585. DOI: 10.1109/GLOCOM.2005.1578439 (cit. on p. 22).

[31] G. J. Foschini. "Layered space-time architecture for wireless communication in a fading environment when using multi-element antennas". In: *Bell labs technical journal* 1.2 (1996), pp. 41–59 (cit. on p. 23).

[32] G. J. Foschini and M. J. Gans. "On limits of wireless communications in a fading environment when using multiple antennas". In: *Wireless personal communications* 6.3 (1998), pp. 311–335 (cit. on p. 23).

[33] E. Telatar. "Capacity of multi-antenna Gaussian channels". In: *European transactions on telecommunications* 10.6 (1999), pp. 585–595 (cit. on p. 23).

[34] J. Kim and J. M. Cioffi. "Spatial multiuser access with antenna diversity using singular value decomposition". In: *2000 IEEE International Conference on Communications. ICC 2000. Global Convergence Through Communications. Conference Record*. Vol. 3. IEEE. 2000, pp. 1253–1257 (cit. on p. 23).

[35] J. Kim and J. Cioffi. "Transmission optimization with a space-time filter at low SNR wireless environment". In: *Seamless Interconnection for Universal Services. Global Telecommunications Conference. GLOBECOM'99.(Cat. No. 99CH37042)*. Vol. 1. IEEE. 1999, pp. 889–893 (cit. on p. 23).

[36] S. Stanczak, M. Wiczanowski, and H. Boche. *Fundamentals of resource allocation in wireless networks: theory and algorithms*. Vol. 3. Springer Science & Business Media, 2009 (cit. on p. 23).

[37] D. Borges et al. "Massive mimo techniques for 5g and beyond—opportunities and challenges". In: *Electronics* 10.14 (2021), p. 1667 (cit. on p. 23).

[38] T. L. Marzetta and B. M. Hochwald. "Capacity of a mobile multiple-antenna communication link in Rayleigh flat fading". In: *IEEE transactions on Information Theory* 45.1 (1999), pp. 139–157 (cit. on p. 24).

[39] P. Shaik et al. "On Impact of Imperfect CSI over SWIPT Device-to-Device (D2D) MIMO Relay Systems". In: *2020 International Conference on Signal Processing and Communications (SPCOM)*. 2020, pp. 1–5. DOI: 10.1109/SPCOM50965.2020.9179633 (cit. on p. 24).

[40] J. Kim, B. Clerckx, and P. D. Mitcheson. "Prototyping and experimentation of a closed-loop wireless power transmission with channel acquisition and waveform optimization". In: *2017 IEEE Wireless Power Transfer Conference (WPTC)*. 2017, pp. 1–4. DOI: 10.1109/WPT.2017.7953827 (cit. on p. 24).

[41] B. Clerckx et al. "Waveform optimization for Wireless Power Transfer with nonlinear energy harvester modeling". In: *2015 International Symposium on Wireless Communication Systems (ISWCS)*. 2015, pp. 276–280. DOI: 10.1109/ISWCS.2015.7454345 (cit. on p. 25).

[42] B. Clerckx and E. Bayguzina. "Waveform Design for Wireless Power Transfer". In: *IEEE Transactions on Signal Processing* 64.23 (2016), pp. 6313–6328. DOI: 10.1109/TSP.2016.2601284 (cit. on p. 25).

[43] J. Rodríguez-Fernández et al. "Frequency-Domain Compressive Channel Estimation for Frequency-Selective Hybrid Millimeter Wave MIMO Systems". In: *IEEE Transactions on Wireless Communications* 17.5 (2018), pp. 2946–2960. DOI: 10.1109/TWC.2018.2804943 (cit. on pp. 25, 61).

[44] P. Moose. "A technique for orthogonal frequency division multiplexing frequency offset correction". In: *IEEE Transactions on Communications* 42.10 (1994), pp. 2908–2914. DOI: 10.1109/26.328961 (cit. on pp. 25, 60, 61, 65).

[45] A. Rajaram et al. "Receiver Design to Employ Simultaneous Wireless Information and Power Transmission with Joint CFO and Channel Estimation". In: *IEEE Access* 7 (2019), pp. 9678–9687 (cit. on pp. 77, 78, 81, 96).

[46] X. Tang et al. "Secure Transmission of Cooperative Zero-Forcing Jamming for Two-User SWIPT Sensor Networks". In: *Sensors* 18.2 (2018), p. 331. ISSN: 1424-8220. DOI: 10.3390/s18020331. URL: http://dx.doi.org/10.3390/s18020331 (cit. on pp. 25, 77).

[47] D. W. K. Ng, L. Xiang, and R. Schober. "Multi-objective beamforming for secure communication in systems with wireless information and power transfer". In: *2013 IEEE 24th Annual International Symposium on Personal, Indoor, and Mobile Radio Communications (PIMRC)*. 2013, pp. 7–12. DOI: 10.1109/PIMRC.2013.6666095 (cit. on p. 25).

[48] A. D. Wyner. "The Wire-Tap Channel". In: *Bell System Technical Journal* 54.8 (), pp. 1355–1387 (cit. on pp. 25, 77, 84).

[49] S. Leung-Yan-Cheong and M. Hellman. "The Gaussian wire-tap channel". In: *IEEE Transactions on Information Theory* 24.4 (1978), pp. 451–456. DOI: 10.1109/TIT.1978.1055917 (cit. on pp. 25, 77, 84).

[50] F. Oggier and B. Hassibi. "The Secrecy Capacity of the MIMO Wiretap Channel". In: *IEEE Transactions on Information Theory* 57.8 (2011), pp. 4961–4972. DOI: 10.1109/TIT.2011.2158487 (cit. on pp. 25, 77).

[51] S. Goel and R. Negi. "Guaranteeing Secrecy using Artificial Noise". In: *IEEE Transactions on Wireless Communications* 7.6 (2008), pp. 2180–2189. DOI: 10.1109/TWC.2008.060848 (cit. on pp. 26, 77).

[52] G. Anjos et al. "Exploiting the Reciprocal Channel for Discrete Jamming to Secure Wireless Communications Against Multiple-Antenna Eavesdropper". In: *IEEE Access* 6 (2018), pp. 33410–33420. DOI: 10.1109/ACCESS.2018.2845839 (cit. on pp. 26, 77).

[53] K. Cumanan et al. "Physical Layer Security Jamming: Theoretical Limits and Practical Designs in Wireless Networks". In: *IEEE Access* 5 (2017), pp. 3603–3611. DOI: 10.1109/ACCESS.2016.2636239 (cit. on pp. 26, 77).

[54] B. He, X. Zhou, and T. D. Abhayapala. "Wireless Physical Layer Security with Imperfect Channel State Information: A Survey". In: *CoRR* abs/1307.4146 (2013). arXiv: 1307.4146. URL: http://arxiv.org/abs/1307.4146 (cit. on p. 26).

[55] T.-H. Chou, S. C. Draper, and A. M. Sayeed. "Impact of channel sparsity and correlated eavesdropping on secret key generation from multipath channel randomness". In: *2010 IEEE International Symposium on Information Theory*. 2010, pp. 2518–2522. DOI: 10.1109/ISIT.2010.5513556 (cit. on pp. 27, 79).

[56] J. Zhang et al. "On the Key Generation From Correlated Wireless Channels". In: *IEEE Communications Letters* 21.4 (2017), pp. 961–964. DOI: 10.1109/LCOMM.2017.2649496 (cit. on p. 27).

[57] A. Rajaram et al. "Secure Information Transmission with Self Jamming SWIPT". In: *Electronics* 9.4 (2020), p. 587. ISSN: 2079-9292. DOI: 10.3390/electronics9040587. URL: http://dx.doi.org/10.3390/electronics9040587 (cit. on pp. 27, 77, 89, 99).

[58] W. Liu et al. "SWIPT with practical modulation and RF energy harvesting sensitivity". In: *2016 IEEE International Conference on Communications (ICC)*. 2016, pp. 1–7. DOI: 10.1109/ICC.2016.7511404 (cit. on p. 28).

[59] G. Forney et al. "Efficient Modulation for Band-Limited Channels". In: *IEEE Journal on Selected Areas in Communications* 2.5 (1984), pp. 632–647 (cit. on p. 28).

[60] F. R. Kschischang and S. Pasupathy. "Optimal nonuniform signaling for Gaussian channels". In: *IEEE Transactions on Information Theory* 39.3 (1993), pp. 913–929 (cit. on p. 28).

[61] W. Betts, A. R. Calderbank, and R. Laroia. "Performance of nonuniform constellations on the Gaussian channel". In: *IEEE Transactions on Information Theory* 40.5 (1994), pp. 1633–1638 (cit. on p. 28).

[62] J.-X. Cai et al. "70.4 Tb/s Capacity over 7,600 km in C+L Band Using Coded Modulation with Hybrid Constellation Shaping and Nonlinearity Compensation". In: *Optical Fiber Communication Conference Postdeadline Papers*. Optical Society of America, 2017, Th5B.2 (cit. on p. 28).

[63] J. R. Barry, E. A. Lee, and D. G. Messerschmitt. *Digital communication*. Springer Science & Business Media, 2004 (cit. on pp. 34, 49).

[64] D. Altinel and G. K. Kurt. "Frequency Switching for Simultaneous Wireless Information and Power Transfer". In: *2016 IEEE 84th Vehicular Technology Conference (VTC-Fall)*. 2016, pp. 1–5. DOI: 10.1109/VTCFall.2016.7881020 (cit. on p. 38).

[65] P. A. Hoeher. "FSK-Based Simultaneous Wireless Information and Power Transfer in Inductively Coupled Resonant Circuits Exploiting Frequency Splitting". In: *IEEE Access* 7 (2019), pp. 40183–40194 (cit. on p. 38).

[66] A. Kurs et al. "Wireless Power Transfer via Strongly Coupled Magnetic Resonances". In: *Science* 317.5834 (2007), pp. 83–86. DOI: 10.1126/science.1143254. eprint: https://science.sciencemag.org/content/317/5834/83.full.pdf. URL: https://science.sciencemag.org/content/317/5834/83 (cit. on p. 38).

[67] Y. Kim and H. Ling. “Investigation of coupled mode behaviour of electrically small meander antennas”. In: *Electronics letters* 43.23 (2007), pp. 1250–1252 (cit. on p. 38).

[68] A. Karalis, J. D. Joannopoulos, and M. Soljačić. “Efficient wireless non-radiative mid-range energy transfer”. In: *Annals of physics* 323.1 (2008), pp. 34–48 (cit. on p. 38).

[69] J.-G. Kim et al. “A Splitting Frequencies-Based Wireless Power and Information Simultaneous Transfer Method”. In: *IEEE Transactions on Circuits and Systems I: Regular Papers* 65.12 (2018), pp. 4434–4445. DOI: 10.1109/TCSI.2018.2847339 (cit. on p. 38).

[70] Y. Park et al. “33.7 A Frequency-Splitting-Based Wireless Power and Data Transfer IC for Neural Prostheses with Simultaneous 115mW Power and 2.5Mb/s Forward Data Delivery”. In: *2021 IEEE International Solid- State Circuits Conference (ISSCC)*. Vol. 64. 2021, pp. 472–474. DOI: 10.1109/ISSCC42613.2021.9365781 (cit. on p. 38).

[71] S. Merchan, A. Armada, and J. Garcia. “OFDM performance in amplifier nonlinearity”. In: *IEEE Transactions on Broadcasting* 44.1 (1998), pp. 106–114. DOI: 10.1109/11.713060 (cit. on p. 38).

[72] H. Ochiai and H. Imai. “Performance analysis of deliberately clipped OFDM signals”. In: *IEEE Transactions on Communications* 50.1 (2002), pp. 89–101. DOI: 10.1109/26.975762 (cit. on p. 38).

[73] J. Joung, C. K. Ho, and S. Sun. “Tradeoff of spectral and energy efficiencies: Impact of power amplifier on OFDM systems”. In: *2012 IEEE Global Communications Conference (GLOBECOM)*. 2012, pp. 3274–3279. DOI: 10.1109/GLOCOM.2012.6503619 (cit. on p. 38).

[74] M.-C. Kim, Y. Shin, and S. Im. “Compensation of nonlinear distortion using a predistorter based on the fixed point approach in OFDM systems”. In: *VTC ’98. 48th IEEE Vehicular Technology Conference. Pathway to Global Wireless Revolution (Cat. No.98CH36151)*. Vol. 3. 1998, 2145–2149 vol.3. DOI: 10.1109/VETEC.1998.686137 (cit. on p. 38).

[75] H. W. Kang, Y. S. Cho, and D. H. Youn. “On compensating nonlinear distortions of an OFDM system using an efficient adaptive predistorter”. In: *IEEE Transactions on Communications* 47.4 (1999), pp. 522–526. DOI: 10.1109/26.764925 (cit. on p. 38).

[76] A. Gusmao, R. Dinis, and P. Torres. “Low-PMEPR OFDM transmission with an iterative receiver technique for cancellation of nonlinear distortion”. In: *IEEE VEHICULAR TECHNOLOGY CONFERENCE*. Vol. 62. 4. IEEE; 1999. 2005, p. 2367 (cit. on p. 39).

[77] J. Guerreiro, R. Dinis, and P. Montezuma. "Optimum and Sub-Optimum Receivers for OFDM Signals with Strong Nonlinear Distortion Effects". In: *IEEE Transactions on Communications* 61.9 (2013), pp. 3830–3840 (cit. on p. 39).

[78] H. H. Jang, K. W. Choi, and D. I. Kim. "Novel Frequency-Splitting SWIPT for Overcoming Amplifier Nonlinearity". In: *IEEE Wireless Communications Letters* 9.6 (2020), pp. 826–829. DOI: 10.1109/LWC.2020.2971983 (cit. on p. 39).

[79] T. Araújo and R. Dinis. *Analytical Evaluation of Nonlinear Distortion Effects on Multicarrier Signals*. USA: CRC Press, Inc., 2015. ISBN: 1482215942 (cit. on pp. 43, 48).

[80] M. Abramowitz and I. A. Stegun. "Handbook of mathematical functions with formulas, graphs, and mathematical tables". In: *Appl.* 1972 (cit. on p. 43).

[81] A. Kaye, D. George, and M. Eric. "Analysis and Compensation of Bandpass Nonlinearities for Communications". In: *IEEE Transactions on Communications* 20.5 (1972), pp. 965–972. DOI: 10.1109/TCOM.1972.1091254 (cit. on p. 44).

[82] C. Rapp. "Effects of HPA-nonlinearity on a 4-DPSK/OFDM-signal for a digital sound broadcasting signal". In: *ESA Special Publication* 332 (1991), pp. 179–184 (cit. on p. 44).

[83] A. Saleh. "Frequency-Independent and Frequency-Dependent Nonlinear Models of TWT Amplifiers". In: *IEEE Transactions on Communications* 29.11 (1981), pp. 1715–1720. DOI: 10.1109/TCOM.1981.1094911 (cit. on p. 44).

[84] W. G. Jeon, K. H. Chang, and Y. S. Cho. "An adaptive data predistorter for compensation of nonlinear distortion in OFDM systems". In: *IEEE Transactions on Communications* 45.10 (1997), pp. 1167–1171. DOI: 10.1109/26.634677 (cit. on p. 44).

[85] J. J. Bussgang. "Crosscorrelation functions of amplitude-distorted Gaussian signals". In: (1952) (cit. on p. 44).

[86] R. Dinis and A. Gusmao. "A class of nonlinear signal-processing schemes for bandwidth-efficient OFDM transmission with low envelope fluctuation". In: *IEEE Transactions on Communications* 52.11 (2004), pp. 2009–2018. DOI: 10.1109/TCOMM.2004.836567 (cit. on p. 45).

[87] T. Araújo and R. Dinis. "Analytical Evaluation of Nonlinear Effects on OFDMA Signals". In: *IEEE Transactions on Wireless Communications* 9.11 (2010), pp. 3472–3479. DOI: 10.1109/TWC.2010.081810.091662 (cit. on p. 45).

[88] G. Stette. "Calculation of Intermodulation from a Single Carrier Amplitude Characteristic". In: *IEEE Transactions on Communications* 22.3 (1974), pp. 319–323. DOI: 10.1109/TCOM.1974.1092195 (cit. on p. 45).

[89] F. Peng and W. E. Ryan. "MLSD Bounds and Receiver Designs for Clipped OFDM Channels". In: *IEEE Transactions on Wireless Communications* 7.9 (2008), pp. 3568–3578. DOI: 10.1109/TWC.2008.070368 (cit. on p. 51).

[90] J. Guerreiro et al. "On the Achievable Performance of Nonlinear MIMO Systems". In: *IEEE Communications Letters* 23.10 (2019), pp. 1725–1729. DOI: 10.1109/LCOMM.2019.2929040 (cit. on p. 51).

[91] S. Verdu. "Maximum likelihood sequence detection for intersymbol interference channels: A new upper bound on error probability". In: *IEEE Transactions on Information Theory* 33.1 (1987), pp. 62–68. DOI: 10.1109/TIT.1987.1057271 (cit. on p. 51).

[92] S. V. Zhidkov. "Orthogonal transform multiplexing with memoryless nonlinearity: A possible alternative to traditional coded-modulation schemes". In: *2017 9th International Congress on Ultra Modern Telecommunications and Control Systems and Workshops (ICUMT)*. 2017, pp. 209–214. DOI: 10.1109/ICUMT.2017.8255159 (cit. on p. 51).

[93] C. Yang et al. "Fast GAMP Algorithm for Nonlinearly Distorted OFDM Signals". In: *IEEE Communications Letters* 25.5 (2021), pp. 1682–1686. DOI: 10.1109/LCOMM.2021.3056657 (cit. on p. 51).

[94] J. Guerreiro, R. Dinis, and P. Montezuma. "On the Optimum Multicarrier Performance With Memoryless Nonlinearities". In: *IEEE Transactions on Communications* 63.2 (2015), pp. 498–509. DOI: 10.1109/TCOMM.2015.2388484 (cit. on pp. 51–53).

[95] K. Raghunath and A. Chockalingam. "SC-FDMA Versus OFDMA: Sensitivity to Large Carrier Frequency and Timing Offsets on the Uplink". In: *GLOBECOM 2009 - 2009 IEEE Global Telecommunications Conference*. 2009, pp. 1–6. DOI: 10.1109/GLOCOM.2009.5425747 (cit. on p. 60).

[96] M. Sabbaghian and D. Falconer. "Joint Turbo Frequency Domain Equalization and Carrier Synchronization". In: vol. 7. 1. 2008, pp. 204–212. DOI: 10.1109/TWC.2008.060451 (cit. on p. 60).

[97] R. Dinis et al. "Joint turbo equalisation and carrier synchronisation for SC-FDE schemes". In: *European Transactions on Telecommunications* 21.2 (2010), pp. 131–141 (cit. on p. 60).

[98] F. Silva et al. "Frequency-domain receiver design for transmission through multipath channels with strong doppler effects". In: *Wireless Personal Communications* 83.2 (2015), pp. 1213–28 (cit. on p. 60).

[99] H. Doğan, N. Odabaşıoğlu, and B. Karakaya. "Time and Frequency Synchronization with Channel Estimation for SC-FDMA Systems Over Time-Varying Channels". In: *Wireless Personal Communications* 96.1 (2017), 163–181 (cit. on p. 60).

[100] F. Silva, R. Dinis, and P. Montezuma. “Channel Estimation and Equalization for Asynchronous Single Frequency Networks”. In: *IEEE Transactions on Broadcasting* 60.1 (2014), pp. 110–119. DOI: 10.1109/TBC.2014.2301900 (cit. on p. 60).

[101] M. Morelli and U. Mengali. “An improved frequency offset estimator for OFDM applications”. In: *IEEE Communications Letters* 3.3 (1999), pp. 75–77. DOI: 10.1109/4234.752907 (cit. on p. 60).

[102] T. Schmidl and D. Cox. “Robust frequency and timing synchronization for OFDM”. In: *IEEE Transactions on Communications* 45.12 (1997), pp. 1613–1621. DOI: 10.1109/26.650240 (cit. on p. 60).

[103] J. Ma et al. “Iterative LMMSE Individual Channel Estimation Over Relay Networks With Multiple Antennas”. In: *IEEE Transactions on Vehicular Technology* 67.1 (2018), pp. 423–435. DOI: 10.1109/TVT.2017.2746562 (cit. on p. 60).

[104] R. Dinis, C.-T. Lam, and D. Falconer. “Joint Frequency-Domain Equalization and Channel Estimation Using Superimposed Pilots”. In: *2008 IEEE Wireless Communications and Networking Conference*. 2008, pp. 447–452. DOI: 10.1109/WCNC.2008.84 (cit. on pp. 60, 66, 78).

[105] J. Guerreiro, R. Dinis, and P. Montezuma. “Analytical Performance Evaluation of Precoding Techniques for Nonlinear Massive MIMO Systems With Channel Estimation Errors”. In: *IEEE Transactions on Communications* 66.4 (2018), pp. 1440–1451. DOI: 10.1109/TCOMM.2017.2782321 (cit. on p. 61).

[106] E. Dahlmaa et al. “A framework for future radio access”. In: *2005 IEEE 61st Vehicular Technology Conference*. Vol. 5. 2005, 2944–2948 Vol. 5. DOI: 10.1109/VETECS.2005.1543886 (cit. on pp. 62, 66).

[107] A. Rajaram et al. “Novel SWIPT Schemes for 5G Wireless Networks”. In: *Sensors* 19.5 (2019), p. 1169. ISSN: 1424-8220. DOI: 10.3390/s19051169. URL: http://dx.doi.org/10.3390/s19051169 (cit. on p. 77).

[108] G. Anjos et al. “Exploiting Reciprocal Channel Estimations for Jamming to Secure Wireless Communications”. In: *in proc. International Wireless Days Conference* (2017) (cit. on p. 77).

[109] A Silva et al. “Performance Evaluation of IB-DFE based Strategies for SC-FDMA Systems”. In: *EURASIP Journal on Wireless Communications and Networking* (2013). DOI: 10.1186/1687-1499-2013-292 (cit. on pp. 78, 90).

[110] D. Castanheira et al. “Efficient Transmitter and Receiver Designs for SC-FDMA Based Heterogeneous Networks”. In: *IEEE Transactions on Communications* 63.7 (2015), pp. 2500–2510. DOI: 10.1109/TCOMM.2015.2434383 (cit. on pp. 78, 90).

[111] W.-C. Liao et al. "QoS-Based Transmit Beamforming in the Presence of Eavesdroppers: An Optimized Artificial-Noise-Aided Approach". In: *IEEE Transactions on Signal Processing* 59.3 (2011), pp. 1202–1216. DOI: 10.1109/TSP.2010.2094610 (cit. on p. 89).

[112] B. Ji et al. "Research on Secure Transmission Performance of Electric Vehicles Under Nakagami-m Channel". In: *IEEE Transactions on Intelligent Transportation Systems* 22.3 (2021), pp. 1881–1891. DOI: 10.1109/TITS.2020.3030540 (cit. on p. 89).

[113] P. L. Yeoh, N. Yang, and K. J. Kim. "Secrecy Outage Probability of Selective Relaying Wiretap Channels with Collaborative Eavesdropping". In: *2015 IEEE Global Communications Conference (GLOBECOM)*. 2015, pp. 1–6. DOI: 10.1109/GLOCOM.2015.7417082 (cit. on p. 89).

[114] J. Yang, I. Kim, and D. I. Kim. "Optimal Cooperative Jamming for Multiuser Broadcast Channel with Multiple Eavesdroppers". In: *IEEE Transactions on Wireless Communications* 12.6 (2013), pp. 2840–2852. DOI: 10.1109/TWC.2013.040413.120972 (cit. on p. 89).

[115] A. Silva et al. "Iterative Frequency-Domain Detection for IA-Precoded MC-CDMA Systems". In: *IEEE Transactions on Communications* 62.4 (2014), pp. 1240–1248. DOI: 10.1109/TCOMM.2014.022514.130681 (cit. on p. 90).

[116] D Borges et al. "Two Low Complexity MRC and EGC Based Receivers for SC-FDE Modulations with Massive MIMO Schemes". In: *J. Signal Process. System* 90 (2018), p. 331. DOI: 10.1007/s11265-018-1335-1 (cit. on p. 93).